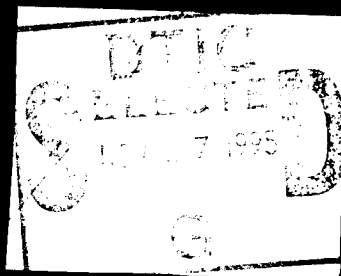


COMPRESSIVE STRENGTH OF
LAMINA REINFORCED

J. G. Davis, 1973

Published on demand by
UNIVERSITY MICROFILMS
University Microfilms Limited, High Wycomb, England
A Xerox Company, Ann Arbor, Michigan, U.S.A.



19951121 013

DISTRIBUTION STATEMENT A

Approved for public release;
Distribution Unlimited

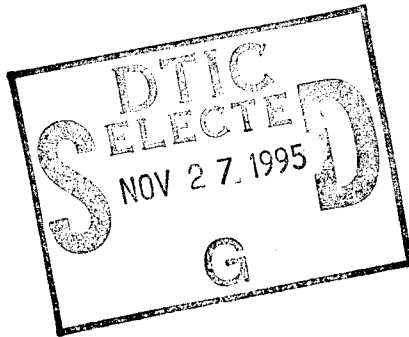
PLASTEC

--- 1 - AD NUMBER: D423225
--- 5 - CORPORATE AUTHOR: VIRGINIA POLYTECHNIC INST AND STATE UNIV
--- BLACKSBURG DEPT OF ENGINEERING SCIENCE AND MECHANICS
--- 6 - UNCLASSIFIED TITLE: COMPRESSIVE STRENGTH OF LAMINA REINFORCED
--- AND FIBER REINFORCED COMPOSITE MATERIALS,
---10 - PERSONAL AUTHORS: DAVIS, J. G. , JR. ;
---11 - REPORT DATE: , 1973
---12 - PAGINATION: 239P
---20 - REPORT CLASSIFICATION: UNCLASSIFIED
---21 - SUPPLEMENTARY NOTE: DISSERTATION.
---22 - LIMITATIONS (ALPHA): APPROVED FOR PUBLIC RELEASE; DISTRIBUTION
--- UNLIMITED. AVAILABILITY: UNIVERSITY MICROFILMS, 300 N. ZEEB RD.,
--- ANN ARBOR, MI. 48106.
---33 - LIMITATION CODES: 1 24

--- END Y FOR NEXT ACCESSION END

--- END OF DISPLAY LIST

--- <<ENTER NEXT COMMAND>>



This is an authorized facsimile and was produced by microfilm-xerography in 1974 by Xerox University Microfilms, Ann Arbor, Michigan, U.S.A.

Accession For	
NTIS CRA&I	<input checked="" type="checkbox"/>
DTIC TAB	<input type="checkbox"/>
Unannounced	<input type="checkbox"/>
Justification	
By	
Dist. istribution /	
Availability Codes	
Dist	Avail and/or Special
A-1	

73-26,264

DAVIS, Jr., John Grady, 1938-
COMPRESSIVE STRENGTH OF LAMINA REINFORCED
AND FIBER REINFORCED COMPOSITE MATERIALS.

Virginia Polytechnic Institute and State
University, Ph.D., 1973
Engineering Mechanics

University Microfilms, A XEROX Company, Ann Arbor, Michigan

COMPRESSIVE STRENGTH OF LAMINA REINFORCED
AND FIBER REINFORCED COMPOSITE MATERIALS

by

John C. Davis, Jr.

Thesis submitted to the Graduate Faculty of the
Virginia Polytechnic Institute and
State University

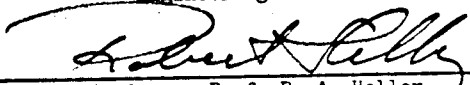
in candidacy for the degree of

DOCTOR OF PHILOSOPHY

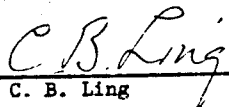
in

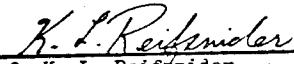
Engineering Mechanics


APPROVED:


Chairman, Prof. R. A. Heller


Prof. G. W. Swift


Prof. C. B. Ling


Prof. K. L. Reifsnider


Prof. R. M. Barker

May 1973

Blacksburg, Virginia

ACKNOWLEDGEMENT

The author is grateful to the National Aeronautics and Space Administration for the opportunity to write this thesis as part of his research assignment at the Langley Research Center and to Professors R. A. Heller and G. W. Swift of the Engineering Science and Mechanics Department, Virginia Polytechnic Institute and State University for their encouragement and helpful guidance. The author is deeply indebted to Mr. R. A. Pride, who deferred or switched work assignments so that the author could complete this thesis in a reasonable time period. Acknowledgement is also noted for the assistance Mr. D. J. Baker provided in debugging computer programs and the assistance that Mrs. S. K. Seward provided in making a thorough search of the literature. The work of Mr. J. K. Kiss, who provided laboratory assistance, and Mrs. S. D. Humble, who typed the manuscript is appreciated and acknowledged. Special thanks and appreciation are due my wife and children, who not only persevered through a drawn-out education period, but encouraged me on to completion.

TABLE OF CONTENTS

	Page
TITLE	1
ACKNOWLEDGEMENT	ii
LIST OF SYMBOLS	v
LIST OF FIGURES AND TABLES	xiii
I. INTRODUCTION	1
II. REVIEW OF LITERATURE	3
A. Chronological Review	3
B. Summary	30
III. ANALYTICAL MODEL	32
IV. INTERLAMINAR SHEAR	34
A. Displacements, Strains, and Stresses	34
B. Bending Moments, Normal and Shear Forces	37
C. Equilibrium Equations	39
D. Shear Stresses	46
E. Solution of Governing Equations	48
F. Initial and Boundary Conditions	55
V. SHEAR INSTABILITY OF MULTILAYERED MEDIA	58
VI. EXPERIMENTAL INVESTIGATION	63
A. Lamina Reinforced Composites	63
1. Laminate Fabrication	63
2. Matrix Specimens	65
3. Matrix-Reinforcement Bond Strength Specimens	65
4. Compression Test of Laminate Specimens	66
5. Compression Test of Matrix Specimens	67
6. Torsion Test of Matrix Specimens	68
7. Bond Strength Test	68
B. Fiber Reinforced Composites	68
1. Fabrication of Tube Specimens	68
2. Compression Test	71
3. Torsion Test	72
4. Combined Compression and Torsion Test	72
VII. RESULTS AND DISCUSSION	74

	Page
A. Theory	74
1. Reinforcement/Matrix Stiffness Ratio	74
2. Shear Stress Distribution	76
3. Nonlinear Matrix Behavior	77
4. Load Increment Size	79
5. Boundary Conditions	80
B. Experiment	81
1. Matrix Compression Test	81
2. Matrix Shear Test	82
3. Matrix-Reinforcement Bond Strength Test	82
4. Compression Test of Laminate Specimens	82
5. Compression Test of Fiber Reinforced Composites	86
6. Torsion Test of Fiber Reinforced Composites	88
7. Combined Compression and Torsion Test of Fiber Reinforced Composites	88
C. Comparison of Experiment and Theory	90
1. Laminate Specimens	90
2. Fiber Reinforced Composite Test Results	91
VIII. CONCLUDING REMARKS	94
IX. REFERENCES	95
APPENDICES	101
A. INTERLAMINAR SHEAR STRESS COMPUTER PROGRAM	101
B. CLASSICAL BEAM THEORY DEFLECTION FOR CASE A AND CASE B BOUNDARY CONDITIONS	104
C. FIBER CURVATURE INVESTIGATION	108
VITA	227

LIST OF SYMBOLS

A	constant of integration, see equation (B-6)
A_f, A_m	cross sectional area of fiber, matrix or m^{th} layer, respectively
a_0	amplitude of initial displacement, see equation (4.63)
a_1, a_2	empirical curve-fit parameters, see equation (2.17)
a_3	constant in equation (2.19)
a_f, a_v	parameters associated fibers and voids, respectively, see equation (2.13)
B	constant of integration, see equation (B-6)
b	width of beam
C	constant of integration, see equation (B-6)
c	one half the matrix thickness, see figure (B-2)
C.B.T.	classical beam theory
D	constant of integration, see equation (B-6)
d_f, d_v	diameter of fiber and void, respectively
E_f, E_m	Young's modulus of fiber, matrix or m^{th} layer, respectively
E_{mt}	tangent modulus of matrix
E_L, E_T	Young's modulus of the composite measured parallel and transverse to the fibers, respectively
E	Young's modulus of an isotropic material
F_f, F_m	compressive strength of fiber and matrix, respectively, see equation (2.13)
F_B	interface bond strength, see equation (2.13)

F_R	residual compressive strength, see equation (2.13)
F_{Lc}, F_{Tt}	"true" ultimate compressive strength in the fiber direction and ultimate composite strength in the transverse direction, respectively, (refer to equation (2.23) and reference 48)
F_i	first moment of area of the i^{th} layer about the midplane, see equation (4.10)
F_x, F_z	forces in the x and z direction, respectively
F	constant of integration, see equation (B-6)
G_f, G_m	shear modulus of fiber, matrix or m^{th} layer, respectively
G_{mt}	tangent shear modulus of matrix
G_z	interlaminar shear modulus defined in reference 41
G_{LT}	shear modulus of a unidirectionally fiber reinforced composite measured parallel and perpendicular to the fibers
G	shear modulus of an isotropic material
G^*	apparent shear modulus, see equation (7.1)
H_i	matrices in the recurrence formulas, see equation (4.60)
h_i	distance from the midplane of the laminate to the outer surface of the $(i-1)^{\text{th}}$ layer
h	thickness of the reinforcement layer, see figure (B-2)
I_m	moment of inertia of the m^{th} layer about the midplane
I	moment of inertia of a laminated beam about the midplane
IPK	counter used in the interlaminar shear stress computer program

J	number of finite intervals into which the beam is subdivided
k	constant, equation (2.1)
k	ratio of a uniformly applied transverse tensile stress to the maximum transverse tensile stress in the resin, see equation (2.23)
k_c	parameter defined by equation (B-7)
k_l	parameter defined by equation (B-14)
k'	shear correction term
L	length of laminate, see figure 4.4
M_{tm}	bending moment in the m^{th} layer (+ above, - below midplane)
M	total moment of forces about the midplane of a laminate or beam
N_{tm}	normal forces due to bending in the m^{th} layer (+ above, - below midplane)
n_f, n_v	number of fibers and voids, respectively
n	shear modulus ratio, see equation (2.7)
n	total number of layers above the midplane
P_{cr}	applied compressive load at which instability occurs
P_m	applied compressive load on the m^{th} layer
P_x	external shear load
P_z	external transverse load
P	applied compressive load on a beam
$P_i(p)$	components of the transverse load vector at the p^{th} node point
$\frac{P}{p}$	load vector at the p^{th} node

P_1	value of the applied compressive load for layer number one
P_{LO}	value of applied compressive load on layer number one that initiates nonlinear shear stress-strain behavior
Q_{zm}	transverse shear force in the m^{th} layer (+ above, - below midplane)
Q_i	vector in the recurrence formulas, see equation (4.61)
R_{ij}	coefficients of a submatrix that forms part of the finite difference equations, see equations (4.53)
\underline{R}_p	a submatrix that forms part of the finite difference equations, see equation (4.52)
r_f	radius of gyration of the fiber
S_{ij}	coefficients of a submatrix that forms part of the finite difference equations, see equations (4.54)
\underline{S}_p	a submatrix that forms part of the finite difference equations, see equation (4.52)
s	$n + 1$
T_{ij}	coefficients of a submatrix that forms part of the finite difference equations, see equations (4.55)
\underline{T}_p	a submatrix that forms part of the finite difference equations, see equation (4.52)
U	the change in strain energy in going from the initial position to the buckled position
u_{zm}	displacement in the length direction of the m^{th} layer (+ above, - below midplane)

V_f, V_m, V_v	volume fraction of fiber, matrix, and void, respectively
V_i	volume fraction of the i^{th} layer
\bar{V}_f, \bar{V}_m	quantities defined by equations (2.16) and (2.15), respectively
$v_{\pm m}$	displacement in the width direction of the multilayered beam
W	work done by the applied load in going from the initial position to the buckled position
w_0	initial transverse displacement
w_1	transverse displacement due to bending and shear loads
w	total transverse displacement
x	coordinate measured along the length direction of the beam
\underline{Y}_p	solution vector for the p^{th} node point along the beam
y	coordinate measured in the width direction of the beam
z	coordinate measured in the depth direction of the beam
β_{fc}, β_{mc}	theory-experiment correlation factor for matrix and fiber, respectively, used in equation (2.14)
β	ratio of maximum shear stress to average shear stress in a buckled column, see equation (2.18)
β	ratio of maximum transverse tensile stress in the resin to the applied axial stress
$\gamma_{xy\pm m}, \gamma_{xz\pm m}$	shear strain in the $\pm m^{\text{th}}$ layer measured in the x-y and x-z planes, respectively
γ_i	shear strain in the i^{th} layer of a multilayered media, see figure (5.1)

x

γ limiting shear deformation on a plane oriented at 45° to the direction of the filaments, refer to equation (2.12)

δ moment arm for the applied axial force, see figure (4.4)

δ displacement of the applied axial force in going from the initial position to the buckled position, see figure (5.1)

$\epsilon_{x1m}, \epsilon_{y1m}, \epsilon_{z1m}$ strain in the 1^{th} layer parallel to the x, y, and z axes, respectively

ϵ_p limiting strain, refer to equation (2.13) and reference 27

θ_1 the angle between the z axis and the initial position of the cross section of the 1^{th} layer

λ Lagrange undetermined multiplier

μ_{LT}, μ_{TL} Poisson's ratio associated with stresses applied parallel and perpendicular to the fibers, respectively, in a composite material

μ Poisson's ratio for an isotropic material

ξ stiffness parameter, refer to equation (2.21) and reference 40

σ_f, σ_m axial compressive stress in the fiber and matrix, respectively

σ_L axial compressive stress in the a composite material at failure, see equation (2.23)

σ_{mc} matrix compressive strength, see equation (2.14)

σ_{my} matrix yield strength

σ_y matrix "characteristic stress", refer to equation (2.11) and reference 16

σ	compressive strength of a composite material
σ_f^*, σ_m^*	compressive stress in the fiber and matrix, respectively, corresponding to shear instability
σ_{im}	axial stress in the i^{th} layer due to bending and shearing loads
$\sigma_{m,m}$	normal stress acting on the upper surface of the m^{th} layer
$\sigma_{xim}, \sigma_{yim}, \sigma_{zim}$	normal stresses in the i^{th} layer measured parallel to the x, y, and z axes, respectively
τ_i	value of shear stress corresponding to the first break in the five segment stress-strain curves for the i^{th} layer
τ_{im}	shear stress in the m^{th} layer measured in the x-z plane
τ_{ave}	average shear stress across the m^{th} layer
τ_{12}	interlaminar shear strength, see equation (2.17)
τ_{LT}	interlaminar shear strength, see equation (2.24)
$\tau_{m,m}$	interlaminar shear stress above the m^{th} layer and acting on the m^{th} layer
τ_{xz}	shear stress measured in the x-z plane
$\tau_{xyim}, \tau_{xzim}, \tau_{yzim}$	shear stresses in the m^{th} layer and measured in the x-y, x-z, and y-z planes, respectively
τ	shear stress acting along the upper and lower surfaces of a multilayered beam, see figure B.2
τ_{BAR}_i	average shear stress across the i^{th} layer at the beam quarter point
ϕ_i	rotation defined by equation (4.49)

ϕ_c

angle of misalignment between the reinforcement and the
load axis

ψ_i

angle between the z axis and the final position of the
deformed cross section of the i^{th} layer

LIST OF FIGURES AND TABLES

FIGURE	PAGE
1.1 Photomicrographs of composite materials	122
3.1 Analytical models of composite material	123
4.1 Laminated beam model of composite material	124
4.2 Notation for multilayered beam	126
4.3 Equilibrium of beam element	127
4.4 Moment arm (δ) for axial force	129
4.5 Free body diagram of an element from the m^{th} layer in a multilayered beam	130
5.1 Shear buckling of multilayered media	131
6.1 Front view of lamina reinforced test specimens	132
6.2 Alignment plate for fabricating lamina reinforced specimens .	133
6.3 Rear view of lamina reinforced test specimens	134
6.4 Initial transverse displacement for lamina reinforced specimens	135
6.5 Matrix compression test specimen	137
6.6 Matrix shear test specimen	138
6.7 Matrix-reinforcement bond strength specimen	139
6.8 Compression test of a lamina reinforced specimen	140
6.9 Close-up view of a strain gage mounted on the edge of a reinforcing lamina	141
6.10 Strain gages on lamina reinforced specimen	142
6.11 Compression test of a matrix specimen	143

FIGURE	PAGE
6.12 Torsion test of a matrix specimen	144
6.13 Bond strength test setup	145
6.14 Flow diagram of process for fabricating uniaxial filament- reinforced epoxy tubes	146
6.15 Photomicrographs of tube cross sections	147
6.16 End plug	148
6.17 Boron-epoxy tubular specimens	149
6.18 S-glass-epoxy tubular specimens	150
6.19 Compression test of a boron-epoxy tubular specimen	151
6.20 Torsion test of a boron-epoxy tubular specimen	152
6.21 Combined compression and torsion test of a boron-epoxy tubular specimen	153
7.1 Multilayered beam utilized to generate theoretical results	154
7.2 Shear stress distribution at $x = L/4$	155
7.3 Interlaminar shear stress based on linear stress-strain behavior	156
7.4 Nonlinear shear stress-strain curve used to generate theoretical results	157
7.5 Effect of nonlinear stress-strain behavior on interlaminar shear	158
7.6 Effect of nonlinear stress-strain behavior on shear instability load	159
7.7 Compressive stress-strain curves for matrix material	160
7.8 Compressive stress-strain curve for matrix material	161

FIGURE	PAGE
7.9 Shear stress-strain curve for matrix material	162
7.10 Shear stress-strain curve for matrix material (curve terminated at 0.012 strain)	163
7.11 Piecewise linear representation of the shear stress-strain curve for the matrix	164
7.12 Shear stress-head displacement plot for aluminum-wax bond strength specimen	165
7.13 Laminate specimen 1 after failure	166
7.14 Enlarged view of laminate specimen 1 after failure	167
7.15 Enlarged view of laminate specimen 2 after failure	168
7.16 Laminae from specimen 1	169
7.17 Laminate specimen 4 after failure	170
7.18 Enlarged view of laminate specimen 4 after failure	171
7.19 Laminae from specimen 4	172
7.20 Load-strain plots for laminate specimen 1	173
7.21 Load-deflection plots for laminate specimen 1	175
7.22 Load-shortening plot for laminate specimen 1	176
7.23 Load-strain plots for laminate specimen 2	177
7.24 Load-deflection plots for laminate specimen 2	178
7.25 Load-shortening plot for laminate specimen 2	181
7.26 Load-strain plots for laminate specimen 3	182
7.27 Load-deflection plots for laminate specimen 3	183
7.28 Load-shortening plot for laminate specimen 3	185
7.29 Load-strain plots for laminate specimen 4	186

FIGURE	PAGE
7.30 Load-deflection plots for laminate specimen 4	187
7.31 Load-shortening plot for laminate specimen 4	189
7.32 Failed boron-epoxy compression specimen (4 mil fiber) . .	190
7.33 Failed boron-epoxy compression specimen (5.6 mil fiber) .	191
7.34 Failed glass-epoxy compression specimen	192
7.35 Compressive load-strain plots for boron-epoxy specimen 1-1	193
7.36 Compressive load-strain plots for boron-epoxy specimen 1-2	194
7.37 Compressive load-strain plots for boron-epoxy specimen 1-3	195
7.38 Compressive load-strain plots for boron-epoxy specimen 2-1	196
7.39 Compressive load-strain plots for boron-epoxy specimen 2-2	197
7.40 Compressive load-strain plots for boron-epoxy specimen 2-3	198
7.41 Compressive load-strain plots for glass-epoxy specimen 3-1	199
7.42 Compressive load-strain plots for glass-epoxy specimen 3-2	200
7.43 Compressive load-strain plots for glass-epoxy specimen 3-3	201
7.44 Failed boron-epoxy torsion specimen	202
7.45 Failed glass-epoxy torsion specimen	203
7.46 Shear stress-strain curve for boron-epoxy (4.0 mil filaments)	204
7.47 Shear stress-strain curve for boron-epoxy (5.6 mil filaments)	205
7.48 Shear stress-strain curve for glass-epoxy	206
7.49 Shear stress-strain curve for boron-epoxy (4.0 mil filaments)	207
7.50 Torque-strain plots for boron-epoxy specimen 1-5	208

FIGURE	PAGE
7.51 Effect of axial compressive stress on the shear modulus of boron-epoxy	209
7.52 Effect of axial compressive stress on the shear modulus of boron-epoxy	210
7.53 Effect of axial compressive stress on the shear modulus of glass-epoxy	211
7.54 Effect of axial compressive stress on the shear modulus of glass-epoxy	212
7.55 Laminate cross section used to represent boron-epoxy in the interlaminar shear stress analysis	213
7.56 Shear stress-strain curve used to represent behavior of epoxy in the interlaminar shear analysis	214
7.57 Effect of axial compressive stress and fiber curvature on shear modulus for laminate model of boron-epoxy	215
A.1 Flow diagram of interlaminar shear stress program	216
B.1 Free body diagram of beam, case A boundary conditions	219
B.2 Free body diagram of beam, case B boundary conditions	220
C.1 Method for determining fiber curvature	221
C.2 Fiber coordinates	222
 TABLE	
6.1 LAMINATE SPECIMEN DIMENSIONS	110
6.2 CONSTITUENT PROPERTIES AND CURE CYCLES FOR PREPREG TAPES	112
6.3 FIBER REINFORCED SPECIMEN DIMENSIONS AND TEST RESULTS	113

TABLE	PAGE
7.1 THEORETICAL RESULTS FOR AN EIGHT LAYER SYMMETRIC BEAM . . .	114
7.2 INFLUENCE OF LOAD INCREMENT SIZE ON RESULTS FROM THE INTERLAMINAR SHEAR STRESS COMPUTER PROGRAM	116
7.3 INFLUENCE OF BOUNDARY CONDITIONS ON DISPLACEMENT, ROTATIONS, AND INTERLAMINAR SHEAR STRESS	117
7.4 LAMINATE SPECIMEN TEST RESULTS	118
7.5 COMPARISON OF THEORY WITH LAMINATE SPECIMEN TEST RESULTS .	119
7.6 EFFECT OF AXIAL COMPRESSIVE STRESS AND FIBER CURVATURE ON SHEAR MODULUS	120
C.1 FIBER COORDINATES	121

I. INTRODUCTION

For slightly over a decade, materials and structural engineers in the aerospace community have been focusing attention on fiber reinforced composite materials. This interest has largely been stimulated by the potential improvements in strength to density and stiffness to density ratios offered by the class of materials. Numerous papers, which deal with the behavior of such materials, have been prepared. While the state of the art in predicting the mechanical behavior of composites has moved forward at a rapid rate during the past decade, there are still some unresolved areas, notably analyses for predicting failure strength.

The purpose of this thesis is to report the results of an investigation on the compressive strength of uniaxial fiber reinforced and lamina reinforced composites when loaded parallel to the reinforcement. In the section which follows, a comprehensive review of previous research on the subject is presented. An analytical model which provides substantial insight into the response of uniaxial composites under compressive load is postulated. Derivation of the governing equations, boundary and initial conditions, casting the governing differential equations into finite difference equations and a computer solution to the equations are discussed. Theoretical predictions are compared with results for boron-epoxy, glass-epoxy and aluminum-wax specimens tested in axial compression.

Perhaps a few words on the physical arrangement of typical fiber reinforced composites are in order before proceeding to the next

section. Figure 1.1 shows cross sections of composite materials that are currently receiving considerable attention in the aerospace community. Three of the composites have a resin (epoxy) type matrix whereas the fourth has a metal (aluminum) matrix. Each material is built-up from a series of layers or laminae. For the boron filament reinforced epoxy, each lamina consists of a single row of filaments. In the graphite composite, each ply consists of a row of yarns. In the glass fiber composite, each layer contains a number of rovings that have been laid side by side. Due to the irregular spacing of the fibers in the matrix, it is the opinion of the author that it would be impossible to postulate a simple mathematical or physical model that would be capable of completely explaining the material behavior. As previously indicated herein, it will be shown that it is possible to postulate a model which provides substantial insight into the material response to compressive load in the direction of the fibers.

II. REVIEW OF LITERATURE

The behavior of unidirectionally fiber reinforced composite materials when subjected to an axial compressive loading parallel to the fibers has been investigated both analytically and experimentally during the past decade. Following is a chronological review of the literature which has proposed methods for predicting strength or modes of failure.

A. Chronological Review

In 1960, Dow and Gruntfest (1) proposed two possible modes of failure. One was based on the premise that as the composite is compressed in the direction of the fibers, the high Poisson's ratio of the matrix relative to the fibers creates a tensile stress on the bond between fibers and matrix which tends to produce internal separation failures between them. The second mode of failure was based on the argument that the compressive load is carried by fibers which behave like columns supported within a continuous elastic foundation provided by the matrix and consequently strength is limited by the stability of the fibers. The latter mode has received substantial study in the ensuing years whereas the other mode has received only limited attention.

Using analysis contained in reference (2), Dow and Gruntfest derived the formula

$$\sigma_f = k \sqrt{E_f E_m} (r_f / A_f) \quad (2.1)$$

where

σ_f = failure stress (buckling) in the fiber

k = constant

E_f = Young's modulus of the fiber

E_m = Young's modulus of the matrix

r_f = radius of gyration of the fiber

A_f = cross sectional area of the fiber

Equation (2.1) by itself did not permit direct calculation of σ_f since the value of k was unknown. However, it did offer insight into some of the variables that influence compressive strength and it was used for this purpose in reference (1).

Elkin (3) examined NOL rings that had been tested in compression to failure. He concluded that failure was a consequence of fiber buckling followed by shear and tension rupture of the matrix. Analysis for predicting compressive strength was not presented.

Fried (4) in 1963 published the results of an experimental study on compressive strength. Axial compression tests were performed on 1/2 in. x 1/2 in. x 1 in. blocks of polyester resin reinforced with either a 1/8 in. diameter drill rod, a 3 mm diameter pyrex glass rod or a single strand of E-glass roving. Each type of specimen failed at or near the yield strain of the unreinforced matrix. Fried reasoned that as the yield point of the matrix is approached, it begins to flow and thus ceases to support the fibers. Therefore, it was proposed that compressive strength could be predicted using the rule of mixtures and the following equation was presented.

$$\sigma = \sigma_{my} \left[1 + V_f (E_f/E_m - 1) \right] \quad (2.2)$$

where

σ_{my} = yield strength of the matrix

V_f = volume fraction of fiber

Realizing that his data had been obtained on very low volume fraction specimens, Fried suggested that the value computed from the rule of mixtures should serve as an upper bound. Equation (2.2) does not agree well with experimental data on high volume fraction specimens and does not take into account variables, other than volume fraction, matrix modulus and yield strength, which influence compressive strength.

In spite of the deficiencies just mentioned, Fried did make a valuable contribution to the subject by putting forth ideas which have since been used in micromechanics analyses of the subject. These ideas include: (1) The fibers behave as long slender columns which are supported laterally by the matrix. This thought appears to have been obtained independent of reference (1). (2) Compressive strength is influenced by the compressive yield strength and shear strength of the matrix. (3) An optimum fiber geometry and volume fraction exist.

One year later, in 1964, Fried and Kaminetsky (5) presented experimental results that substantiated several of the ideas postulated in reference (4). Existence of an optimum fiber volume fraction was demonstrated. In addition, it was clearly shown that compressive strength increases with increasing resin yield strength for the range of values investigated.

Rosen (6) was the first to propose an analysis that permitted estimation of compressive strength without requiring the use of

empirical factors. He suggested that the composite material be represented by a laminate consisting of alternating hard and soft laminae. The hard laminae represent fibers whereas the matrix is simulated by the soft laminae. Thus, it was proposed that a two dimensional model be utilized to represent a three dimensional problem. Two modes of failure were postulated, extension instability and shear instability. For the extension mode, which is analogous to column buckling of a beam supported by an elastic foundation, adjacent fibers are assumed to buckle out of phase and thus subject the matrix to extension deformations transverse to the fibers. For the shear mode, adjacent fibers are assumed to buckle in phase and subject the matrix to shearing deformations.

By using the energy approach, assuming linear elastic behavior for both fiber and matrix, and assuming the fiber to be much stiffer than the matrix, Rosen (6) developed the following equations for predicting compressive strength. For the extension mode

$$\sigma = 2V_f \left[\frac{V_f E_f E_m}{3(1-V_f)} \right]^{1/2} \quad (2.3)$$

and for the shear mode

$$\sigma = \frac{G_m}{1-V_f} \quad (2.4)$$

where

σ = compressive strength of the composite

G_m = shear modulus of the matrix

and the remaining symbols have already been defined herein. The lower value predicted by equations (2.3) or (2.4) gives the best estimate for compressive strength. For most materials of interest, equation (2.4) yields the lower prediction and consequently has received the most attention.

Examination of equation (2.4) and subsequent comparison with experimental data indicates the following deficiencies:

1. Elastic properties of the fiber are not taken into account.
2. Effects of fiber geometry (diameter and straightness) are neglected.
3. Nonlinear behavior of most matrix materials is neglected.
4. Experimentally determined values of strength are generally one-third to one-half the value predicted by equation (2.4).

Rosen realized item number 3 above and offered the suggestion that the shear modulus be varied linearly from its elastic value at an axial strain of one percent to zero at an axial strain of five percent.

In addition to the analysis, reference (6) presented photoelastic stress patterns for glass fibers in an epoxy matrix to illustrate that instability type failure could be expected when the material is subjected to compressive loading.

Data and analysis appearing in reference (6) are also contained in reference (7).

A correlation between compressive strength and behavior in transverse shear was given by Fried (8). His results were obtained from

tests on orthogonal glass filament reinforced epoxy laminates. A linear relationship between compressive strength and interlaminar shear strength was observed. Both types of strength were shown to decrease linearly with increasing void content. One would anticipate that an increase in resin shear strength and fiber to resin bond strength would be accompanied by an increase in interlaminar shear strength and consequently an increase in compressive strength.

Further emphasis on composite failure by buckling of the filaments was presented by Ekvall (9). Failed specimens were examined and found to contain buckled filaments. Using analysis presented in reference (2), a comparison of the predicted and measured buckle length was made. Agreement was good. However, the problem of predicting compressive strength was not addressed in reference (9).

Schuerch (10), apparently working independently, used the same model as Rosen (6) and arrived at the same results for composites that are not subjected to inelastic deformations prior to failure. To include the effects of nonlinear behavior, Schuerch (10) proposed that the tangent shear modulus be used in equation (2.4). He assumed isotropic behavior in the nonlinear portion of the stress-strain curve for the matrix material. That is

$$G_{mt} = \frac{E_{mt}}{2(1 + \nu)} \quad (2.5)$$

where

G_{mt} = tangent shear modulus for the matrix material

E_{mt} = tangent modulus for the matrix material

μ = Poisson's ratio for the matrix material

Results of compression tests on two boron filament reinforced magnesium specimens are reported in reference (10). The measured strengths are in reasonable agreement with the predicted strengths based on tangent moduli values. As Schuerch points out, it is perhaps fortuitous that experiment and theory were in agreement, especially when the failure strain of the composite was approximately four times the yield strain of the matrix.

Data and analysis appearing in reference (10) are also contained in reference (11).

Another approach for predicting compressive strength, which consists of treating the composite material as a beam column with low shear stiffness, was presented in reference (12). For columns which buckle elastically, the analysis can readily be found in many engineering texts. (See for example, reference (2).) It was proposed in reference (12), that predictions for columns which fail inelastically be based on tangent shear moduli. Isotropic relationship between extensional and shear stiffnesses in the inelastic region was assumed. In an attempt to account for the effect of voids in the matrix material and the effect of filament misalignment; influence factors were incorporated in the analysis. The authors of reference (12) were apprehensive about applying the analysis as the column aspect ratio approached zero. This is believed to be a consequence of focusing attention on the fiber diameter rather than the overall dimensions of the column.

Most of the experimentally determined compressive strengths reported in reference (12) were obtained on NOL ring type specimens loaded in diametrical compression. Scatter in the measured strengths was such that comparison with theory could only be made on a statistical basis.

Perhaps the most important experimental data presented in reference (12) are the photographs of plexiglass reinforced rubber laminates under varying amounts of compressive load. These pictures clearly show that the reinforcing material, plexiglass, deforms laterally at loads below the maximum compressive load supported. In other words, there must have been some initial curvature in the plexiglass laminae which increased in magnitude as the compressive load was increased. Since lateral deformation of the reinforcing laminae is accompanied by shearing deformations in the matrix material, the shear stiffness of the composite would decrease with increasing compressive load if the matrix material exhibits inelastic behavior in shear. It appears reasonable to assume that fiber reinforced materials would exhibit the same type behavior. Fiber collimation is usually better for large diameter fibers (.004 in.) than for small diameter fibers (.0004 in.). Consequently, one might expect an optimum fiber diameter to exist for a given material combination since compressive strength would increase with increasing fiber diameter until the fibers start to fail in bending. This phenomenon had been suggested by Fried (4) and had been proven experimentally by Levenetz (13).

Utilizing mechanics of incremental deformations, Biot (14) developed equations for predicting the stability of a multilayered media. The multilayered media could represent the model used by Rosen (6). In his

analysis, Biot assumed both media to be incompressible and the buckle wave length to be large compared to the thickness of either layer. The results of Biot's analysis can be written in the form

$$\sigma = \frac{G_m}{1 - V_f} \left[\frac{1 + n(1 - V_f)/V_f}{1 + n^2 + \frac{n(1 - 2V_f)^2}{2V_f(1 - V_f)}} \right] \quad (2.6)$$

where

$$n = \frac{G_m}{G_f} \quad (2.7)$$

If the ratio of fiber to matrix stiffnesses is large, the value of n approaches zero and equation (2.6) reduces to equation (2.4) which was derived by Rosen (6). It should be noted that for most materials combinations of current interest, the bracketed term in equation (2.6) ranges from approximately 1.005 to 1.045. Obviously, equation (2.6) has the same deficiencies as equation (2.4).

An indepth discussion of factors influencing the compressive strength of filament reinforced composites is given by Foye (15). Using the energy method of analysis and treating the composite as a macroscopic, homogeneous, orthotropic material Foye showed that the compressive strength should equal the shear modulus of the composite. That is

$$\sigma = G \quad (2.8)$$

where

G = shear modulus of the composite

Assuming the Reuss or "stiffnesses in series" model the shear stiffness of the composite is related to the constituent stiffnesses by the following equation.

$$G = \frac{G_m}{(1 - V_f) + V_f (G_m/G_f)} \quad (2.9)$$

Substituting equation (2.9) into (2.8) yields

$$\sigma = \frac{G_m}{(1 - V_f) + V_f (G_m/G_f)} \quad (2.10)$$

As indicated by Foye, equation (2.10) reduces to equation (2.4) when $G_f \gg G_m$. When equation (2.4) was derived, the strain energy due to shearing stresses in the filaments was neglected. For most materials currently of interest the second term in the denominator of equation (2.10) can be neglected. However, as the volume fraction approaches unity and/or the shear modulus of the fiber is of the same order of magnitude as that of the matrix the term becomes important.

In addition to the analysis discussed to this point, reference (15) also focused attention on the effects of voids, fillers and whiskers on compressive strength. In general voids are expected to decrease strength whereas fillers and whiskers may be used to improve strength.

In yet another attempt to bring experiment and theory closer together, Dow. et al. (16) suggested that a matrix "characteristic stress" be included in the analysis and the following equation for predicting strength was offered:

$$\sigma = \left[\frac{v_f E_f \sigma_y}{3(1 - v_f)} \right]^{1/2} \quad (2.11)$$

where

σ_y = matrix "characteristic stress" level

For elastic perfectly plastic materials, the characteristic stress was identified as the yield stress. No suggestion was offered for materials exhibiting other types of stress-strain behavior. Equation (2.11) can be derived from equation (2.4) when the following assumptions are made:

1. The matrix material exhibits isotropic behavior and is incompressible after yielding.
2. Axial strains in the matrix and fiber are equal.

The major fallacies associated with using equation (2.11) is that most matrix materials currently of interest do not exhibit elastic perfectly plastic behavior, hence determining σ_y remains unresolved, and the effect of residual tensile stresses in the matrix from curing the composite at elevated temperature is not taken into account.

Two problems related to the compressive strength of a single wire embedded in a soft matrix material were studied by Hermann, Mason, and Chan (17). First the beam-column behavior of an initially crooked wire embedded in a matrix and subjected to a state of uniaxial stress was investigated. Second, the possibility of buckling, within the matrix, of a compressively loaded straight wire was considered. Three dimensional elasticity was used to predict the foundation (matrix) behavior in both cases. Two major conclusions were reached. One, if the ratio

of the shear moduli of the matrix and fiber is sufficiently low (plots were based on 0.00033) a substantial difference in the compression and tension stress strain curves can be expected. Second, again for low ratios of shear moduli, failure can be expected at stress levels well below the buckling stress of a straight fiber. When evaluating the significance of the conclusions and analysis put forth in reference (17), one should keep in mind that the ratio G_m/G_f for most materials of current interest is on the order of 0.01 or greater, two orders of magnitude greater than the values considered in reference (17). Also, the influence of surrounding fibers on the particular fiber being investigated was not taken into account.

Results reported in reference (17) are also found in reference (18).

Sadowsky, Pu, and Hussain (19) also investigated buckling of a single fiber embedded in an elastic matrix. The reaction of the matrix was calculated using three dimensional elasticity and the fiber was treated as a beam. Plots were presented for determining if the fiber will buckle due to thermal shrinkage which occurs in cooling the specimen from the curing temperature to room temperature. It was shown mathematically that the buckle wave length is directly proportional to the fiber diameter.

The results and analysis of a brief study on boron-polymer film layered composites was published by Crawford (20). Using the same model as Rosen (6) and Schuerch (10), but considering the reinforcement to have initial waviness, Crawford derived equations for predicting compressive strength, axial stiffness, tensile and shear stresses at the

reinforcement-matrix interface. Crawford obtained the same results as equation (2.3) reported herein for the extension mode of buckling. The equation derived to predict the shear mode of instability differed from equation (2.4) reported herein only by the term $1 + (E_m V_m / E_f V_f)$ which approximates unity for most composites of current interest. It is shown in reference (20) that axial stiffness can be reduced substantially below the value based on the assumption of straight fibers if sufficient waviness is present in the composite. Since the axial stiffness of most fiber reinforced composites can be predicted by the "rule of mixtures" it appears that one need not consider the effect of waviness on stiffness. In other words the waviness is not sufficient to appreciably decrease the stiffness. Plots of tensile and shear stresses at the reinforcement-matrix interface as a function of the waviness parameters were constructed using the material properties and geometry of one test specimen. It was shown that the stresses could reasonably be expected to be of sufficient magnitude to cause failure by delamination.

Perhaps the most important point made in reference (20) was that initial waviness can create stresses which cause the composite to delaminate at loads below those based on buckling analyses. However, this thought was not related to the behavior of filamentary composites in reference (20), possibly due to the brevity of the study. When studying reference (20), one will note that shearing deflections in the reinforcement have been neglected and several equations need minor corrections.

Yue, et al. (21) modified the work of Dow, Rosen, and Haskin (16)

to include linearly strain hardening materials. However, their analysis contains an equation which appears to be incorrect. To be specific, a relationship between longitudinal strain in the fiber and shear strain in the matrix is assumed. For fibers which remain straight prior to buckling, there can be no shearing stresses parallel and perpendicular to the fibers. Thus further discussion of reference (21) is not offered herein.

The results of performing axial compression tests on several different resin systems reinforced with boron filaments were presented by Lager and June (22). They found that Rosen's analysis (6) could be correlated with the data if an influence coefficient of 0.63 were used. Their justification for using the influence coefficient was to account for the differences between a two dimensional model and a three dimensional test specimen. The authors of reference (22) indicated that the influence coefficient is not expected to be the same for all fiber reinforced composites. Obviously, this approach for predicting compressive strength contains the same shortcomings as reference (6).

Chung and Testa (23) investigated the problem of predicting compressive strength for a soft plate (matrix) reinforced by strips of a stiffer (fibers) material. The spacing between fibers was assumed to be large compared to the plate thickness. In their study (23) beam theory was used to describe the behavior of the fibers whereas the matrix behavior was formulated as a generalized plane stress problem. The resulting analysis led to a set of highly intractable transcendental equations. Two possible solutions were obtained, the extensional

mode and the shear mode of fiber buckling. If the wave length of the buckled fiber is large compared to the spacing between fibers and Poisson's ratio is set equal to zero, the equations developed by Chung and Testa (23) can be reduced to equations (2.3) and (2.4) reported herein.

Reference (23) reported experimental data on specimens in which the reinforcement was a glass base sheet (a continuous filament woven glass fabric impregnated with a resin binder) separated by layers of epoxy resin. The comparison between theory and experiment was favorable for the small amount of data presented. However, it should be noted that the material tested differs substantially from the type of unidirectionally fiber reinforced material normally considered for use in primary load carrying structures of aerospace vehicles.

By utilizing the governing differential equations for nonlinear elasticity, Guz (24) was able to derive that the compressive strength of a reinforced composite should equal the shear modulus of the material. Failure planes were predicted to be perpendicular to the fiber direction. Since the end result of reference (24) is the same as that of references (6) and (15), the difference between predicted and measured strengths would be the same as that obtained using the earlier references.

Skudra, et al. (25) proposed that failure in a composite subject to axial compression is by shearing along a plane oriented at 45° to the direction of loading. Using elementary principles of statics and energy methods, one can follow the derivation in reference (25) which leads to the equation

$$\sigma = \frac{E_L E_T \gamma}{E_L (1 + \mu_{TL}) + E_T (1 + \mu_{LT})} \quad (2.12)$$

for predicting compressive strength. Symbols contained in equation (2.12) and not previously identified are as follows:

E_L, E_T = Young's modulus of the composite measured parallel and transverse to the filaments, respectively.

μ_{LT}, μ_{TL} = Poisson's ratio associated with a load applied parallel and transverse to the filaments, respectively.

γ = Limiting shear deformation on a plane oriented at 45° to the direction of the filaments.

The experimental results presented in reference (25) compare quite well with the values predicted by equation (2.12). The test specimens reported in reference (25) failed at stresses less than 20 ksi. However, very poor agreement is obtained when one compares the analysis of reference (25) with test data for S-glass-epoxy presented in reference (26). To be specific, the predicted strength is 17 ksi whereas the measured strength is 207 ksi. Therefore, one must conclude that the analysis presented in reference (25) cannot be used to predict the compressive strength of most materials suitable for use in aerospace structures.

Chamis (27) presented two equations for computing compressive strength. One is a modified rule of mixtures relationship whereas the other relates compressive strength to interlaminar shear strength in the same manner that Fried (8) proposed. The lower of the two values is

recommended for use in analysis. Starting with the following equation:

$$\sigma = \sigma \left[(V, d, n, a)_{f, v}, V_m, (E, \mu, G, F, \epsilon_p)_{f, m}, F_B, F_R \right] \quad (2.13)$$

which is all encompassing, Chamis quickly reduced it to the form:

$$\sigma = \sigma_{mc} \left[\beta_{mc} \bar{V}_m + \beta_{fc} \bar{V}_f (E_f/E_m) \right] \quad (2.14)$$

Symbols appearing in equations (2.13) and (2.14) and not previously identified are as follows:

a_f, a_v = parameter associated with fibers and voids, respectively

d_f, d_v = diameter of fiber and void, respectively

n_f, n_v = number of fibers and voids, respectively

F_f, F_m = compressive strength of fiber and matrix, respectively

F_B = interface bond strength

F_R = residual compressive strength

β_{mc}, β_{fc} = Theory-experiment correlation factor for matrix and fiber, respectively

ϵ_p = limiting strain

$$\bar{V}_m = (1 - V_v)(1 - V_f) \quad (2.15)$$

$$\bar{V}_f = (1 - V_v) V_f \quad (2.16)$$

Chamis offered the following argument for reducing equation (2.13) to (2.14). The void content, bond strength and residual stress are dependent on the fiber surface treatment, matrix additives, hardeners,

temperature, and pressure used during fabrication and method of fabrication. In other words, the list of variables on which strength depends is quite long. By assuming that void size and distribution, filament spacing nonuniformity, interface bond strength, and residual stress are influenced by the particular fabrication process used Chamis reasoned that all of these variables could be grouped into theory-experiment correlation factors shown in equation (2.14).

In recognition of Fried's earlier work (8), Chamis presented the following equation:

$$\sigma = a_1 \tau_{12} + a_2 \quad (2.17)$$

where

a_1, a_2 = empirical curve-fit parameters

τ_{12} = interlaminar shear strength

One would expect that data over a limited range of fiber volume fraction could be fitted by equations (2.14) and (2.17). However, these equations provide only limited insight into the variables which effect compressive strength and thus do not contribute significantly to the knowledge of failure mechanics of composites.

Essentially, the same analysis that was presented in reference (24) is contained in reference (28). In addition, reference (28) presents experimental data on the compressive strength of fiberglass reinforced epoxy. Although the measured strengths are only about 20 percent of the predicted values, the authors claim the proposed theory explains quite well the nature of the failure for the material under investigation.

DeFerran and Harris (29) in a study of the compressive strength of steel wire reinforced polyester resin indicated that most of the analyses discussed previously herein are inadequate for predicting strength. The experimental data reported in reference (29) is in agreement with calculations based on the rule of mixtures using the tensile strength of the steel wire. For specimens containing cold-drawn wire the yield strength was used whereas the ultimate strength was used in calculations for specimens reinforced with annealed wire.

It is perhaps fortuitous that the authors of reference (29) were able to obtain agreement between the rule of mixtures and experiment. There are data reported in the literature that obviously would not correlate. For example, Leventz (13) reported compressive strengths for both 0.005-inch diameter and 0.0004-inch diameter glass fiber reinforced composites. Tensile strength for the 0.005-inch diameter fiber was reported to be slightly less than 60 percent of the value reported for the 0.0004-inch diameter fiber. Yet the compressive strength of the 0.005-inch diameter fiber reinforced composite was approximately twice that of the composite reinforced with 0.0004-inch diameter fibers.

Results of compressive tests on S-glass-epoxy and boron-epoxy tubular specimens are presented in reference (30). By taking the limit as the column length to diameter ratio approaches zero, it was shown that the compressive strength should be given by the equation

$$\sigma = G/B \quad (2.18)$$

where

β = ratio of maximum shear stress to average shear stress in a buckled column

Equation (2.18), like most of the equations previously derived for predicting strength, provided estimates that substantially exceed the measured values of strength. It was shown in reference (30) that the compressive strength and column buckling data correlated reasonably well with analysis when a value equal to one-half the measured shear modulus was utilized in the calculations. At the time reference (30) was published, the author had not developed the rationale for considering the shear modulus to decrease with increasing axial strain. Assuming the fibers to be initially curved provides the missing link and this will be explained in more detail later in this paper.

Pinnel and Lawley (31) presented results of compression tests on aluminum reinforced with stainless-steel wires. The authors found that equation (2.11) reported herein correlated well with experimental results when the "characteristic stress" was assumed to equal the "flow stress" of the aluminum matrix. Unfortunately, when one observes the axial stress-strain curve for the aluminum alloy reported in reference (31), it is found that the value given for the "flow stress" has no distinct characteristic. In other words, it is doubtful that one could predict the "flow stress" without first knowing the compressive strength of the composite.

Hayashi (32) proposed that a unidirectionally fiber reinforced composite loaded in compression parallel to the fibers fails when the shear instability limit of the matrix material is reached. Hayashi

reasoned that as the compressive stress in the matrix approached the shear instability limit the matrix would cease to support the fibers. Fiber buckling would immediately follow and consequently failure of the composite. In an earlier paper (33), Hayashi like Biot (15), Guz (24), and Guz (28) had shown that the shear instability limit equals the shear modulus. In reference (32), it was assumed that the shear modulus decreases as compressive stress is increased. The following equation was offered as an approximation of the relationship:

$$G_m(\sigma_m^*) = \frac{G_m}{\left[1 + (\sigma_m/\sigma_{my})^3\right]^{a_3} (a_3 + 1)/a_3} \quad (2.19)$$

where

a_3 = an undefined constant

By assuming equal strain in the matrix and fibers at failure and using the rule of mixtures Hayashi (32) concluded that compressive strength should be predicted by the expression

$$\sigma = \sigma_f^* V_f + (1 - V_f) \sigma_m^* \quad (2.20)$$

where σ_f^* is the fiber stress corresponding to matrix strain at the shear instability limit, σ_m^* .

A comparison between the analysis of reference (32) and experimental data reported in reference (22) is presented in reference (32). According to Hayashi (32) the comparison is more reasonable than one would obtain using equations (2.3) or (2.4) reported herein. In spite of this

optimistic opinion put forth by Hayashi, there appears to be some doubt as to the validity of the analysis. For example using the analysis and material properties presented in reference (32) to predict failure for a boron-epoxy composite containing 40 percent fibers by volume, one easily calculates the failure strain to equal approximately 0.04. Examination of test data for the same material, reference (22), indicates that axial strain at failure was less than 0.01. This discrepancy was not addressed in reference (32).

Starting with the governing equations for elasticity, Guz (34), develops an expression for computing the shear buckling mode of failure for a fiber reinforced matrix material with uniformly spaced circular fibers. In reference (35), Guz compares the results with prior studies reported in references (6) and (24). For certain values of stiffness ratio and fiber volume fraction substantial differences are noted. However, the results are very limited and do not support general conclusions.

The results of an investigation on specimen geometry and load introduction for unidirectional carbon fiber reinforced plastic are reported in reference (36). A suitable test specimen was identified for the material tested. Experimentally determined compressive strength values were approximately one quarter of the values computed by the analysis of reference (6).

Evidence of shear buckling due to compressive loading of Al-CuAl₂ specimens is reported in reference (37). Experimentally determined strengths are compared with values predicted by the analysis of

reference (21). Since the analysis of reference (21) appears to contain an incorrect equation, the comparison will not be discussed herein.

Results obtained from compression tests on steel wire reinforced epoxy and glass rod reinforced epoxy are reported and compared with existing theoretical predictions in reference (38). The data indicate substantial scatter in failure loads and does not appear to warrant definite conclusions. The author puts forth the idea that failure may be associated with transverse tensile stresses due to mismatch between Poisson's ratios for the fiber and matrix.

Greszczuk provides a brief review of prior investigations on compressive strength and presents experimental data obtained on model composites in reference (39). The behavior of graphite rod and steel rod reinforced epoxy and urethane specimens were studied. The data obtained follow the same trends as predicted for microbuckling failure of the reinforcing rods. Small prebuckling deformations in the rods were shown to significantly reduce the compressive strength of the model. Greszczuk continued the study initiated in reference (39) and the results of further effort are reported in reference (48) discussed herein.

Results of tests and analyses on the compressive strength of boron-epoxy composites are reported in reference (40). Of the several failure modes discussed, only filament fracture and layer instability appear to be related to material failure. Filament fracture is reported to have been observed in some specimens tested at room temperature and -67°F and to have occurred at a stress of 600 ksi in the composite. This

corresponds to a strain of 0.02 inch/inch. Layer instability, buckling of the outermost ply away from the remaining plies, was analyzed by treating the buckled ply as a beam with finite shear stiffness and the remaining plies as an elastic foundation. The subsequently derived equations are

$$\sigma = G_z \xi (2 - \xi) , \xi < 1 \quad (2.21)$$

$$\sigma = G_z , \xi \geq 1 \quad (2.22)$$

where G_z denotes the "interlaminar shear modulus" as defined in reference (41) and ξ denotes a stiffness parameter defined in reference (40). Based on the analyses presented in reference (40), one would expect the value of G_z in equation (2.22) to equal the shear modulus of the composites. However, the value of G_z reported in reference (40) ranges from 44 to 67 percent of the shear modulus. Experimentally determined values of compressive strength reported in reference (40), agree quite well with the predictions of equation (2.22). However, the analysis provides only limited insight into the parameters which influence compressive strength.

Sednor and Watterson studied the compressive fatigue behavior of $0^\circ - 90^\circ$ glass-epoxy laminates and the results are presented in reference (42). They conclude, based on examination of numerous photomicrographs of failed specimens, that compressive failure is probably initiated by debonding at the matrix-fiber interface followed by buckling of the unsupported fiber.

Prebuckling and postbuckling behavior of a single reinforcing fiber

surrounded by a matrix material was investigated analytically by Lavir and Fung (43). The authors point out that buckling of the fiber is possible if it is not supported by the surrounding matrix (debonded). However, the authors also conclude that in common composite materials the buckling of fibers will have no significant effect on the overall behavior of the composite in the linear elastic range. Although, not discussed in detail, Lanir and Fung conclude that fiber buckling will significantly affect the behavior of the composite when loaded in the plastic range.

Harris (44) provides a brief review of previous work on compressive strength. Specifically the papers by Rosen, Yue, Lager and June, DeFerran and Harris, and Hayashi are noted.

Photomicrographs of tungsten wire reinforced aluminum and stainless steel reinforced aluminum specimens that had been loaded to failure in axial compression are presented in reference (45). The photographs show that the mode of failure was microbuckling of the reinforcement.

Additional evidence to support microbuckling as a possible mode of failure in metal matrix composites is presented in reference (46) which reports the results of axial compression tests on tungsten fiber reinforced copper. The authors did not offer a comparison between theory and experiment.

Yet another analysis of the buckling of a single fiber embedded in a matrix material is presented in reference (47). Experimental results obtained from photoelastic stress analysis are compared with predictions from finite element analysis. In general the comparison

ranges from fair to reasonable. No attempt is made to extrapolate the results to composite materials currently under investigation.

Greszczuk (48) conducted an experimental and theoretical investigation on aluminum lamina-epoxy, aluminum rod-epoxy, graphite rod-epoxy and graphite fiber-epoxy composites. Variables and initial imperfections studied include rod diameter, volume fraction, lamina thickness, number of rods contained in a specimen, bowed rods, misaligned rods, unbonded rods and fiber twist.

Utilizing a low modulus resin ($E = 2500$ psi) Greszczuk showed that the failure mode for the lamina and rod reinforce composites is microbuckling and that failure can be predicted by the analyses previously developed by Rosen (reference (6)). As the resin modulus was increased to 62,000 psi, Greszczuk reports the failure mode changed to compressive strength failure of the reinforcement. For specimens that failed by microbuckling, the compressive strength was shown to increase with increasing rod diameter. This effect may be associated with fewer initial imperfections in the specimens containing the larger diameter rods. It was also shown that the compressive strength of 0.078 in. diameter aluminum rod-epoxy specimens could be reduced by more than forty percent by bending the rod to an arc height of 0.020 in. over a 2.5 in. span. The compressive strength of a graphite rod reinforced specimen, which had been fabricated in such a manner that the resin and rod were not bonded, was essentially equal to the value measured for specimens in which the rod and matrix were initially bonded. Thus Greszczuk concluded that, debonding of the rod and matrix occurred

prior to microbuckling in the latter group of specimens.

Experimentally determined compressive strengths for the graphite fiber-epoxy specimens ranged from 56 to 62 ksi compared to a predicted value of 290 ksi for the microbuckling mode of failure. As a result, other modes of failure were investigated. It had been shown earlier, reference (49), that an applied axial compressive stress induces tensile stresses in the transverse direction. After observing failed specimens, Greszczuk proceeded to compute a failure stress based on the maximum induced tensile stress in the transverse direction. Starting with the failure criterion developed by Norris, reference (50), the following equation for predicting failure was derived.

$$\sigma_L = \frac{F_{Lc} F_{Tt}}{\left[F_{Tt}^2 + 2k F_{Lc} (k\beta F_{Lc} - F_{Tt}) \right]^{1/2}} \quad (2.23)$$

F_{Tt} and F_{Lc} are defined as the ultimate composite strength in the transverse direction and the true ultimate compressive strength in the fiber direction, respectively. β and k are the ratios of maximum transverse tensile stress in the resin to the applied axial stress and uniformly applied transverse tensile stress to the maximum transverse tensile stress in the resin. The major difficulty in using equation (2.23) is determining the value of F_{Lc} . Greszczuk assumed that the compressive and tensile strengths of the graphite fiber are equal and then used the rule of mixtures to compute F_{Lc} . Values computed in this manner ranged from 10 percent below to 33 percent greater than experimentally determined values.

Reference (51) presents another derivation of the shear mode of instability for a fiber reinforced column loaded in axial compression. The results are in agreement with earlier derivations.

Argon (51) argues that the earlier analysis of Rosen (6) should be considered as an upper bound since composites made by normal manufacturing techniques will always contain regions in which the reinforcing filaments are not parallel and aligned with the load axis. He further states that such regions will form a failure nucleus by kinking similar to that previously observed in metal crystals. The failure is reported to resemble in form the in-phase internal buckling of Rosen (6) but to occur at much lower stress. Utilizing energy analyses developed in fundamental studies of metallurgy, Argon estimates the compressive strength, σ , to be

$$\sigma = \tau_{LT} / \phi_0 \quad (2.24)$$

where τ_{LT} denotes the interlaminar shear strength of the laminate and ϕ_0 is the angle of misalignment between the reinforcement and the load axis. The kinking mode of failure has been observed in boron-polyimide-epoxy film laminates. However, with the exception of some recent studies (53) on FRD-49 fiber-epoxy composites the failure mode has not been observed in most composites of current interest to the aerospace community.

B. Summary

Based on the references reviewed herein, it is readily apparent that a unified theory for the prediction of compressive strength for

fiber reinforced or laminate reinforced composites does not exist. However, several important points emerge from the survey. In general, the evidence tends to support three modes of failure, microbuckling of the reinforcement, delamination, and fiber-matrix separation followed by microbuckling of the fiber. Also, a direct relationship between compressive strength and interlaminar shear strength is noted for some materials. Study of these points lead to postulation of an analytical model which allows microbuckling and/or delamination as potential failure modes and provides an explanation for the relationship between interlaminar shear and compressive strength. The model is described in the next section of this paper.

III. ANALYTICAL MODEL

The model postulated herein is compared with the one utilized by Rosen (6) in figure 3.1. In each the composite is built-up from a series of hard and soft laminae. Rosen assumed that the laminae were initially straight and predicted two buckling modes. Positive and negative features of the Rosen model are listed in figure 3.1. First the advantages: Strength is related to the matrix properties and the resulting equations are simple to use. As for disadvantages, predicted values are usually much larger than experimental measurements, fiber geometry is not taken into account and nonlinear behavior of the matrix is neglected.

The present model permits the laminae to contain initial curvature. Under an increasing axial load, the laminae deflect until one of two failure modes is experienced. These are shear buckling or delamination. The extension mode of buckling has not been observed or predicted to occur in most materials of interest and hence is not discussed further. If the matrix material behaves in a nonlinear manner, one can see that the shear modulus of the composite and consequently the buckling stress of the composite will decrease as axial load is applied. One can also see that interlaminar shear stresses increase as the axial load is increased.

Important features of the present model include: (a) strength is related to constituent properties and geometry. (Both the fiber and matrix material properties are taken into account. Filament size, initial curvature and collimation are reflected in the value of a_0 and

L .) (b) An explanation for the relation between compressive strength and interlaminar shear strength is offered. (c) A decrease in shear modulus with increasing applied axial load is explained. (d) The equations for computing buckling and delamination can be programmed on a computer to provide easy utilization by materials engineers. The major disadvantage of the model is that it contains only two dimensions whereas the filamentary composite is a three dimensional material. However, it is the opinion of the author that the model used herein will be adequate in many cases, as will be shown. In addition to providing useful information on filamentary composites, the model will obviously provide results on laminated media.

Two approaches will be used to compute the stress distribution in the model. In the first, designated case A, the entire laminate is subdivided into the desired number of layers and the stresses and displacements in each layer are computed. Thus, case A takes into account the free boundaries of the model. In the second, designated case B, a repeating element in the model is identified and then subdivided into layers. The repeating element consists of one fiber layer sandwiched between two half layers of matrix material. Continuity of displacements along the edges of the repeating element is imposed on the solution.

IV. INTERLAMINAR SHEAR

Stresses and displacements in the analytical model were determined using the following method of analysis. First, the model was considered to be a multilayered beam. Then the equilibrium equations based on the assumptions of Timoshenko (54) were applied to each layer. Next, the resulting differential equations were expressed in finite difference form. Finally, the resulting set of algebraic equations were solved with the aid of a digital computer. This method of analysis had been used by Heller and Swift (55) (56) (57) previously to investigate the behavior of laminated beams under transverse loading.

Figure 4.1 shows the laminated beam models used to represent the composite material. For case A, the composite is represented by a series of alternating fiber and matrix layers. For case B, a repeating element which consists of one fiber and two half layers of matrix is used to represent the composite. Both models are symmetric about the midplane and are initially deflected in the z direction. All layers within the beam are assumed to have the same initial deflection in the z direction and the same initial radius of curvature at any specified value of x.

A. Displacements, Strains, and Stresses

Utilizing the Timoshenko assumptions (54), which state that each layer undergoes transverse deflection and that cross sections initially perpendicular to the neutral axis may rotate with respect to the neutral axis, and the notation of figure 4.2, the displacement within each layer of a multilayered symmetric beam can be written as follows:

(a) Displacement in the length direction of the beam is given by

$$\begin{aligned}
 u_{\pm 1} &= z(\psi_1 - \theta_1) \\
 u_{\pm 2} &= h_2(\psi_1 - \theta_1) + (z \pm h_2)(\psi_2 - \theta_2) \\
 u_{\pm m} &= (z \pm h_m)(\psi_m - \theta_m) \pm \sum_{i=1}^{m-1} (h_{i+1} - h_i)(\psi_i - \theta_i)
 \end{aligned} \tag{4.1}$$

where ψ_i is the angle between the vertical axis and the final position of the deformed cross section of the i^{th} layer, θ_i is the angle between the vertical axis and the initial position of the cross section of the i^{th} layer (the value of ψ_i which represents the initial rotation of the i^{th} layer), h_i is the distance from the neutral axis (midplane of the laminate) to the outer surface of the $(i-1)^{\text{th}}$ layer, z is the transverse coordinate and the positive and negative subscripts refer to layers above and below the midplane, respectively. Note, compression of the beam due to the application of axial end loads was neglected as customarily done in all buckling problems and equations (4.1) represent only displacements due to bending and shearing of the cross section.

(b) Displacements in the beam width direction are assumed to vanish for all layers since the moment of inertia ratio (I_{yy}/I_{zz}) is much larger than unity.

$$v_{\pm m} = 0 \tag{4.2}$$

(c) Transverse displacements are the same for each layer

$$w_{\pm m} = w$$

In addition the transverse displacement is composed of two parts, an initial displacement, w_0 , and the displacement due to loading, w_1 ,

$$w = w_0 + w_1 \quad (4.3)$$

Utilizing equations (4.1), (4.2), and (4.3) strains in the m^{th} layer can be written as follows:

$$\epsilon_{x \pm m} = \frac{\partial u_{\pm m}}{\partial x} = (z \pm h_m)(\psi'_m - \theta'_m) \pm \sum_{i=1}^{m-1} (h_{i+1} - h_i)(\psi'_i - \theta'_i) \quad (4.4)$$

$$\gamma_{xz \pm m} = \frac{\partial u_{\pm m}}{\partial z} + \frac{\partial w_1}{\partial x} = \psi_m - \theta_m + w'_1 \quad (4.5)$$

$$\epsilon_{y \pm m} = \epsilon_{z \pm m} = \gamma_{yz \pm m} = \gamma_{xy \pm m} = 0 \quad (4.6)$$

Assuming that each layer is at least piecewise linearly elastic, (which may restrict the analysis to problems with monotonically increasing loads), the stress components can be written in terms of the strains.

$$\sigma_{x \pm m} = E_m \epsilon_{x \pm m} \quad (4.7)$$

$$\tau_{xz \pm m} = G_m \gamma_{xz \pm m}$$

$$\sigma_{y \pm m} = \sigma_{z \pm m} = \tau_{yz \pm m} = \tau_{xy \pm m} = 0$$

The last of equations (4.7) does not satisfy the boundary conditions when a transverse loading is imposed on the laminated beam ($\sigma_z \neq 0$). However, this will be ignored as is customarily done in plate and beam

analyses since σ_z is usually small compared to other stresses in the laminate. Thus, all stress components except $\sigma_{x\pm m}$ and $\tau_{xz\pm m}$ are assumed to vanish. Hence the subscripts will be deleted and

$$\sigma_{x\pm m} = \sigma_{\pm m} \qquad \tau_{xz\pm m} = \tau_{\pm m}$$

will be used. In equations (4.7) G_m and E_m denote shear modulus and Young's modulus, respectively, for the m^{th} layer.

Again it is noted that compression or extension of the beam due to application of axial end loads and the corresponding axial strains and stresses have been neglected. Thus $\sigma_{\pm m}$ represents only longitudinal bending stress and does not include the applied axial stress. In the event total stresses or strains are required, they can readily be obtained using the principle of superposition.

B. Bending Moments, Normal and Shear Forces

Next, expressions for the bending moment, normal, and shear forces on each layer are required. The bending moment due to longitudinal stresses in the m^{th} layer about the midplane of the beam is given by

$$M_{\pm m} = b \int_{h_m}^{h_{m+1}} z \sigma_{\pm m} dz \qquad (4.8)$$

Substituting equations (4.7) and (4.4) into (4.8), and performing the integration leads to

$$M_{\pm m} = E_m (I_m - F_m h_m) (\psi'_m - \theta'_m) \pm E_m F_m \sum_{i=1}^{m-1} (h_{i+1} - h_i) (\psi'_i - \theta'_i) \qquad (4.9)$$

where I_m and F_m are defined by

$$I_m = \frac{b}{3} (h_{m+1}^3 - h_m^3) \quad (4.10)$$

$$F_m = \frac{b}{2} (h_{m+1}^2 - h_m^2)$$

The normal stress resultant due to the longitudinal bending stresses is defined by

$$N_{\pm m} = b \int_{h_m}^{h_{m+1}} \sigma_{\pm m} dz \quad (4.11)$$

which becomes

$$N_{\pm m} = E_m (F_m - A_m h_m) (\psi'_m - \theta'_m) + E_m A_m \sum_{i=1}^{m-1} (h_{i+1} - h_i) (\psi'_i - \theta'_i) \quad (4.12)$$

when stress and strain are expressed in terms of displacements and A_m denotes the cross sectional area of the m^{th} layer. Due to symmetry

$$M_{+m} = M_{-m} \quad (4.13)$$

$$N_{+m} = -N_{-m}$$

The resultant shear force on the m^{th} layer may be expressed by

$$Q_{\pm m} = bk' \int_{h_m}^{h_{m+1}} \tau_{\pm m} dz \quad (4.14)$$

Writing stress in terms of displacements and then integrating equation

(4.14) yields

$$Q_{im} = k' G_m A_m (\psi_m - \theta_m + w_1') \quad (4.15)$$

k' is a shear correction factor. In the past, there has been considerable disagreement as to the precise value of k' , see for example references 58, 59, and 60. In general, the value is close to unity and, following the precedent of Heller and Swift (56), $k' = 1$ will be used herein.

C. Equilibrium Equations

Equilibrium of a segment of the multilayered beam is considered next. Figure 4.3 shows the forces and bending moments acting on the beam segment. As a result of defining bending moments, M_{im} , by equation (4.8), different free body diagrams are used for summing moments and forces on the beam element. The standard practice of replacing the axial applied loads, P_i , by a single load equal to the sum of the applied loads and acting along the midplane of the beam has been utilized. Boundary conditions at the layer interfaces require that the interlaminar shear and normal stresses be equal

$$\begin{aligned} \tau_{m,m} &= \tau_{m,m+1} \\ \sigma_{m,m} &= \sigma_{m,m+1} \end{aligned} \quad (4.16)$$

where the first subscript denotes the interlaminar region at the top of the m^{th} layer and the second subscript denotes the layer on which the stress is acting.

First consider equilibrium of the complete beam segment and sum forces in the horizontal direction:

$$\begin{aligned}
 P \cos w' - (P + dP) \cos(w' + w'dx) + Q \sin \bar{\psi} - (Q + dQ) \sin(\bar{\psi} + \bar{\psi}'dx) \\
 + b(\tau_{n,n} - \tau_{-n,-n}) \cos w'dx - b(\sigma_{n,n} - \sigma_{-n,-n}) \sin w'dx = 0
 \end{aligned}
 \tag{4.17}$$

where $\bar{\psi}$ is defined by

$$\bar{\psi} = \frac{\sum_{i=1}^n Q_i \psi_i}{\sum_{i=1}^n Q_i}
 \tag{4.18}$$

Collecting terms in equation (4.17), expressing the sine and cosine in terms of the small angles w' and $\bar{\psi}$, and dividing by the length of the beam segment, dx , leads to

$$\frac{dP}{dx} + \frac{dQ}{dx} (\bar{\psi} + \bar{\psi}'dx) + Q\bar{\psi}' + b(\tau_{n,n} - \tau_{-n,-n}) - b(\sigma_{n,n} - \sigma_{-n,-n})w' = 0
 \tag{4.19}$$

For case A, $\tau_{n,n}$ and $\tau_{-n,-n}$ vanish and for case B they are equal. Thus the fourth term in equation (4.19) vanishes. The transverse normal stresses, $\sigma_{n,n}$ and $\sigma_{-n,-n}$, are assumed to be small compared to other stresses in the beam. Since they are multiplied by w' , which is small compared to unity, the last term in equation (4.19) is neglected. Since $\bar{\psi} \ll 1$, the shear resultant Q can be considered to act perpendicular to the midplane of the beam and from elementary beam analysis one can readily deduce that

41

$$Q = Pw' \quad (4.20)$$

for the two cases discussed herein. Substituting equation (4.20) into (4.19) leads to

$$\frac{dP}{dx} [1 + w'(\bar{\psi} + \bar{\psi}'dx)] + Pw'(\bar{\psi} + \bar{\psi}'dx) + Pw'\bar{\psi}' = 0 \quad (4.21)$$

Noting that both $\bar{\psi}$ and w' are very small compared to unity, equation (4.21) reduces to

$$\frac{dP}{dx} = 0 \quad (4.22)$$

which agrees with classical plate and beam analyses (see for example reference 2). Equation (4.22) will be used in the subsequent derivations by considering P to be constant along the length of the beam.

In order for the segment to be in equilibrium, the sum of the forces on the outer layers above and below the midplane must also vanish. From figure 4.3, it follows:

$$\begin{aligned} \sum_{i=m+1}^n F_x = 0 = & b(\tau_{n,n} - \tau_{m,m+1}) \cos w'dx + \sum_{i=m+1}^n (N_i + dN_i) \cos (w' \\ & + w'dx) - \sum_{i=m+1}^n N_i \cos w' + \sum_{i=m+1}^n Q_i \sin \psi_i \\ & - \sum_{i=m+1}^n (Q_i + dQ_i) \sin (\psi_i + \psi_i'dx) - b(\sigma_{n,n} - \sigma_{m,m+1}) \sin w'dx = 0 \end{aligned} \quad (4.23)$$

$$\begin{aligned}
\sum_{i=-n}^{-(m+1)} F_x = 0 &= b(\tau_{-m,m+1} - \tau_{n,n}) \cos w' dx + \sum_{i=-n}^{-(m+1)} N_i \cos w' \\
&- \sum_{i=-n}^{-(m+1)} (N_i + dN_i) \cos(w' + w'' dx) + \sum_{i=-n}^{-(m+1)} Q_i \sin \psi_i \\
&- \sum_{i=-n}^{-(m+1)} (Q_i + dQ_i) \sin(\psi_i + \psi_i' dx) + b(\sigma_{-n,-n} \\
&- \sigma_{-m,-(m+1)}) \sin w' dx = 0 \tag{4.24}
\end{aligned}$$

Noting that

$$\begin{aligned}
\cos w' &\approx 1 \\
\cos(w' + w'' dx) &\approx 1 \\
\sin \psi_i &\approx \psi_i' \\
\sin(\psi_i + \psi_i' dx) &\approx \psi_i' + \psi_i'' dx
\end{aligned} \tag{4.25}$$

Collecting terms and dividing through by dx, equations (4.23) and (4.24) reduce to

$$\begin{aligned}
b(\tau_{n,n} - \tau_{m,m+1}) + \sum_{i=m+1}^n N_i' - \sum_{i=m+1}^n (Q_i \psi_i' + Q_i' \psi_i + dQ_i \psi_i') \\
- b(\sigma_{n,n} - \sigma_{m,m+1}) w' = 0 \tag{4.26} \\
b(\tau_{-m,-(m+1)} - \tau_{-n,-n}) - \sum_{i=-n}^{-(m+1)} N_i' - \sum_{i=-n}^{-(m+1)} (Q_i \psi_i' + Q_i' \psi_i + dQ_i \psi_i') \\
+ b(\sigma_{-n,-n} - \sigma_{-m,-(m+1)}) w' = 0 \tag{4.27}
\end{aligned}$$

Substituting equation (4.16) into (4.26) and (4.27) and then subtracting (4.27) from (4.26) leads to

$$b(\tau_{n,n} + \tau_{-n,-n}) - b(\tau_{m,m+1} + \tau_{-m,-(m+1)}) + 2 \sum_{i=m+1}^n N'_i - b[(\sigma_{n,n} + \sigma_{-n,-n}) - (\sigma_{m,m+1} + \sigma_{-m,-(m+1)})] w' = 0 \quad (4.28)$$

Since transverse normal stresses are assumed to be negligible compared to other stresses in equation (4.28) and the last term is multiplied by w' , the last term in the equation is neglected. Thus yielding

$$b(\tau_{n,n} + \tau_{-n,-n}) - b(\tau_{m,m+1} + \tau_{-m,-(m+1)}) + 2 \sum_{i=m+1}^n N'_i = 0 \quad (4.29)$$

Introducing

$$P_x = b(\tau_{n,n} + \tau_{-n,-n}) \quad (4.30)$$

to denote the total applied horizontal shear force per unit length of beam and combining equations (4.29), (4.30) and (4.16) yields

$$\tau_{m,m} + \tau_{-m,-m} = \frac{1}{b} (P_x + 2 \sum_{i=m+1}^n N'_i) \quad (4.31)$$

for expressing the interlaminar shear stresses acting on the $2m$ inner layers of the beam.

In order for the beam segment to be in equilibrium, the sum of the moments acting on the $2m$ inner layers must also vanish. Referring to

figure 4.3, summing moments about the right end of the beam segment leads

to

$$\begin{aligned} \Sigma M = 2 \sum_{i=1}^m (M_i + dM_i - M_i) - 2 \sum_{i=1}^m Q_i \cos \psi_i dx + bh_{m+1} (\tau_{m,m} + \tau_{-m,-m}) dx \\ + P\delta = 0 \end{aligned} \quad (4.32)$$

where δ is defined in figure 4.4 and can be represented by

$$\delta = w(x) + w'(x) dx - w(x + dx) \quad (4.33)$$

Utilizing a Taylor series expansion for $w(x + dx)$ in terms of $w(x)$ and its derivatives, equation (4.33) takes the form

$$\delta = -w''(dx)^2/2 \quad (4.34)$$

when higher order terms are neglected. Substituting equation (4.34) into (4.32), dividing by dx , and noting that $\cos \psi_i \approx 1$ yields

$$2 \sum_{i=1}^m (M_i' - Q_i) + bh_{m+1} (\tau_{m,m} + \tau_{-m,-m}) - Pw''dx/2 = 0 \quad (4.35)$$

The last term in equation (4.35) is a higher order term than the remaining terms. Thus equation (4.35) becomes

$$2 \sum_{i=1}^m (M_i' - Q_i) + bh_{m+1} (\tau_{m,m} + \tau_{-m,-m}) = 0 \quad (4.36)$$

Combining equations (4.36) and (4.31) leads to

$$\sum_{i=1}^m (M_i' - Q_i) + h_{m+1} (P_x + 2 \sum_{i=m+1}^n N_i') = 0 \quad (4.37)$$

Finally, equilibrium in the vertical direction requires that the sum of the forces in the vertical direction vanish. Referring to figure 4.3, it follows:

$$\begin{aligned}
 & 2 \sum_{i=1}^n [(Q_i + dQ_i) \cos(\psi_i + \psi_i' d\psi) - Q_i \cos \psi_i] + P \sin w' \\
 & - P \sin (w' + w' dx) + b(\sigma_{n,n} - \sigma_{-n,-n}) \cos w' dx \\
 & + b(\tau_{n,n} - \tau_{-n,-n}) \sin w' dx = 0
 \end{aligned} \tag{4.38}$$

Noting that equations (4.25) are valid if ψ_i and w' are interchanged, collecting terms and dividing by dx equation (4.38) becomes

$$2 \sum_{i=1}^n Q_i' - Pw'' + b(\sigma_{n,n} - \sigma_{-n,-n}) + b(\tau_{n,n} - \tau_{-n,-n}) w' = 0 \tag{4.39}$$

Denoting the applied transverse load by

$$P_z = b(\sigma_{n,n} - \sigma_{-n,-n}) \tag{4.40}$$

and noting that the last term in equation (4.39) is a higher order term compared to the remaining terms in the equation leads to

$$2 \sum_{i=1}^n Q_i' - Pw'' + P_z = 0 \tag{4.41}$$

Substituting equations (4.9), (4.12), and (4.15) into (4.37) and (4.15) into (4.41) provides a $(n + 1)$ set of linear, second order partial

differential equations.

$$\begin{aligned} & \sum_{i=1}^m [E_i(I_i - F_i h_i)(\psi_i'' - \theta_i'') + E_i F_i \sum_{k=1}^{i-1} (h_{k+1} - h_k)(\psi_k'' - \theta_k'')] \\ & - \sum_{i=1}^m k'_i G_i A_i (\psi_i - \theta_i + w_1') + h_{m+1} P_x / 2 \\ & + h_{m+1} \sum_{i=m+1}^n [E_i(F_i - A_i h_i)(\psi_i'' - \theta_i'') + E_i A_i \sum_{k=1}^{i-1} (h_{k+1} \\ & - h_k)(\psi_k'' - \theta_k'')] = 0 \end{aligned} \quad (4.42)$$

$$\sum_{i=1}^n k'_i G_i A_i w_1'' + \sum_{i=1}^n k'_i G_i A_i (\psi_i' - \theta_i') + P_z / 2 - P w'' = 0 \quad (4.43)$$

Equations (4.42) and (4.43) are the governing differential equations for the problem under consideration. Solving these equations, taking into account the appropriate boundary and initial conditions, permits one to compute the stress-displacement field for the laminate. Equations (4.42) and (4.43) differ from equations (26) and (27) in reference (54) in that P , θ_i , and w_0 were not included in the earlier derivation.

D. Shear Stresses

Noting that $\tau_{m,m}$ and $\tau_{-m,-m}$ and expressing the moments M_i , and shears Q_i , in terms of displacements and substituting into equation (4.36), the following equation is obtained and may be used to compute the interlaminar shear stresses.

$$\tau_{m,m} = \frac{1}{bh_{m+1}} \left\{ \sum_{i=1}^m [E_i(I_i - F_i h_i)(\psi_i'' - \theta_i'') + E_i F_i \sum_{k=1}^{i-1} (h_{k+1} - h_k)(\psi_k'' - \theta_k'')] - \sum_{i=1}^m [k' G_i A_i (\psi_i - \theta_i + v_i')] \right\} \quad (4.44)$$

Shear stresses within the m^{th} layer are readily derived by considering equilibrium of the element shown in figure 4.5.

$$\tau_m = \tau_{m,m} + \int_z^{h_{m+1}} \frac{\partial \sigma_m}{\partial x} dz \quad (4.45)$$

It is noted that the axial compressive stress resulting from the applied load is not shown in figure 4.5 since it was shown earlier (see equation 4.22) that the axial force is constant along the length of the beam.

Thus the terms would cancel and have no effect on equation (4.45).

Expressing σ_m in equation (4.45) in terms of the displacements and then performing the integration yields

$$\tau_m = \tau_{m,m} + E_m \left\{ \left(\frac{h_{m+1}^2}{2} - \frac{z^2}{2} + h_m h_{m+1} + h_m z \right) (\psi_m'' - \theta_m'') + (h_{m+1} - z) \sum_{i=1}^{m-1} (h_{i+1} - h_i)(\psi_i'' - \theta_i'') \right\} \quad (4.46)$$

continuing one step further, the average shear stress within the m^{th} layer is given by

$$\tau_{\text{ave}} = \frac{1}{h_{m+1} - h_m} \int_{h_m}^{h_{m+1}} \tau_m dz \quad (4.47)$$

or in terms of the displacements and interlaminar shear stresses

$$\begin{aligned} \tau_{ave} = \tau_{z,m} + \frac{E_m}{3} (h_{m+1} - h_m)^2 (\psi_m'' - \theta_m'') \\ + \frac{E_m}{2} (h_{m+1} - h_m) \sum_{i=1}^{m-1} (h_{i+1} - h_i) (\psi_i'' - \theta_i'') \end{aligned} \quad (4.48)$$

E. Solution of Governing Equations

A brief examination of equations (4.42) and (4.43) leads to the conclusion that the chances of obtaining a tractable closed form solution for a multilayered beam, particularly if the number of layers is large, are rather remote. One approach for overcoming this obstacle is to express the derivatives of ψ , θ , and w in terms of finite differences. The result is a $(n + 1)$ set of algebraic equations for each node along the beam. For a beam with both ends fixed and subdivided into J intervals, the simultaneous solution of $(J - 1)(n + 1)$ algebraic equations is required to determine the stress and displacement fields. The only practical method of solution is utilization of a computer. Transformation of the governing differential equations into algebraic equations and discussion of the analytical method and computer program used to obtain a solution follow.

Defining

$$\phi_i = \psi_i - \theta_i \quad (4.49)$$

and writing the first and second derivatives at the p^{th} node along the beam in terms of finite differences

$$\phi_1'(p) = \frac{\phi_1(p+1) - \phi_1(p-1)}{2(\Delta x)}$$

$$\phi_1''(p) = \frac{\phi_1(p+1) - 2\phi_1(p) + \phi_1(p-1)}{(\Delta x)^2}$$

equations (4.42) and (4.43) may be expressed in the following matrix form.

$$\begin{bmatrix} R_{11} & R_{12} & \dots & R_{1s} & | & S_{11} & S_{12} & \dots & S_{1s} & | & T_{11} & T_{12} & \dots & T_{1s} \\ R_{21} & R_{22} & \dots & R_{2s} & | & S_{21} & S_{22} & \dots & S_{2s} & | & T_{21} & T_{22} & \dots & T_{2s} \\ \cdot & \cdot & \cdot & \cdot & | & \cdot & \cdot & \cdot & \cdot & | & \cdot & \cdot & \cdot & \cdot \\ \cdot & \cdot & \cdot & \cdot & | & \cdot & \cdot & \cdot & \cdot & | & \cdot & \cdot & \cdot & \cdot \\ R_{s1} & R_{s2} & \dots & R_{ss} & | & S_{s1} & S_{s2} & \dots & S_{ss} & | & T_{s1} & T_{s2} & \dots & T_{ss} \end{bmatrix} \begin{bmatrix} \phi_1(p-1) \\ \phi_n(p-1) \\ w(p-1) \\ \phi_1(p) \\ \phi_n(p) \\ w(p) \\ \phi_1(p+1) \\ \phi_n(p+1) \\ w(p+1) \end{bmatrix} = \begin{bmatrix} P_1(p) \\ P_2(p) \\ \cdot \\ \cdot \\ P_s(p) \end{bmatrix} \quad (4.51)$$

where $s = (n + 1)$. Utilizing abbreviated notation equation (4.51) becomes

$$\begin{bmatrix} \underline{R} & | & \underline{S} & | & \underline{T} \\ \hline -p & | & -p & | & -p \end{bmatrix} \begin{bmatrix} \underline{Y}_{p-1} \\ \underline{Y}_p \\ \underline{Y}_{p+1} \end{bmatrix} = \begin{bmatrix} \underline{P}_p \end{bmatrix} \quad (4.52)$$

Coefficients of the \underline{R} , \underline{S} , \underline{T} , matrices and the load vector \underline{P} are defined as follows:

$$i = j \leq n$$

$$R_{ij} = \frac{2E_i(I_i - F_i h_i) + 2h_{i+1}(h_{i+1} - h_i) \sum_{k=i+1}^n E_k A_k}{(\Delta x)^2} \quad (4.53a)$$

$$i > j \leq n$$

$$R_{ij} = \frac{2E_j(I_j - F_j h_j) + 2(h_{j+1} - h_j) \sum_{k=j+1}^i E_k F_k + 2h_{i+1}(h_{j+1} - h_j) \sum_{k=i+1}^n E_k A_k}{(\Delta x)^2} \quad (4.53b)$$

$$i < j \leq n$$

$$R_{ij} = \frac{2h_{i+1} E_j (F_j - A_j h_j) + 2h_{i+1}(h_{j+1} - h_j) \sum_{k=j+1}^n E_k A_k}{(\Delta x)^2} \quad (4.53c)$$

$$1 \leq i \leq n$$

$$j = s$$

$$R_{ij} = \sum_{k=1}^i k' G_k A_k / \Delta x \quad (4.53d)$$

$$i = s$$

$$1 \leq j \leq n$$

$$R_{ij} = -k' G_j A_j / \Delta x \quad (4.53e)$$

$$i = s$$

$$j = s$$

$$R_{ij} = \frac{2 \sum_{k=1}^n k' G_k A_k - P}{(\Delta x)^2} \quad (4.53f)$$

$$1 \leq i \leq n$$

$$j \leq i$$

$$S_{ij} = -2(R_{ij} - k'G_j A_j) \quad (4.54a)$$

$$1 \leq i \leq n$$

$$j > i$$

$$S_{ij} = -2 R_{ij} \quad (4.54b)$$

$$1 \leq i \leq n$$

$$i = s$$

$$S_{ij} = 0 \quad (4.54c)$$

$$i = s$$

$$1 \leq j \leq n$$

$$S_{ij} = 0 \quad (4.54d)$$

$$i = s$$

$$j = s$$

$$S_{ij} = -2 R_{ij} \quad (4.54e)$$

$$1 \leq i \leq n$$

$$1 \leq j < n$$

$$T_{ij} = R_{ij} \quad (4.55a)$$

$$1 \leq i \leq n$$

$$j = s$$

$$T_{ij} = -R_{ij} \quad (4.55b)$$

$$i = s$$

$$1 \leq j \leq n$$

$$T_{ij} = -R_{ij} \quad (4.55c)$$

$$i = s$$

$$j = s$$

$$T_{ij} = R_{ij} \quad (4.55d)$$

$$1 \leq i \leq n$$

$$P_i(p) = -h_{i+1} P_x \quad (4.56a)$$

$$i = s$$

$$P_i(p) = -P_z + P w_0^n \quad (4.56b)$$

Inspection of equation (4.53f) indicates that the values of some coefficients are a function of the applied axial load, P . As a result, stresses and displacements due to large loads may have to be computed in smaller increments in order to avoid error in the analysis. The influence of load increment size will be discussed later.

Applying equations (4.52) to each node along the beam

leads to the following set of matrix equations.

$$\begin{bmatrix} R_2 & S_2 & T_2 & 0 & 0 & 0 & \cdot & \cdot & \cdot & \cdot \\ 0 & R_3 & S_3 & T_3 & 0 & 0 & \cdot & \cdot & \cdot & \cdot \\ 0 & 0 & R_4 & S_4 & T_4 & 0 & \cdot & \cdot & \cdot & \cdot \\ \cdot & \cdot & \cdot & 0 & 0 & 0 & R_{J-1} & S_{J-1} & T_{J-1} & 0 \\ \cdot & \cdot & \cdot & 0 & 0 & 0 & 0 & R_J & S_J & T_J \end{bmatrix} \begin{bmatrix} Y_1 \\ Y_2 \\ \cdot \\ \cdot \\ Y_J \\ Y_{J+1} \end{bmatrix} = \begin{bmatrix} P_2 \\ P_3 \\ \cdot \\ \cdot \\ P_{J-1} \\ P_J \end{bmatrix} \quad (4.57)$$

When boundary conditions are taken into account, rotations and deflections at the end of the beam (Y_1 and Y_{J+1}) are prescribed for the cases under consideration and equation (4.57) becomes

$$\begin{bmatrix} S_2 & T_2 & 0 & 0 & 0 & \cdot & \cdot & \cdot \\ R_3 & S_3 & T_3 & 0 & 0 & \cdot & \cdot & \cdot \\ 0 & R_4 & S_4 & T_4 & 0 & \cdot & \cdot & \cdot \\ \cdot & \cdot & \cdot & 0 & 0 & R_{J-1} & S_{J-1} & T_{J-1} \\ \cdot & \cdot & \cdot & 0 & 0 & 0 & R_J & S_J \end{bmatrix} \begin{bmatrix} Y_2 \\ Y_3 \\ \cdot \\ \cdot \\ Y_{J-1} \\ Y_J \end{bmatrix} = \begin{bmatrix} P_2 \\ P_3 \\ \cdot \\ \cdot \\ P_{J-1} \\ P_J \end{bmatrix} \quad (4.58)$$

Equations (4.58) may be solved by utilizing the tridiagonal method of solution described in reference 61 and used earlier by Swift (57). The method of solution works in the following manner. Starting with the first of equations (4.58) and proceeding to the last, the values of Y_1 are expressed in terms of Y_{i+1} .

$$\begin{aligned}
\underline{Y}_2 &= \underline{S}_2^{-1} [\underline{P}_2 - \underline{T}_2 \underline{Y}_3] \\
\underline{Y}_3 &= [\underline{S}_3 - \underline{R}_3 \underline{S}_2^{-1} \underline{T}_2]^{-1} [\underline{P}_3 - \underline{R}_3 \underline{S}_2^{-1} \underline{P}_2 - \underline{T}_3 \underline{Y}_4] \\
\underline{Y}_4 &= [\underline{S}_4 - \underline{R}_4 [\underline{S}_3 - \underline{R}_3 \underline{S}_2^{-1} \underline{T}_2]^{-1} \underline{T}_3]^{-1} [\underline{P}_4 - \underline{R}_4 [\underline{S}_3 - \underline{R}_3 \underline{S}_2^{-1} \underline{T}_2]^{-1} [\underline{P}_3 \\
&\quad - \underline{R}_3 \underline{S}_2^{-1} \underline{P}_2] - \underline{T}_4 \underline{Y}_5 \\
&\vdots
\end{aligned} \tag{4.59}$$

Noting the following recurrence formulas,

$$\underline{H}_i = \underline{S}_i - \underline{R}_i \underline{H}_{i-1}^{-1} \underline{T}_{i-1} \tag{4.60}$$

$$\underline{Q}_i = \underline{R}_{i+1} \underline{H}_{i+1}^{-1} [\underline{P}_i - \underline{Q}_{i-1}] \tag{4.61}$$

and substituting into equations (4.59) leads to

$$\begin{aligned}
\underline{Y}_2 &= \underline{H}_2^{-1} [\underline{P}_2 - \underline{T}_2 \underline{Y}_3] \\
\underline{Y}_3 &= \underline{H}_3^{-1} [\underline{P}_3 - \underline{Q}_2 - \underline{T}_3 \underline{Y}_4] \\
&\vdots \\
\underline{Y}_{j-1} &= \underline{H}_{j-1}^{-1} [\underline{P}_{j-1} - \underline{Q}_{j-2} - \underline{T}_{j-1} \underline{Y}_j] \\
\underline{Y}_j &= \underline{H}_j^{-1} [\underline{P}_j - \underline{Q}_{j-1}]
\end{aligned} \tag{4.62}$$

Values of displacement and rotation (\underline{Y}_j) at the j^{th} node can be calculated using the last of equations (4.62). Then the remaining values of \underline{Y}_i can be calculated by successive back substitution.

The computer program, written earlier by Swift (57), was modified

to solve equations (4.58). In addition to making changes required to appropriately adjust the coefficient matrices (\underline{R} , \underline{S} , \underline{T}), the program was altered to accept materials which exhibit nonlinear shear stress-strain behavior. A brief description of the computer program is given in Appendix A.

F. Initial and Boundary Conditions

Figure 4.1 shows sketches of the two problems studied. As indicated previously, case A represents an entire laminate and case B represents a typical repeating element contained in a laminate. For each case, an initial deflection of the form

$$w_0 = a_0 \{1 + \sin[(2\pi/L)(x - L/4)]\} \quad (4.63)$$

$$\theta_1 = 0$$

was assumed. The transverse deflection, w_0 , is symmetric about the midspan of the beam and has zero slope at the midspan and both ends of the beam. Values of w_0'' are evaluated at each node along the beam and used to compute the values of $P_1(p)$ in equation (4.56b). The choice of θ_1 is based on the requirement that all layers have the same initial radius of curvature and that displacements in the x direction are continuous at the layer interfaces. In other words, prior to assembly of the laminate, each layer was assumed to undergo the transverse deflection represented by equation (4.63) and then all cross sections which were initially perpendicular to the neutral axis were rotated

back to the vertical position in order to impose continuity of the horizontal displacements. For both cases, the ends of the laminate were assumed to be fixed and thereby preventing any lateral deflection or rotation at the stations $x = 0$ and $x = L$. For case A, the upper and lower surfaces were assumed to be free of tractions. For case B, the upper and lower surfaces form the boundary of a repeating element and in order to satisfy compatibility horizontal displacement, $u(x)$, was not permitted along these boundaries. An unknown surface traction, $\tau_{n,n}$ results from this constraint.

Thus for case B, an additional equation and an additional unknown $\tau_{n,n}$ must be included in the analysis. The requirement that $u(x)$ vanish along the upper and lower surfaces provides the additional equation

$$\phi_1 h_2 + \phi_3 (h_3 - h_2) + \dots + \phi_n (h_{n+1} - h_n) = 0 \quad (4.65)$$

Referring to equation (4.20) and noting the relationship between $\tau_{n,n}$ and P_x , permits P_x to be treated as the unknown variable and equations (4.51) take the form

$$\begin{array}{c}
 \left[\begin{array}{cccc|cccc|cccc}
 R_{11} & R_{12} & \dots & R_{1s} & 0 & S_{11} & S_{12} & \dots & S_{1s} & h_2/2 & T_{11} & T_{12} & \dots & T_{1s} & 0 \\
 R_{21} & R_{22} & \dots & R_{2s} & 0 & S_{21} & S_{22} & \dots & S_{2s} & h_3/3 & T_{21} & T_{22} & \dots & T_{2s} & 0 \\
 \cdot & \cdot & \cdot & \cdot & \cdot & \cdot & \cdot & \cdot & \cdot & \cdot & \cdot & \cdot & \cdot & \cdot & \cdot \\
 \cdot & \cdot & \cdot & \cdot & \cdot & \cdot & \cdot & \cdot & \cdot & \cdot & \cdot & \cdot & \cdot & \cdot & \cdot \\
 R_{n1} & R_{n2} & \dots & R_{ns} & 0 & S_{n1} & S_{n2} & \dots & S_{ns} & h_{n+1}/2 & T_{n1} & T_{n2} & \dots & T_{ns} & 0 \\
 R_{s1} & R_{s2} & \dots & R_{ss} & 0 & S_{s1} & S_{s2} & \dots & S_{ss} & 0 & T_{s1} & T_{s2} & \dots & T_{ss} & 0 \\
 0 & 0 & \dots & 0 & 0 & h_2 & (h_3-h_2) & \dots & (h_{n+1}-h_n) & 0 & 0 & 0 & \dots & 0 & 0
 \end{array} \right]
 \begin{array}{c}
 \phi_1^{(p-1)} \\
 \phi_n^{(p-1)} \\
 w^{(p-1)} \\
 P_x^{(p-1)} \\
 \phi_1^{(p)} \\
 \cdot \\
 \cdot \\
 \phi_n^{(p)} \\
 w^{(p)} \\
 P_x^{(p)} \\
 \phi_1^{(p+1)} \\
 \phi_n^{(p+1)} \\
 w^{(p+1)} \\
 P_x^{(p+1)}
 \end{array}
 =
 \begin{array}{c}
 P_1^{(p)} \\
 P_2^{(p)} \\
 \cdot \\
 P_n^{(p)} \\
 0
 \end{array}
 \end{array}
 \quad (4.66)$$

Equations (4.66) were solved using the procedure described for obtaining a solution to equations (4.51).

V. SHEAR INSTABILITY OF MULTILAYERED MEDIA

Figure 5.1 shows a segment of a multilayered medium under axial compression load. The medium is assumed to be composed of repeating elements which might be representative of a lamina or fiber reinforced composite material. The length to width ratio of each lamina in the multilayered material is assumed to be small and thus bending (Euler buckling) of the laminae is precluded. The magnitude of the applied end loads is such that a uniform axial strain is imposed on the material. The repeating element is assumed to be symmetric about its midplane and compatibility of displacements along the vertical boundaries is imposed in the following analysis. As a result, the average vertical displacement at the upper ends of the $+n^{\text{th}}$ and $-n^{\text{th}}$ laminae will equal the displacement at the midplane of the repeating element. Thus, for convenience, the applied axial loads are replaced by a single load acting at the midplane of the repeating element.

The axial load which initiates shear buckling, may be calculated using an energy analysis, as indicated in reference 15. Referring to figure 5.1, it is noted that the work done by the external forces in going from the initial position to the buckled position is

$$W = P\delta \quad (5.1)$$

where δ is the axial displacement of the midplane and the outer surfaces of the repeating element. δ can be expressed in terms of the slope,

w_1' , by

$$\delta = (1 - \cos w_1') dx \quad (5.2)$$

and utilizing the relationship

$$\cos w_1' \approx 1 - w_1'^2/2 \quad (5.3)$$

equation (5.1) becomes

$$W = P w_1'^2 dx/2 \quad (5.4)$$

Since bending of the laminae is precluded, the change in strain energy in going from the initial position to the buckled position is due only to shearing stresses and is given by

$$U = \sum_{i=1}^n \tau_i \gamma_i A_i dx \quad (5.5)$$

where τ_i , γ_i , and A_i denote shear stress, shear strain and cross sectional area of the i^{th} layer. Expressing shear stress and shear strain in terms of displacement, w_1 , and rotations ϕ_1 (refer to equations (4.5) and (4.7)) and substituting into equation (5.5) yields

$$U = \sum_{i=1}^n G_i A_i (\phi_i + w_1')^2 dx \quad (5.6)$$

Equating W and U leads to

$$P w_1'^2 = 2 \sum_{i=1}^n G_i A_i (\phi_i + w_1')^2 \quad (5.7)$$

Equation (5.7) plus the following equation which imposes continuity of displacements along the vertical edges of the repeating element, are the governing equations for predicting shear instability.

$$\sum_{i=1}^n A_i \phi_i = 0 \quad (5.8)$$

Next, determining the minimum value of P using the method of Lagrange multipliers

$$\frac{\partial P}{\partial w'_1} + \lambda \frac{\partial \phi}{\partial w'_1} = 0 \quad (5.9)$$

$$\frac{\partial P}{\partial \phi_1} + \lambda \frac{\partial \phi}{\partial \phi_1} = 0$$

⋮

$$\frac{\partial P}{\partial \phi_n} + \lambda \frac{\partial \phi}{\partial \phi_n} = 0 \quad (5.10)$$

where ϕ represents the constraint equation (5.8). Substituting equations (5.7) and (5.8) into (5.9) and (5.10) and performing the differentiation leads to

$$\sum_{i=1}^n G_i A_i (\phi_i + w'_1) w'_1 - \sum_{i=1}^n G_i A_i (\phi_i + w'_1)^2 = 0 \quad (5.11)$$

$$4G_1 A_1 (\phi_1 + w'_1) / w'_1{}^2 + \lambda A_1 = 0$$

⋮

(5.12)

$$4G_n A_n (\phi_n + w'_1) / w'_1{}^2 + \lambda A_n = 0$$

Eliminating the Lagrange multiplier from equations (5.12) yields

$$G_1 (\phi_1 + w'_1) = G_2 (\phi_2 + w'_1) = \dots = G_n (\phi_n + w'_1) \quad (5.13)$$

Equation (5.13) indicates that P will be minimum when a state of uniform shear stress exists in the buckled element. The solution, equation (5.13), also satisfies equation (5.11). This can be shown by substituting equations (5.13) and (5.8) into (5.11). Utilizing equations (5.8) and (5.13) to determine the values of ϕ_i in terms of v_1' and then substituting the results into equation (5.7) yields

$$P_{cr} = \frac{2(A_1 + A_2 + \dots + A_n)^2}{\left(\frac{A_1}{G_1} + \frac{A_2}{G_2} + \dots + \frac{A_n}{G_n}\right)} \quad (5.14)$$

Denoting the average compressive stress by

$$\sigma_{cr} = P_{cr} / 2 \sum_{i=1}^n A_i \quad (5.15)$$

and the volume fraction of the i^{th} lamina by

$$V_i = A_i / \sum_{i=1}^n A_i \quad (5.16)$$

and substituting into (5.14) leads to

$$\sigma_{cr} = \frac{G_1 G_2 \dots G_n}{V_1 G_2 \dots G_n + V_2 G_1 G_3 \dots G_n + \dots + V_n G_1 \dots G_{n-1}} \quad (5.17)$$

Equation (5.17) was used to predict shear buckling in the computer program described in Appendix A.

Perhaps it should be noted that the right side of equation (5.17) equals the predicted shear modulus of a multilayered material, based on

the "stiffness in series" model for the material. Thus equation (5.17) agrees with Foye's (15) results for the case, $n = 2$.

VI. EXPERIMENTAL INVESTIGATION

Fabrication procedures and test methods utilized in the research program are described in this section of the thesis. Two types of composite specimens, lamina and fiber reinforced, were fabricated and tested. The lamina reinforced composites were designed to provide verification of the interlaminar shear analysis and the fiber reinforced composite specimens were designed to show a relationship between shear modulus and axial compressive stress.

A. Lamina Reinforced Composites

1. Laminate Fabrication

Four specimens were fabricated using either 0.040-inch or 0.083-inch thick strips of 7075-T6 aluminum for the reinforcement and type "WI-Green Rigidax" compound for the matrix. Figure 6.1 shows two of the specimens. All specimens were nominally one-half inch thick and contained ten reinforcing laminae. At the ends of each specimen aluminum shims were used to maintain a uniform spacing between the reinforcing laminae and to provide the additional stiffness required to simulate a clamped end boundary condition during testing.

The two larger specimens were fabricated using 0.083-inch thick strips of aluminum which had been hand-formed on a 6.0-inch diameter steel cylinder. After the strips were formed, they were assembled with the separating shims and a hole was drilled through each end to permit clamping with a machine screw and fastener. Next, the assembly was

chemically cleaned and then disassembled. The specimen was then reassembled using a pattern of pins (drill bits) to align the reinforcing laminae. (See figure 6.2.) The pins were held in position by an aluminum plate which had been precision machined to provide the pattern. In general, the pins passed through the laminate and extended into the plate approximately 1/8-inch. Minimal effort was required to insert the reinforcing laminae between adjacent rows of pins, since each lamina had been formed to approximately the same shape as the pin pattern. Next the assembly and plate were heated to 250°F in a circulating-air oven and the cavities between the aluminum strips were filled with molten wax. After the specimen was allowed to cool to room temperature, it was removed from the supporting plate. The alignment pins remained in the specimen, as shown in figure 6.3. The pins were not located at points where peak interlaminar shear stresses were expected to occur.

Fabrication of the two smaller specimens was similar with the exception that a rectangular frame and only two transverse rows of pins were used to align the reinforcing laminae which had been hand formed on a 4.5-inch diameter cylinder. Figure 6.3 shows the pins remaining in one of the specimens containing 0.040-inch thick laminae. The ends of each specimen were machined flat and parallel and perpendicular to the length direction of the specimen in order that uniform loading of the ends could be approached.

Table 6.1 lists the dimensions for each specimen. The x and z coordinates listed were determined with a CORDAX measuring machine which

is accurate to within $\pm 1/1000$ inch. Specimen length and width were measured with a machinist scale. Specimen thickness was determined by subtracting the upper and lower z coordinates at each station along the x axis where measurements were taken. A comparison of the initial displacement pattern for each laminate with the displacement given by equation (4.63) is shown in figure 6.4.

2. Matrix Specimens

Cylindrical and tubular shaped specimens were fabricated and used to determine compression and shear stress-strain curves, respectively, for the matrix material. The compression specimen was made by first filling a brass tube with molten wax and then machining off the brass tube after the wax had cooled to room temperature. Nominal dimensions for the compression specimen were 3.0 inches in length and a 1.0 inch diameter. (See figure 6.5.)

A matrix shear test specimen is shown in figure 6.6. The specimen was machined from a 9-inch long by 2-inch square casting of wax. Nominal dimensions for the finished specimen were: 6.000-inch length, 1.750-inch square ends, 2.000-inch long, 1.500-inch outside diameter by 1.000-inch inside diameter test section. The test section to end grip transition portion of the specimen was tapered at an angle of approximately 20 degrees.

3. Matrix-Reinforcement Bond Strength Specimens

Figure 6.7 shows the type of specimen used to determine the bond strength between the aluminum reinforcement and the matrix material.

The specimen consists of two basic parts: a 0.50 inch thick by 2.000 inch square aluminum block with a 15/16 inch diameter hole and a 0.750 inch outside diameter by 0.062 inch thick aluminum tube. The aluminum tube passed through the hole in the block. The tube was located in the center of the hole and thus provided a uniform gap between the two parts. The gap was filled with molten wax.

4. Compressor Test of Laminate Specimens

Figure 6.8 shows the test setup utilized for each laminated specimen. Compressive load was applied to the specimen by the upper and lower platens of a 120,000 pound capacity hydraulic testing machine which had been calibrated to an accuracy of 0.1 percent full scale load with standards traceable to the National Bureau of Standards. Loading rates of 4100 and 2100 pounds per minute were applied to the larger and smaller laminates, respectively. These loading rates correspond approximately to an axial strain rate of 0.001 per minute.

Foil type strain gages were bonded to the edge of aluminum laminae number 3 and 5 at the specimen mid length. (See figure 6.9.) Strain gages were also bounded to the outer surface of aluminum laminae number 1 and 10 at the specimen mid length and one inch either side of the mid length. (See figure 6.10.) No attempt was made to attach strain gages to the matrix laminae since an earlier effort to bond gages to wax castings had proved to be unsuccessful. The resistance of each gage was 120 ohms, ± 0.3 percent. Gages factors ranged from 2.04 to 2.15 for all gages, but the value for each gage was known within ± 0.5 percent. Each gage was connected to a single active arm Wheatstone bridge which

utilized a 3.00 volt power supply. The average circuit sensitivity was 1.58 volts. Recording equipment capable of accurately detecting voltage changes as small as 0.0025 millivolts was used to read voltage changes in the Wheatstone bridge. Thus strain increments as small as 0.000002 in./in. could be detected.

Transverse and axial displacements were measured with linear direct current differential transformers (DCDT). Full range displacement varied from ± 0.050 to ± 1.000 inches. The DCDT's with ± 0.050 -inch displacement range could accurately measure displacements as small as 0.000167-inch whereas the DCDT's with ± 1.000 inch range were only accurate to approximately 0.001 inch.

During the tests, load strain data from the four gages at the mid span of the specimen and load deflection data from four transformers along one side of the specimen were monitored on an oscilloscope at the test site. All data were recorded on magnetic tape in the Langley Research Center data processing facility. In general, the data were recorded at one second intervals.

5. Compression Test of Matrix Specimens

Figure 6.11 shows the test setup utilized to obtain compressive stress-strain data on the wax matrix material. The specimen was positioned in an Instron testing machine and load was applied by lowering the upper platen at a constant rate of 0.01-inch per minute. Load was recorded as a function of time for subsequent use with platen displacement to develop stress-strain plots.

6. Torsion Test of Matrix Specimens

Figure 6.12 shows the test setup utilized to obtain shear stress-strain data on the matrix material. The tests were performed in a 60,000 inch-pound capacity hydraulic testing machine. The right end of the specimen was held stationary and the left end was rotated. Rotation at two stations along the specimen were measured using linear direct current transformers capable of accurately measuring displacements as small as 0.0004-inch. Torque-deflection curves were monitored on an oscilloscope at the test site. Data were recorded at each 5-inch-pounds of load and stored on magnetic tape.

7. Bond Strength Test

Figure 6.13 shows the bond strength test setup. Compressive load was applied to the upper end of the tube. The load was reacted by shearing stress at the tube-wax interface. The tests were performed in an Instron Testing machine and using a constant head displacement rate of 0.002-inch per minute. Load was recorded as a function of time for subsequent use with platen displacement to develop load deflection plots.

B. Fiber Reinforced Composites

1. Fabrication of Tube Specimens

Unidirectionally fiber reinforced tubular specimens for use in compression, torsion and combined compression-torsion tests were fabricated using the general procedure presented in reference 26 with minor modifications. Figure 6.14 shows a flow diagram of the fabrication process and a brief description follows. First, an aluminum tube which

serves as the mandrel is cut to the required length and several small holes are drilled through the wall near each end. Next, a Teflon heat shrinkable sleeve is positioned on the aluminum tube and heated until it fits tightly around the tube. In the second step, plies of preimpregnated filaments are wrapped around the mandrel. The filaments are aligned parallel to the longitudinal axis. Each ply extends one revolution around the mandrel and contains a butt-type seam. Seams in the various layers are uniformly distributed around the circumference. After the required number of plies have been laid up, a release cloth and then bleeder plies are tightly wrapped over the prepreg material. The bleeder plies extend over the holes in the aluminum tube. The fourth step consists of placing a Teflon sleeve over the bleeder plies and heating until it fits tightly. The ends of the sleeve are sealed by clamping. The entire assembly is then placed in an autoclave for curing under pressure at elevated temperature. While in the autoclave, one end of the aluminum tube is plugged and the other is connected to a vacuum line. After the prepreg material has been cured, the composite tube is easily cut into sections and removed from the mandrel.

Three types of composite material were used in the study. The fiber, matrix, and cure cycle for each material are listed in Table 6.2. Ten ply tubes were fabricated using the 4-mil boron-epoxy prepreg and the glass-epoxy prepreg. An 11-ply tube was fabricated from the 5.6-mil boron-epoxy prepreg. One ply of MIL-TEX nylon peel ply number 3921 cloth was used for the release ply on the 4-mil boron epoxy tube. TX-1040, a Teflon coated style 104 glass cloth, was used for the release

ply on the other two tubes. A nylon shrink tape, Bally Ribbon Mills pattern 7282, was used for bleeder plies on all tubes. Two bleeder plies were used on the 10-ply tubes and three bleeder plies were used on the 11-ply tube.

Cross sectional views of each tube are shown in figure 6.15. The two boron filament reinforced tubes were photographed at the same magnification and the difference in size between filaments is apparent. The glass reinforced tube was photographed at a higher magnification in order to show individual filaments. Filament content for the 4-mil boron-epoxy and 5.6-mil boron-epoxy tubes was determined using the point counting technique presented in reference 62. The respective values are 52 and 53 percent. Filament content for the glass tube was determined using the procedure described in reference 63 and the value is 68 percent.

Each tube was cut into several specimens utilizing a diamond cutting wheel. The ends of each specimen were ground flat, square and perpendicular to the longitudinal axis of the specimen. Machined end plugs were bonded with Versamid 140-Epon 828 resin (equal parts by weight) to each specimen. The end plugs were 1.75-inches square, 0.25-inch thick and had a 0.125-inch deep machined groove in which the specimen was inserted. The width of the groove was 0.015-inch greater than the tube wall thickness and the groove diameter was specified such that clearances of 0.005-inch and 0.010-inch were obtained on the inside and outside of the tube, respectively. (See figure 6.16.) Figures 6.17 and 6.18 show boron-epoxy and S-glass epoxy specimens. The longer

specimens were used in torsion and combined compression-torsion tests whereas the shorter specimens were tested in compression.

Table 6.3 lists the dimensions for each fiber reinforced tubular specimen and the type of tests performed on it. Outside-diameter measurements were made with a micrometer whereas wall-thickness measurements were made with a moveable-dial-gage apparatus described in reference 64. Specimen length was measured with a machinist scale. Six diameter measurements were made on each specimen, two at each end and two at the center. The maximum variation in diameter was less than one percent of the value reported in Table 6.3. Twelve wall-thickness measurements were made on each specimen, four at each end and four at the center. The maximum variation in wall thickness was less than 4.5 percent of the value reported in Table 6.3.

2. Compression Test

Figure 6.19 shows the compression test setup. The tests were performed in the same 120,000-pound capacity testing machine used to test the lamina reinforced specimens. Foil-type strain gages were used to measure axial strain at three locations, 90 degrees apart, around the circumference of the specimen. At least one compression specimen from each tube was also instrumented with a 45° degree foil gage rosette which measured strains parallel and ±45° with respect to the longitudinal axis. A constant load rate of approximately 5000 pounds per minute was maintained during all tests.

3. Torsion Test

Figure 6.20 shows the torsion test setup. The same testing machine that was used to test the matrix specimens was used for these tests. The right end of the specimen was held stationary and the left end was rotated by the testing machine. Strain data were obtained from two diametrically opposite rosettes which contained a 0 and 45 degree oriented gage. All tests were conducted at a nominal load rate of 50 inch-pounds per minute.

4. Combined Compression and Torsion Test

Figure 6.21 shows the test setup for the combined compression and torsion test. This apparatus was used to generate torque-strain curves for the composite material while it was under compressive load. While each torque-strain curve was being generated, the compressive load was held constant at a predetermined value. The test specimen was mounted in series with an aluminum load cell which was rigidly attached to the upper platen of the compression testing machine. While not visible in the photograph, the load cell had a tubular cross section and the walls contained four equally spaced longitudinal slits. The slits were used to reduce torsional stiffness so that the magnitude of the applied torque could be detected by rotation of the lower end of the load cell. Rotation was measured by two DCDT's which were capable of detecting displacements as small as 0.000084-inch. Typical calibration runs from 0 to 150-inch-pounds, using 17 discrete load points, indicated 13 points would be within 0.375-inch-pounds of a straight line determined from a least squares fit of the data. The lower end of the specimen was

supported by a thrust bearing assembly. Torque was applied by attaching weights on two strings which were connected to the moment arms.

Diametrically opposite strain rosettes were attached to the middle of the specimen. The rosettes contained aluminum foil-type gages aligned at 0 and ± 45 degrees with respect to the longitudinal axis. A single strain gage was mounted midway between the two rosettes. Torque was increased in increments, either by adding 0.5 or 1.0 pound weights.

Strain gage and load data from the compression, torsion, and combined compression and torsion tests were recorded in the Langley Research Center data processing facility. Recording intervals varied from 0.25 to 5.0 seconds depending on the test circumstances. The higher rate was generally used when failure was expected. Selected data were displayed on oscilloscopes and monitored at the test site.

VII. RESULTS AND DISCUSSION

Both theoretical and experimental results are presented herein. The theoretical results consist of data generated by the computer program described in Appendix B. The experimental results were obtained from tests on laminated beams and fiber reinforced tubular specimens.

A. Theory

The eight layer beam shown in figure 7.1 was used as a model laminate in generating the theoretical results. The beam is symmetrical about its center line, has an initial deflection represented by

$$w_0 = 0.02\{1 + \sin[0.5\pi(x - 1)]\} \quad (7.1)$$

$$\theta_1 = 0 \quad (7.2)$$

and the span to depth ratio equals 4. Six values of reinforcement to matrix stiffness ratio were investigated for both boundary conditions A and B described herein. In addition, the effect of nonlinear shear stress behavior in the matrix and load increment size were studied. Results obtained with case A and case B boundary conditions were compared.

1. Reinforcement/Matrix Stiffness Ratio

Table 7.1 lists rotations, interlaminar shear stresses, and shear resultant at $x = L/4$ and transverse deflection at $x = L/2$ calculated

by the computer program and classical beam theory (CBT) for the beam shown in figure 7.1. For all examples listed in table 7.1, end loads corresponding to a uniform axial strain of 6.4×10^{-4} were prescribed. In order to emphasize transverse shear deflection, shear modulus values for each layer were arbitrarily chosen to be one tenth the value calculated using the assumptions of isotropic material behavior and Poisson's ratio equal to 0.3.

Examination of the results, based on case A boundary conditions, indicates: (1) For high values of the stiffness ratio E_1/E_2 , 10^7 to 10^3 , the reinforcing laminae behave like separate columns and interlaminar shear stresses are negligible except at the neutral axis. (2) As the ratio E_1/E_2 becomes smaller, 10 to 1, the matrix laminae influence the reinforcing laminae behavior and interlaminar shear stresses become more evenly distributed over the beam cross section. (3) The rotations at $x = L/4$ and transverse deflection at $x = L/2$ show the expected trends. To be specific, one would always expect a counter clockwise rotation at $x = L/4$ in the reinforcing laminae. The data substantiates this, even for the case where the matrix and reinforcement laminae positions are interchanged ($E_1/E_2 = 10^{-5}$). Total transverse displacement decreases as E_1/E_2 approaches unity and is always greater than the value calculated with classical beam theory. When comparing the displacements listed in table 7.1, the reader should recall that the initial displacement was 4.00×10^{-2} . Hence the difference between values calculated by the computer program and with CBT are significant.

Examination of the results, based on case B boundary conditions,

indicates: (1) Behavior of the reinforcing laminae is not affected by the matrix laminae, if E_1/E_2 is greater than 10^3 . (2) As the value of E_1/E_2 becomes smaller, range of 10 to 1, the reinforcing laminae are influenced by the matrix and the interlaminar shear stresses become more evenly distributed over the beam cross section. (3) Rotations and transverse deflection indicated the expected trends. Rotation of the reinforcement was in the counter clockwise direction and equal values of rotation in the clockwise direction were computed for the matrix laminae. Transverse displacement decreases as E_1/E_2 approaches unity and always exceeds the value computed with classical beam theory.

2. Shear Stress Distribution

Figure 7.2 shows the variation in shear stress through the depth of the beam predicted by both the computer program and classical beam theory. The plots are based on the beam shown in figure 7.1, boundary conditions A and the fifth set of material properties ($E_1 = E_2 = 10^7$) listed in table 7.1. Both methods indicate that the maximum shear stress is developed at the neutral axis. However, the computer program, predicts a peak shear stress approximately 15 percent below the classical beam theory value. Perhaps even more significant is the difference in the shape of the two curves over the central portion of the specimen. Classical beam theory indicates the shear stress varies from 75 to 100 percent of its maximum value over the central half of the beam whereas; the computer program indicates the variation is approximately 10 percent. Confidence in the computer results is enhanced when it is noted that failure in short beam interlaminar shear specimens (ASTM Designation D

2344) often occurs at locations as much as 20 percent of the beam depth above or below the neutral axis. Thus indicating that the shear stress distribution near the neutral axis may not vary as much as predicted by classical beam theory.

Interlaminar shear stress at the midplane and at the first-second layer interface are plotted as a function of position along the beam in figure 7.3. Boundary conditions B and the fourth set of material properties ($E_1/E_2 = 10$) listed in table 7.1 were used in the computations. Maximum stresses are predicted to occur at the quarter points. This result was anticipated since the slope of the deflected beam was maximum at the quarter points and transverse shear is directly proportional to the slope for the case under consideration.

3. Nonlinear Matrix Behavior

In order to illustrate the influence of nonlinear matrix behavior on shear stress distribution along the beam, the shear stress-strain curve shown in figure 7.4 was postulated. The curve is divided into five linear segments and the initial shear modulus equals 3.85×10^4 psi. Utilizing the stress-strain behavior indicated in figure 7.4 for the matrix, but retaining the other material properties used to develop figure 7.3, interlaminar shear stress along the length of the beam is predicted to vary in the manner shown in figure 7.5. Interlaminar shear stress along the neutral axis is maximum at the quarter points, as previously indicated in figure 7.3. Interlaminar shear stress along the first-second layer interface is also maximum at the quarter points but

remains nearly constant for ± 10 percent of the beam length on either side of the quarter points. The bluntness of the first-second layer interlaminar shear stress curve is a consequence of the nonlinear shear stress-strain behavior of the matrix and indicates that strain in the matrix has exceeded the proportional limit along approximately 60 percent of the beam.

While performing the computations required to construct figure 7.5, it was found that the matrix laminae had to be subdivided in order to obtain accurate results from the computer program. Thus a six layer beam is shown in the sketch on figure 7.5. In the computer program, the value of shear modulus used in each computation is based on the average shear stress across each lamina. As a result, the matrix laminae were subdivided in order to prevent the computer program from over estimating the interlaminar shear stress values. Each matrix lamina adjacent to a reinforcement lamina was only 0.025 inches thick whereas the remaining matrix laminae were 0.100 inches thick.

Figure 7.6 illustrates the effect of nonlinear shear behavior in the matrix on the shear instability load predicted by equation (5.17). The plot is based on the same material properties and laminae arrangement that were used to develop figure 7.5 and values of shear modulus corresponding to the average shear stress in each lamina at the beam quarter point. Axial load was applied in 25 equal increments. The 14th increment terminates at 490 pounds, the point where nonlinear shear behavior is initiated. During the next three load increments, shear stress in all matrix laminae exceeds the proportional limit shown in

figure 7.4 and the shear instability load drops to approximately 10 percent of its initial value. Throughout the remaining increments (figure 7.6), the change in shear instability is small. By utilizing smaller load increments and further subdividing the matrix laminae, the series of line segments shown in figure 7.5 could be replaced by a smooth curve.

4. Load Increment Size

A brief study of the influence of load increment size on the computer program results was performed. Utilizing the beam shown in figure 7.1, boundary conditions A and the fourth set of material properties ($E_1/E_2 = 10$) listed in table 7.1, rotations, transverse deflection, shear stresses and shear resultant were computed using four different size load increments. The results are listed in table 7.2. The load increments listed correspond to dividing the total load into 5, 10, 15 and 25 increments, respectively. Comparison of the rotations for each layer, indicates a change of less than 0.4 percent is obtained by decreasing the load increment size from 40 to 8 pounds. Transverse deflection is predicted to be constant over the range of load increments investigated. Changes in interlaminar shear stress and transverse shear resultant are insignificant compared to the accuracy of the analysis. Inspection of equation (4.53f) leads to the conclusion that the results listed in table 7.2 should be anticipated since the value of $\Delta P \ll \sum_{i=1}^n G_i A_i$. Use of load increments which correspond to larger ratios of $\Delta P/2 \sum_{i=1}^n G_i A_i$ are expected to show more variation in the results.

5. Boundary Conditions

Table 7.3 shows the influence of utilizing boundary conditions case A and case B on the computed displacements, rotations and interlaminar shear stresses. The objective of the study was to determine if the transverse displacement, laminar rotations and interlaminar shear stresses near the midplane of a thick laminate with free upper and lower surfaces could be accurately computed using a repeating element from the laminate with restrained upper and lower surfaces.

The results listed under case A are based on a 19 ply laminate (10 fiber or reinforcing laminae and 9 matrix laminae). Each lamina was 4.000 inches long, 0.500 inch wide, 0.083 inch thick and had an initial transverse deflection at the midspan of 0.020 inch. End loadings which correspond to a uniform axial strain, 0.004 in./in., were used in all computations. The rotations listed under case A are for the matrix lamina located at the midplane of the laminate and for the adjacent fiber lamina. Interlaminar shear stress for the two laminae just described is also listed.

Results listed under case B were computed for a single fiber lamina and the two adjoining half layers of matrix taken from the case A laminate. As indicated in table 7.3, the fiber lamina was subdivided for the purpose of analysis. A uniform axial strain, 0.004 in./in., was imposed in all computations.

Examination of table 7.3 indicates: (1) For $E_f/E_m = 100$ the results based on case A and case B boundary conditions are in reasonable agreement. (2) For $E_f/E_m = 10$, the comparison is less satisfactory and

for $E_f/E_m = 1$ the two sets of boundary conditions provide significantly different results. (3) Rotations, displacement and interlaminar shear stress based on case B boundary conditions are always less than the corresponding values based on case A boundary conditions.

Perhaps the use of a laminate with a lower length to depth ratio and a larger number of laminae would provide a more favorable comparison. This would tend to eliminate bending of the laminate about its neutral axis. Additional analysis is required to confirm this idea. Since most laminated specimens contain a small number of laminae (usually less than 20), table 7.3 clearly shows that case A boundary conditions should be used in analysis of the test results.

B. Experiment

1. Matrix Compression Test

Figure 7.7 shows compressive stress-strain curves determined for three specimens. Each curve is characterized by an initial linear segment which is followed by a nonlinear region. The linear behavior terminates at a strain of approximately 0.003 in./in. The specimens did not fracture. However, loading was terminated at the maximum strain shown for each specimen since it was believed that additional loading would not produce data applicable to the present study. The three curves shown in figure 7.7 were averaged, from 0 to 1000 psi, and the result is shown in figure 7.8. Young's modulus for the matrix material, based on the initial slope of the stress-strain curve in figure 7.8, is 169,500 psi.

2. Matrix Shear Test

Torque-twist tests on two specimens (refer to figures 6.6 and 6.12) produced essentially identical results. Figure 7.9 shows the shear stress-strain curve for one of the specimens. The curve is nonlinear and the slope continually decreases with increasing stress. Loading was terminated at the maximum stress level shown in figure 7.9 and the specimen showed no indication of failure. The initial portion of the curve, 0 to 0.012 in./in., is shown in figure 7.10. A piecewise linear representation of the curve shown in figure 7.10 is presented in figure 7.11. The latter curve was used to represent the matrix shear stress-strain behavior in the computer program described in Appendix A.

3. Matrix-Reinforcement Bond Strength Test

Three specimens (refer to figures 6.7 and 6.13) were tested to determine matrix-reinforcement bond strength and each test produced essentially identical results. Figure 7.12 shows a plot of shear stress as a function of testing machine head displacement. The curve is linear up to approximately 150 psi and then the slope begins to decrease with additional load. At a stress level of approximately 290 psi, the slope of the curve equals zero and indicates that the tube was being pushed through the base block (refer to figure 6.13). Bond strengths for the three specimens ranged from 290 to 293 psi, less than one half of the shear strength of the matrix.

4. Compression Test of Laminate Specimens

Failure loads and amplitude coefficients, a_0 , of the initial

deflection for each specimen are listed in table 7.4. It should be noted that specimens 1 and 2 contained 0.083 inch laminae and were identical except for the respective values of a_0 , whereas; specimens 3 and 4 contained 0.040 inch laminae and differed only in values of a_0 . All specimens failed by delamination and noting the values of a_0 , the failure loads appear to reflect the expected trend. That is, specimen 1 would be expected to fail at a lower load than specimen 2 and specimen 3 would be expected to fail at a lower load than specimen 4.

Figures 7.13 through 7.19 show failed laminate specimens. Figure 7.13 is a photograph of specimen 1 after failure. A delamination along the outer matrix lamina on the convex side of the specimen is clearly visible. The delamination, or crack, sheared through the matrix laminae approximately half way between the specimen quarter point and midspan. The specimen contains other delaminations which are not readily apparent in the photograph but could be seen by placing a light underneath the specimen. Close examination of the photograph also reveals that the ends of the specimen rotated at failure and are no longer perpendicular to the longitudinal centerline of the specimen. Figure 7.14 shows a close-up view of the cracked matrix laminae. Specimen 2 failed in the same manner as specimen 1 and the outer matrix layer failed at approximately the same location. Figure 7.15 shows a close-up view of the failed matrix layer in specimen 2.

After specimen 1 had been failed, the screws which clamped the ends were removed. At that point, the lamina fell apart. Figure 7.16 shows the individual lamina from specimen 1. The surfaces of both the aluminum

and matrix laminae are very smooth and indicate that the bond between laminae was weak.

Figure 7.17 is a photograph of specimen 4 after failure. It also contains a delamination along the outer matrix lamina but the crack does not pass through the matrix. Figure 7.18 shows a close-up view of specimen 4 and additional delaminations are visible. After specimen 4 had been failed, the screws which clamp the ends were also removed and it fell apart, as indicated in figure 7.19. The surfaces of the laminae from specimen 4 were smooth and also indicate a weak bond between laminae. The appearance of specimen 3 after failure was similar to that of specimen 4.

Figures 7.20 through 7.31 show load-strain and load-deflections plots obtained from tests on the laminate specimens. Figure 7.20 shows the strain gage data for specimen 1. Gages 1 and 4, (refer to figure 6.8 for strain gage and DCDT locations) indicate a small amount of bending in the two outer laminae. Load-strain curves for gages 2 and 3 do not indicate bending of the laminate about its midplane. Also, gages 5 through 8 which were located at the quarter points do not indicate bending of the laminate.

Load-transverse displacement plots for specimen 1 are shown in figure 7.21. The data, DCDT's 1, 5, 6, and 10, indicated fixed end boundary conditions were not maintained throughout the test. However, displacements at the ends of the matrix laminae were small, less than 0.0005 inch for the lower end and approximately 0.0012 for the upper end. The remaining DCDT's indicated nonlinear load deflection curves

and that the deflection is approximately symmetric with respect to the midspan of the specimen. All DCCT's positioned on the convex side of the specimen indicated larger displacements than the corresponding DCCT's on the concave side of the specimen. At the midspan, transverse displacement at failure on the convex side was approximately 1.3 times the displacement on the concave side. However, the difference was only about .00115 inch which is small compared to the width of the specimen.

Figure 7.22 is a load-shortening plot for specimen 1. Except near the origin, the curve is linear.

Figures 7.23 through 7.25 show similar strain gage data for specimen 2. At an axial load of approximately 5000 pounds, irregular behavior was observed. The specimen did not produce an audible sound at this load or other indications of failure. It is possible, although as yet unproven, that a malfunction in the data recording system was experienced. It is also noted that DCCT 7 (figure 7.24) did not appear to be functioning properly during the test. The irregular behavior was not detected in the load-shortening data shown in figure 7.25. While the strain gage and deflection data for specimen 2 has not been completely explained, it does indicate the same general trends as the data for specimen 1.

Figures 7.26 through 7.31 present load-deflection and strain data for specimens 3 and 4. The data leads to the same conclusions stated about specimen 1.

5. Compression Test of Fiber Reinforced Composites

Nine tubular specimens were tested to failure in axial compression. Table 6.3 lists the maximum stress supported by each specimen. Failure of specimens 1-1, 1-2, and 1-3, (11 ply 4 mil boron filament reinforced epoxy) ranged from 277 to 297 ksi and average 286 ksi. The 10 ply 5.6 mil boron filament reinforced epoxy tubes (specimens 2-1, 2-2 and 2-3) failed between 302 and 322 ksi with an average stress at failure equal to 314 ksi. Two of the S-glass-epoxy specimens failed at stresses which differ by less than 10 percent whereas; the third specimen failed at about 70 percent of the average strength for the first two specimens. The low strength of the third specimen was not expected and perhaps is attributable to a short longitudinal crack which was not detected when the specimen was visually inspected prior to testing.

Figures 7.32, 7.33 and 7.34 show failed compression specimens. Numerous longitudinal cracks and broken filaments are exhibited by all specimens. In addition, failure appears to have initiated in the central portion of the specimen.

Load-strain plots for all nine specimens are presented in figures 7.35 through 7.43. The figures which show three plots are based on data obtained from three strain gages located at 90 degree intervals around the circumference and at the midspan of the specimen. All three gages were aligned parallel to the longitudinal axis of the specimen and gages 1 and 2 were diametrically opposite. The data indicate that boron-epoxy specimens 1-1, 1-2, 2-2, and 2-3 may have failed by column buckling but does not indicate a mode of failure for glass-epoxy

specimen 3-1. Young's modulus values listed in table 6.3 for specimens 1-1, 1-2, 2-2, 2-3, and 3-1 were determined using the initial slope of the load-strain curves.

Figures 7.37, 7.38, 7.42 and 7.43 each show five load-strain plots. Gages 1, 2, and 3 formed a 0, ± 45 degree rosette which was located at the quarter point along the length of the specimen. Gage 3 was aligned parallel to the longitudinal axis. Gages 4 and 5 were located at the midspan and 90 degrees and 180 degrees, respectively, around the circumference from gage 3. Gages 4 and 5 were also aligned parallel to the longitudinal axis of the specimen. Data obtained from gages 3, 4, and 5 on boron-epoxy specimens 1-3 and 2-1 (fig. 7.37 and 7.38) indicate that they may have failed by column buckling. However, gages 1 and 2 indicate that the cross sectional shape of the specimens started to change prior to failure and thus indicate that cylinder buckling may have influenced failure. Figures 7.42 and 7.43 present data on glass-epoxy specimens 3-2 and 3-3. The results shown in figure 7.42 supports the possibility of failure by column and/or cylinder buckling. Data shown in figure 7.43, appears to only indicate failure by cylinder buckling. Young's modulus values listed in table 6.3 for specimens 1-3, 2-2, 3-2 and 3-3 were determined using the initial slope of the load-strain curves obtained with gages 3, 4 and 5.

Based on the data presented in figures 7.35 through 7.43, failure of the fiber reinforced compression specimens appears to have been initiated by column and/or cylinder buckling.

6. Torsion Test of Fiber Reinforced Composites

Specimens 1-4, 2-4, and 3-4 listed in table 6.3 were tested to failure in torsion. All specimens failed by cracking parallel to the longitudinal axis. Figures 7.44 and 7.45 show failed specimens. Shear stress-strain curves determined from the tests are presented in figures 7.46 through 7.48. All specimens exhibited nonlinear stress-strain behavior. Failure of specimens 1-4, 2-4, and 3-4 ranged from 9.55 to 9.90 ksi.

In addition to testing specimens 1-4, 2-4 and 3-4, specimens 1-6 and 3-5 were tested in torsion after they had been subjected to combined compression and torsion tests. Shear stress at failure for each specimen is listed in table 6.3. A short crack was observed in specimen 3-5, prior to torsion testing and failure occurred along the cracked area at approximately 80 percent of the strength measured for specimen 3-6. Figure 7.49 shows the stress-strain plot for specimen 1-6 and it is nearly identical to the plot for specimen 1-4.

7. Combined Compression and Torsion Test of Fiber Reinforced

Composites

In order to determine the effect of axial compressive stress on shear modulus for fiber reinforced composite materials, specimens 1-5, 1-6, 3-5 and 3-6 were subjected to combined loading test. During these tests, shear stress-strain curves were developed as a function of applied axial compression stress. Figure 7.50 shows the plots for specimen 1-5. Close examination of the plots indicates that the slope (shear modulus) decreases with increasing values of compressive stress. Similar plots

were constructed for the remaining specimens and used to determine shear modulus as a function of compressive stress.

Figures 7.51 through 7.54 summarize the results which are presented in the form of apparent shear modulus-applied axial compression stress plots. The dashed line in each figure represents the relationship

$$G^* = G - \sigma_c \quad (7.1)$$

which is readily derived using energy methods and is based on shear modulus being independent of the applied compressive stress. Except for low values of compressive stress, the experimentally determined values of G^* for the boron-epoxy specimens (figures 7.51 and 7.52) do not agree with equation (7.1). The difference increases with increasing values of applied stress and thus indicates that shear modulus of the composite decreases with increasing applied stress. A curve, which intersects the abscissa at the highest compressive strength for boron-epoxy known to the author, has been drawn through the data. Based on the data shown, it appears reasonable to conclude that the maximum compressive strength of boron-epoxy is limited by shear instability ($G^* = 0$).

Results for the glass-epoxy specimens (figures 7.53 and 7.54) are inconclusive. Specimen 3-6 exhibited behavior which differed from the prediction of equation (7.1) whereas data on specimen 3-5 agrees with equation (7.1). The inconclusiveness is due perhaps to the low ratios of σ_c/G that could be investigated, since the axial stress had to be kept below approximately 140 ksi to prevent failure of the specimens.

C. Comparison of Experiment and Theory

1. Laminate Specimens

Table 7.5 lists predicted values of transverse displacement and interlaminar shear stresses at the quarter points for the central matrix lamina and the outermost matrix laminae. Values of w_1 listed in the table equal the difference between final and initial displacements and the experimental values represent the average of displacements measured on opposite edges of the specimen. Theoretical results for each laminate were calculated using the computer program described in appendix A, case A boundary conditions described herein and the experimentally determined failure load.

Comparison of the midspan displacements shows reasonable agreement, the differences average less than 15 percent. Quarter point displacements are in excellent agreement for specimen 1 although they show significant differences for specimens 3 and 4. Specimen 3 shows less agreement, at the quarter points, than the other specimens and this is attributed to the difference between its initial displacement and the assumed initial displacement (refer to figure 6.4). In addition, the predicted displacements are based on fixed end boundary conditions which were not completely simulated. Taking these items into consideration the comparison between predicted and measured displacements appears to be satisfactory.

Predicted values of interlaminar shear stress for the middle lamina in each specimen exceed the bond strength by as much as 75 percent. Agreement between the bond strength and predicted values of interlaminar

shear stress for the outermost matrix laminae is much better and the average difference is 15 percent. In view of these data, observation of the failed specimens and the matrix to reinforcement bond strength test results, the following argument is offered. As the applied axial load increases, interlaminar shear stresses along the inner laminae increase until the maximum bond strength is attained. However failure does not occur at this point since the laminae are still in contact with each other and continue to transfer load across the interfaces. In other words, the laminae exhibit behavior similar to the bond strength specimens (refer to figure 7.12). Application of additional load increases interlaminar shear stresses in the outer laminae until the bond-strength is attained at the outermost interface. At this point, the outer reinforcement lamina on the convex side of the laminate buckles and failure occurs. This leads to the conclusion that adequate correlation between experiment and the interlaminar shear analysis was achieved.

2. Fiber Reinforced Composite Test Results

A study was performed to determine if the interlaminar shear stress analysis presented herein could be used to predict the type of behavior exhibited by the combined compression and torsion tests. The 4 mil boron-epoxy composite was modeled by the laminate shown in figure 7.55 and case B boundary conditions were assumed for the analysis. The shear stress-strain curve for the epoxy was computed using the stiffness in series model and the experimentally determined shear stress-strain curve for specimen 1-6. The computed curve is shown in figure 7.56. The

interlaminar shear stress computer program used five linear segments to represent the curve shown in figure 7.56.

Table 7.6 lists the computed results and the loading and curvature parameters (a_o , L) used in the analysis. The value of a_o was varied from .0005 to .0030 inch whereas; a value of .8 inch for L , which is equal to 200 times the fiber diameter, was used in all computations. Values of matrix shear stress listed in the table represent the maximum value and the average value along the length of the model. The average shear stress and figure 7.56 were used to compute the values of G_m listed. Values of G_{LT} listed in the table were calculated using the stiffness in series model and the tabulated value of G_m . The last column lists values of apparent shear modulus ($G_{LT} - \sigma_c$). Examination of the tabulated results indicate the following: (1) For $a_o/L < 0.001875$ and $\sigma_c \leq 468$ ksi, the average value of G_m is constant and the variation in G^* is due only to changes in σ_c . (2) At some value of σ_c between 312 and 390 ksi and $a_o/L = 0.001875$, the value of G_m begins to decrease and thus causes changes in G^* . (3) For $a_o/L = 0.003750$, G_m begins to decrease at a lower value of σ_c , between 156 and 312 ksi. (4) Increasing the value of a_o/L would indicate failure by delamination since the maximum shear strength is approximately 9700 psi.

Figure 7.75 shows a plot of G^* as a function of applied stress. Only values which differ from elementary theory ($G_{LT} = \text{constant}$) have been identified by symbols since the remaining values are represented by the solid line. Dashed lines have been drawn through the points to only illustrate trends in the data, which indicate that small values of

initial deflection can have a significant effect on the apparent shear modulus, G^* . Based on the data shown two conclusions are drawn: (1) Behavior similar to that determined experimentally on boron-epoxy (refer to figures 7.51 and 7.52) can be predicted using the interlaminar shear stress analysis developed herein. (2) Only very small values of initial deflection are required to predict the indicated behavior. Concerning the latter conclusion, a brief study on initial displacement of the fibers in a boron-epoxy composite was conducted and the results are presented in appendix C. The results indicate that initial displacement values, a_0/L , used in the analysis are of the same order of magnitude as the measured deflections. Thus, adequate correlation between the analysis and experiment appears to have been achieved.

VIII. CONCLUDING REMARKS

A theoretical and experimental investigation on the compressive strength of lamina reinforced and fiber reinforced composite materials has been performed. An analytical model which replaces the fiber reinforced composite with a laminate containing initially curved laminae has been proposed. By applying the Timoshenko beam equations to each layer in the laminate, an interlaminar shear stress analysis which can be used to predict the behavior of the laminate under compressive loading was developed. Experimental evidence that the shear modulus of boron-epoxy is a function of axial compressive stress was obtained. In addition it was shown that the fibers in a boron-epoxy composite are not parallel and straight but contain initial curvature. Both the experimental and theoretical results indicate that failure of the boron-epoxy composite is most likely due to shear instability. Adequate correlation between theory and experiment was obtained for both lamina reinforced and fiber reinforced test results.

IX. REFERENCES

1. Dow, N. F.; and Gruntfest, I. J.: Determination of Most-Needed, Potentially Possible Improvements in Materials for Ballistic and Space Vehicles. General Electric Technical Information Series R6OSD389, June 1960.
2. Timoshenko, S.: Theory of Elastic Stability. McGraw-Hill Book Company, Inc., 1936, pp. 111.
3. Elkin, Robert A.: Compression testing of NOL Rings. Symposium on Standards for Filament-Wound Reinforced Plastics, ASTM Special Technical Publication No. 327, June 1962.
4. Fried, N.: The Compressive Strength of Parallel Filament Reinforced Plastics - The Role of the Resin. Proceedings 18th Annual Technical and Management Conference, Reinforced Plastics Div., Soc. Plastics Ind., Inc., February 1963.
5. Fried, N.; and Kaminetsky, J.: The Influence of Material Variables On the Compressive Properties of Parallel Filament Reinforced Plastics. Proceedings 19th Annual Technical and Management Conference, Reinforced Plastics Div., Soc. Plastics Ind., Inc., February 1964.
6. Rosen, B. W.: "Mechanics of Composite Strengthening", Fiber Composite Materials, American Society of Metals, Metals Park, Ohio, October 1964.
7. Dow, Norris F.; and Rosen, B. Walter: Evaluation of Filament-Reinforced Composites for Aerospace Structural Applications. NASA CR-207, April 1965.
8. Fried, N.: The Response of Orthogonal Filament Wound Materials to Compressive Stress. Proceedings 20th Anniversary Technical Conference, Reinforced Plastics Div., Soc. Plastics Ind., Inc., February 1965.
9. Ekvall, J. C.: Structural Behavior of Monofilament Composites. 6th AIAA Structures and Materials Conference, Palm Springs, California, April 5-7, 1965.
10. Schuerch, H.: Compressive Strength of Boron-Metal Composites. NASA CR-202, April 1965.
11. Schuerch, H.: Prediction of Compressive Strength of Uniaxial Boron Fiber-Metal Matrix Composite Materials. AIAA Journal. vol. 4, no. 1, January 1966, pp. 102-106.

12. Anon: Micromechanics - Compressive Properties of Fiber Reinforced Composites. AFML-TR-237, May 1965.
13. Levenetz, Boris: Compressive Applications of Large Diameter Fiber Reinforced Plastics. Proceedings 19th Annual Technical and Management Conference, Reinforced Plastics Div., Soc. Plastics Ind., Inc., February 1964.
14. Biot, Maurice A.: Mechanics of Incremental Deformations. John Wiley and Sons, Inc., 1965, pp. 257.
15. Foye, R. L.: Compressive Strength of Unidirectional Composites. AIAA Paper No. 66-143, January 1966.
16. Dow, Norris F.; Rosen, B. W.; and Hashin, Zvi: Studies of Mechanics of Filamentary Composites. NASA CR-492, June 1966.
17. Herrmann, L. R.; Mason, W. E.; and Chan, S. T. K.: Behavior of Compressively Loaded Reinforcing Wires. Structural Engineering Laboratory Report 67-2, University of California, Berkeley, January 1967.
18. Herrmann, Leonard R.; Mason, William E.; and Chan, S. T. K.: Response of Reinforcing Wires to Compressive States of Stress. Journal of Composite Materials, vol. 1, July 1967, pp. 212-226.
19. Sadowsky, M. A.; Pu, S. L.; and Hussain, M. A.: Buckling of Microfibers. Transactions of the ASME, Journal of Applied Mechanics, December 1967, pp. 1011-1016.
20. Crawford, R. F.: An Evaluation of Boron-Polymer Film Layer Composites for High-Performance Structures. NASA CR-1114, September 1968.
21. Yue, A. S.; Crossman, F. W.; Vidoz, A. E.; and Jacobson, M. I.: Controlled Microstructures of Al-CuAl₂ Eutectic Composites and Their Compressive Properties. Transactions of the Metallurgical Society of AIME, vol. 242, December 1968, pp. 1968-2441.
22. Lager, John R.; and June, Reid R.: Compressive Strength of Boron-Epoxy Composites. Journal of Composite Materials, vol. 3, January 1969, pp. 48-56.
23. Chung, Wen-Yi; and Testa, Rene B.: The Elastic Stability of Fibers In A Composite Plate. Journal of Composite Materials, vol. 3, January 1969, pp. 58-80.

24. Guz, O. M.: Determination of the Theoretical Compression Strength of Reinforced Materials. (Pro Viznachennia Teoretichnoi Granitsi Mitsnosti Na Stisk Armovanikh Materialiv, Dopovidi Akademii Nauk Ukrayns' Kcy RSR, Seriya A, Fiziko-Tekhnichni i Matematichni Nauki, vol. 31, March 1969, pp. 236-238.) (Also available as NASA TT F-13, 433.)
25. Skudra, A. M.; Kalnays, A. A.; and Bulavs, F. Ya.: Creep-Rupture Strength of Reinforced Plastics Under Uniaxial Compression. (Akademiia Nauk Latviiskoi SSR, Institit Mekhaniki Polimerov, Riga, Latvian SSR), Mekhanika Polimerov, vol. 5, July-August 1969, pp. 621-628. (Also available as NASA TT F-13, 441.)
26. Davis, John G., Jr.: Fabrication of Uniaxial Filament-Reinforced Epoxy Tubes For Structural Applications. Advanced Techniques For Material Investigation and Fabrication, SAMPE vol. 14, Soc. Aerosp. Matl. Process Engr., c. 1968, paper II-2A-1.
27. Chamis, Christos C.: Failure Criteria For Filamentary Composites. NASA TN D-5367, August 1969.
28. Guz, A. N.; Kritsuk, A. A.; and Yemel'yanov, R. F.: Nature of the Failure of A Unidirectional Fiberglass-Reinforced Plastic Under Compression. (Akademiia Nauk Ukrainiskoi SSR, Institut Mekhaniki, Kiev, Ukrainian SSR.) Prikladnaia Mekhanika, vol. 5, September 1969, pp. 118-121. (Also available as NASA TT F-13, 442.)
29. DeFerran, E. Moncunill; and Harris, B.: Compressive Strength of Polyester Resin Reinforced With Steel Wires. Journal of Composite Materials, vol. 4, January 1970, pp. 62-71.
30. Davis, John G., Jr.: Compressive Instability and Axial Strength of Uniaxial Filament-Reinforced Epoxy Tubes. NASA TN D-5697, March 1970.
31. Pinnel, M. R.; and Lawley, A.: Correlation of Uniaxial Yielding and Substructure in Aluminum-Stainless Steel Composites. Metallurgical Transactions, vol. 1, May 1970, pp. 1337-1348.
32. Hayashi, Tsuyoshi: Compressive Strength of Unidirectionally Fibre Reinforced Composite Materials. 7th International Reinforced Plastics Conference, October 20-22, 1970, pp. 11/1 - 11/3.
33. Hayashi, Tsuyoshi: On the Shear Instability of Structures Caused by Compressive Load. AIAA Paper No. 65-770, November 1965.
34. Guz, A. N.: On Setting Up a Stability Theory of Unidirectional Fibrous Materials. Institute of Mechanics, Academy of Sciences of the Ukrainian SSR. (Translated from Prikladnaya Mekhanika, vol. 5, no. 2, February 1969, pp. 62-70.)

35. Guz, A. N.: Constructing A Theory for the Strength of Unidirectionally Reinforced Materials in Compression. Institute of Mechanics, Academy of Sciences of the Ukrainian SSR, Kiev. (Translated from Problemy Prochnosti, no. 3, March 1971, pp. 37-39.)
36. Ervins, P. D.: A Compressive Test Specimen for Unidirectional Carbon Fibre Reinforced Plastics. Royal Aircraft Establishment, Farnborough, England, Current Paper No. 1132, January 1970.
37. Pattnaik, A.; and Lawley, A.: Deformation and Fracture in Al-CuAl₂ Eutectic Composites. Metallurgical Transactions, vol. 2, June 1971, pp. 1529-1536.
38. Orringer, Oscar: Compressive Behavior of Fiber Composites. Air Force Office of Scientific Research, ASRL TR 162-1, October 1971.
39. Greszczuk, L. B.: Microbuckling of Unidirectional Composites. AFML-TR-71-231, January 1972.
40. Suarez, J. A.; Whiteside, J. B.; and Hadcock, R. N.: The Influence of Local Failure Modes on Compressive Strength of Boron/Epoxy Composites. Composite Materials: Testing and Design. ASTM STP 497, February 1972, pp. 237-256.
41. Hadcock, R. N.; Corvelli, N. J.; and Weingart, D.: Analysis of a Short Beam Shear Test Specimen. Composites Technical Note CTN-462-18, Grumman Aircraft Engineering Corporation, February 1968.
42. Sednor, Gerald; and Watterson, Rodney K.: Low Cycle Compressive Fatigue Failure of E Glass-Epoxy Composites. Air Force Office of Scientific Research, ASRL TR-162-2, March 1972.
43. Lanir, Y.; and Fung, Y. C. B.: Fiber Composite Columns Under Compression. Journal of Composite Materials, vol. 6, July 1972, pp. 387-401.
44. Harris, Byran: The Strength of Fibre Composites. Composites, vol. 3, no. 4, July 1972, pp. 152-167.
45. Ruzauskas, E. J.; and Hay, D. Robert: Fracture Modes in Metal Matrix Composites. Journal of Composite Materials, vol. 6, July 1972, pp. 414-419.
46. Gorb, M. L.; Marek, B. A.; and Teodorovich, O. K.: The Compressive Strength of Copper Reinforced with Tungsten Fiber. Problemy Prochnosti, vol. 3, November 1971, pp. 95-97. (Strength of Materials, vol. 3, no. 11, July 1972, pp. 1355-1357.)

47. Hackett, R. M.; Tarpay, T. S., Jr.; and Wood, J. L.: An Analysis of Fiber Buckling. *Polymer Engineering and Science*, vol. 12, no. 4, July 1972, pp. 272-276.
48. Greszczuk, L. B.: Failure Mechanics of Composites Subject to Compressive Loading. AFML TR-72-107, August 1972.
49. Greszczuk, L. B.: Interfiber Stresses in Filamentary Composites. *AIAA Journal*, vol. 4, no. 7, July 1971.
50. Norris, C. E.: Strength of Orthotropic Materials Subjected to Combined Stresses. Forest Products Laboratory Report, FPL, 1816, July 1950.
51. Kao, B. C.; and Pipkin, A. C.: Finite Buckling of Fiber-Reinforced Columns. *Acta Mechanica*, vol. 13, no. 304, 1972, pp. 265-280.
52. Argon, A. S.: Fracture of Composites. *Treatise on Material Science and Technology*, vol. 1, Academic Press., Inc., 1972, pp. 79-114.
53. Kulkarni, Satish V.; Rice, Joseph S.; and Rosen, B. Walter: An Investigation of the Compressive Strength of PRD-III/Epoxy Composites. NASA CR-112334, May 1973.
54. Timoshenko, S. P.: On the Transverse Vibrations of Bars of Uniform Cross-Section. *Phil. Mag.*, vol. 43, 1922, pp. 125-131.
55. Heller, R. A.: Interlaminar Shear Stress in Sandwich Beams. *Experimental Mechanics*, vol. 26, September 1969, pp. 413-418.
56. Heller, R. A.; and Swift, G. W.: Solutions for the Multilayer Timoshenko Beam. Department of Engr. Mech., Virginia Polytechnic Institute Report No. VPI-E-71-12. Contract No. DAA-FO7-70-C-044, August 1971.
57. Swift, G. W.: The Solution of N Simultaneous Second Order Coupled Differential Equations by the Finite Difference Method. Dept. of Engr. Mech., Virginia Polytechnic Institute Report No. VPI-E-71-3. Contract No. DAA-FO7-70-C-0444, February 1971.
58. Mindlin, R. D.; and Deresiewicz, H.: Timoshenko's Shear Coefficient For Flexural Vibrations of Beams. *Proc. Second U.S. Natl. Congress of Appl. Mech.*, 1954, pp. 175-178.
59. Reissner, E.: The Effect of Transverse Shear Deformation on the Bending of Elastic Plates. *J. Appl. Mech.*, vol. 12, 1945, pp. A69-77.

60. Cowper, G. R.: The Shear Coefficient in Timoshenko's Beam Theory. Transactions of the ASME, Journal of Applied Mechanics, June 1966, pp. 335-340.
61. Zienkiewicz, O. C.: The finite Element Method in Structural and Continuum Mechanics. McGraw-Hill Publishing Co., Ltd., London, 1967, pp. 234-235.
62. Sands, A. G.; Clark, R. C.; and Kohn, E. J.: Microvoids in Glass-Filament-Wound Structures: Their Measurement, Minimization and Correlation with Interlaminar Shear Strength. NRL Report 6498, U.S. Navy, March 31, 1967.
63. Davis, John G., Jr.; and Zender, George W.: Compressive Behavior of Plates Fabricated from Glass Filaments and Epoxy Resin. NASA TN D-3918, 1967.
64. Rummeler, Donald R.; Dexter, H. Benson; Harth, George H., III; and Buchanan, Raymond A.: Mechanical Properties and Column Behavior of Thin-Wall Beryllium Tubing. NASA TN D-4833, 1968.

APPENDIX A - INTERLAMINAR SHEAR STRESS COMPUTER PROGRAM

This appendix provides a brief description of the computer program used to calculate interlaminar shear stresses. Figure A-1 shows a flow diagram of the program. First the problem is defined by reading in the beam geometry, including the maximum amplitude of the initial deflection and the number of node points to be used, the boundary conditions and the material properties. Linear elastic behavior is assumed for extension and compression of each lamina but the shear stress-strain curve may be approximated by five linear segments. Next, the quantities that remain constant throughout the computation cycles are calculated. These include lamina thickness, cross sectional area, first moment of area, and the second moment of area. In addition, Euler buckling load and total applied axial load are computed and the counter, IPK, which is used to keep track of the number of computation cycles through the program, is set equal to zero.

Initial displacements and rotations and their first and second derivatives at each node point along the beam are computed next and stored on tape for subsequent use in the program. The initial values of interlaminar shear stress at each node are set equal to zero. Next, the counters that are used in storing and keeping track of the \underline{R} , \underline{S} , and \underline{T} matrices for each node point along the beam are computed.

Prior to computing the coefficients of the \underline{R} , \underline{S} , and \underline{T} matrices, the average shear stress within each lamina is computed. Then the appropriate values of shear modulus to be used in the subsequent calculations are computed utilizing the five segment stress-strain curves

read in at the beginning of the program. The values of \underline{R} , \underline{S} , and \underline{T} are stored on tape.

After the coefficient matrices have been generated, the recurrence matrices and the load vector, starting at node 2 and continuing through the node one station to the left of $x = L$, are computed and stored on tape. Then beginning one node away from the right end of the beam, the recurrence matrices and load vector are recalled from tape and values of the rotations and displacements, $\underline{Y}(n)$, are solved by back substitution. Each value of $\underline{Y}(n)$ is stored on tape for subsequent use in computing first and second derivatives.

Next the counter, IPK , is increased by one and the first and second derivatives at each node along the beam are computed. Forward and backward difference routines are used to compute derivatives at the left and right ends of the beam, respectively. At all other node points, central differences are used. After the derivatives have been computed and stored, interlaminar shear stresses at each node are calculated and stored on tape. The transverse shear resultant at 51 node points along the beam is also computed and stored.

Utilizing the shear modulus values that were used to generate the \underline{R} , \underline{S} , and \underline{T} matrices, the value of axial load which will cause shear instability is computed using equation (5.17). If the shear stress-strain curves are nonlinear, the load which produces instability will decrease as the axial load increases.

If $IPK \neq 1$, the program proceeds to location ③ and the tapes storing displacements, rotations, derivatives, and interlaminar shear stresses

are updated using the principle of superposition. If $IPK = 1$, the average shear stress within each lamina at the beam quarter point is computed and compared with the value of shear stress corresponding to the first break in the five segment stress-strain curve of the lamina. If all ratios are less than unity, the program proceeds to location ③ and subsequent computation cycles are not required.

If any ratio (τ_{BAR_i}/τ_i) is greater than unity, the maximum value is determined and linear interpolation is used to compute the value of axial load, PLO , which initiates nonlinear behavior. This value of load is used in the next computation cycle through the program. Next the size of the load increments for use in the load range PLO to $P1$ are computed and the program returns to location ① on the flow chart.

After location ③ on the flow diagram has been reached and the tapes have been updated, the counter IPK is checked to determine if the maximum load, $P1$, has been reached. If not, the program returns to location ① on the flow diagram and another computation cycle is initiated. After the displacements, rotations and stresses due to the maximum load have been computed, the data are displayed in the form of plots and tables.

APPENDIX B - CLASSICAL BEAM THEORY DEFLECTION
FOR CASE A AND CASE B BOUNDARY CONDITIONS

An equation for predicting the lateral deflection of an initially deformed beam under axial load is derived in this appendix. Free body diagrams of the beam are shown in figures B-1 and B-2. For case A, the following assumptions are made: the ends are clamped, the upper and lower surfaces are free, the beam may be considered to be homogeneous with an apparent bending stiffness, EI, and classical beam theory assumptions are applicable. The initial deflection, w_0 is given by

$$w_0 = a_0 \{1 + \sin[(2\pi/L)(x - L/4)]\} \quad (B-1)$$

and the total deflection, w , is given by

$$w = w_0 + w_1 \quad (B-2)$$

From classical beam theory

$$EI w_1'' = M \quad (B-3)$$

and summing moments, M , about the right end of the beam segment shown in figure B-1 leads to

$$M = -Pw + M_1 + Q_1(L - x) \quad (B-4)$$

Noting that M_1 and Q_1 are constants and differentiating equations (B-3) and (B-4) twice yields

$$w_1'''' + (P/EI)w_1'' = -(P/EI)w_0'' \quad (B-5)$$

The solution to equation (B-5) is

$$w_1 = A \sin k_0 x + B \cos k_0 x + cx + D + F \sin [(2\pi/L)(x - L/4)] \quad (B-6)$$

where

$$k_o^2 = P/EI \quad (B-7)$$

Applying the boundary conditions for case A to evaluate the constants of integration in equation (B-6) leads to the desired equation

$$v = \frac{a_o}{1 - \frac{k_o^2 L^2}{4\pi^2}} (1 + \sin [(2\pi/L)(x - L/4)]) \quad (B-8)$$

Since axial load P , appears in the denominator of the first term on the right side of equation (B-6), $k_o^2 = P/EI$, lateral deflection will not increase linearly with load and instability will occur as the load approaches P_{cr} , which is given by

$$P_{cr} = \frac{4\pi^2 EI}{L^2} \quad (B-9)$$

and is identical to the Euler buckling load for a fixed-end column.

For case B, the following assumptions are made: the ends of the beam are clamped, the upper and lower surfaces are not permitted to translate in the horizontal direction, the reinforcing laminae is subject to bending deformation only, bending stresses in the matrix laminae are negligible compared to those in the reinforcement and the matrix is considered to only support shear stresses, classical beam theory assumptions are applicable for the reinforcement. Summing moments about the right end of the beam segment shown in figure B-2, leads to

$$M = -Pv + M_1 + Q_1(L - x) + \int_0^x \tau(h + 2c) dx \quad (B-10)$$

Substituting equation (B-10) into (B-3) and noting

$$\tau_m = G_m(1 + h/2c) w_1' \quad (\text{B-11})$$

yields

$$w_1'''' + \left[\frac{P}{EI} - \frac{(h + 2c)^2 G_m}{2c EI} \right] w_1'' = \frac{4\pi^2 a_o P}{L^2 EI} \sin \left[\left(\frac{2\pi}{L} \right) \left(x - \frac{L}{4} \right) \right] \quad (\text{B-12})$$

The solution to (B-12) is

$$w_1 = A \sin k_1 x + B \cos k_1 x + cx + D + F \sin \left[\left(\frac{2\pi}{L} \right) \left(x - \frac{L}{4} \right) \right] \quad (\text{B-13})$$

where

$$k_1^2 = k_o^2 - \frac{(h + 2c)^2 G_m}{2c EI} \quad (\text{B-14})$$

Applying the boundary conditions for case B to equation (B-10), leads to the desired equation

$$w = a_o \left[1 + \frac{k_o^2}{\left(\frac{2\pi}{L} \right)^2 - k_1^2} \right] \left\{ 1 + \sin \left[\left(\frac{2\pi}{L} \right) \left(x - \frac{L}{4} \right) \right] \right\} \quad (\text{B-15})$$

Equation (B-15), like equation (B-7), is nonlinear with respect to the axial load. Instability for case B is seen to occur as k_1^2 approaches $(2\pi/L)^2$. The buckling load is given by

$$P_{cr} = \frac{4\pi^2 EI}{L^2} + \frac{(h + 2c)^2 G_m}{2c} \quad (\text{B-16})$$

If $(h/L \ll 1)$, a condition met by most composites of current interest,

the first term in equation (B-16) may be neglected and the buckling stress is given by

$$\sigma = \frac{G_m}{1 - \nu_m} \quad (\text{B-17})$$

which is identical to the failure stress predicted by Rosen (6).

APPENDIX C FIBER CURVATURE INVESTIGATION

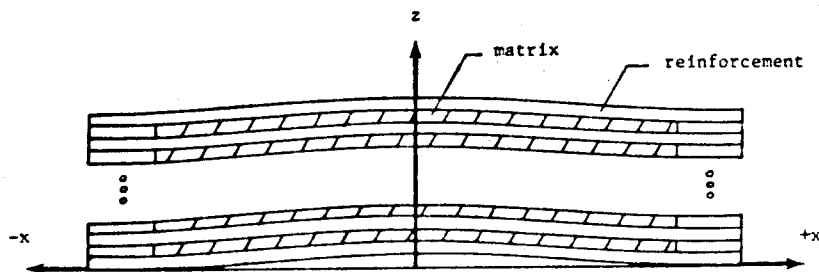
The method used to determine the coordinates of fibers in a boron-epoxy composite and the results obtained are discussed in this appendix. A 0.500 inch wide strip was machined from the central portion of a 6.00 inch wide by 4.00 inch long 12 ply laminate. The fibers were aligned in the length direction of the strip. Next the strip was sliced into nominally 0.10 inch thick coupons. (See figure C.1.) The thickness of each coupon was measured with a micrometer and then the coupon was mounted for viewing under a tool maker's microscope. Next the x and y coordinates of five arbitrarily selected fibers were measured.

Table C.1 and figure C.2 present the results obtained at 22 cross sections along the length of the strip. The z coordinates listed in the table reflect the fact that 0.070 inch of material was removed by each cut across the strip and indicate that x and y coordinates were measured at approximately 0.170 inch intervals along the strip. Thus, successive stations were approximately 42.5 fiber diameters apart. Examination of the results indicates: (1) Variation in the x coordinate was usually much larger than the variation of the y coordinate. (2) Four of the fibers are skewed with respect to the z axis. (3) All fibers are essentially parallel to the x-z plane. (4) All fibers exhibit waviness along their length. Item (2) does not appear to be as significant as the plots tend to indicate since the average angle, $[(x_{22}-x_1)/3.6426]$, between each fiber and the z axis is less than 0.24 degrees. Item (4) is perhaps the most important since it can lead to development of shear

stresses when the fiber is compressed in the axial direction. Displacements ranging from 0.0006 to 0.0012 inch over a span of 0.34 inch are readily seen.

Due to the irregular wave shape along each fiber, no attempt was made to express the displacement by a mathematical function. However, in segments of fibers are examined and equation 4.63 is used to express the displacement, the values of a_0/L required to fit the deflection range approximately from 0.0009 to 0.001875 (0.0006/0.68 to 0.0012/0.68).

TABLE 6.1 - LAMINATE SPECIMEN DIMENSIONS



x, in.	SPECIMEN NO. 1			SPECIMEN NO. 2		
	z_L , in.	z_U , in.	t, in.	z_L , in.	z_U , in.	t, in.
-2.44	0.0000	1.5794	1.5794	-0.0000	1.5816	1.5816
-2.25	-0.0032	1.5737	1.5769	-0.0007	1.5765	1.5772
-2.00	-0.0065	1.5713	1.5778	-0.0030	1.5722	1.5752
-1.75	-0.0049	1.5725	1.5774	-0.0010	1.5732	1.5742
-1.50	+0.0019	1.5784	1.5765	+0.0055	1.5793	1.5735
-1.25	+0.0133	1.5893	1.5760	+0.0151	1.5893	1.5742
-1.00	+0.0270	1.6030	1.5760	+0.0272	1.6010	1.5738
-0.75	+0.0421	1.6173	1.5752	+0.0389	1.6130	1.5741
-0.50	+0.0548	1.6294	1.5746	+0.0497	1.6239	1.5742
-0.25	+0.0641	1.6374	1.5723	+0.0578	1.6306	1.5722
0.00	+0.0678	1.6397	1.5719	+0.0619	1.6328	1.5709
0.25	+0.0655	1.6373	1.5718	+0.0601	1.6302	1.5701
0.50	+0.0589	1.6295	1.5706	+0.0530	1.6231	1.5701
0.75	+0.0484	1.6174	1.5690	+0.0421	1.6123	1.5702
1.00	+0.0343	1.6034	1.5691	+0.0297	1.5998	1.5701
1.25	+0.0194	1.5898	1.5704	+0.0168	1.5879	1.5711
1.50	+0.0061	1.5788	1.5727	+0.0055	1.5777	1.5722
1.75	-0.0027	1.5725	1.5752	-0.0017	1.5717	1.5734
2.00	-0.0056	1.5714	1.5770	-0.0041	1.5704	1.5745
2.25	-0.0024	1.5747	1.5771	-0.0019	1.5754	1.5773
2.44	0.0000	1.5821	1.5821	0.0000	1.5795	1.5795

TABLE 6.1 - CONCLUDED

x, in.	SPECIMEN NO. 3			SPECIMEN NO. 4		
	z _L , in.	z _u , in.	t, in.	z _L , in.	z _u , in.	t, in.
-2.42	0.0000	0.7689	0.7689	0.0000	0.7641	0.7641
-2.25	0.0011	0.7695	0.7684	-0.0012	0.7608	0.7620
-2.00	0.0040	0.7713	0.7673	-0.0041	0.7587	0.7628
-1.75	0.0105	0.7770	0.7665	-0.0016	0.7604	0.7620
-1.50	0.0201	0.7780	0.7579	+0.0043	0.7678	0.7635
-1.25	0.0327	0.8022	0.7695	+0.0137	0.7803	0.7666
-1.00	0.0456	0.8168	0.7712	+0.0260	0.7937	0.7677
-0.75	0.0576	0.8295	0.7719	+0.0393	0.8074	0.7681
-0.50	0.0678	0.8384	0.7706	+0.0512	0.8178	0.7666
-0.25	0.0756	0.8428	0.7672	+0.0606	0.8235	0.7629
0.00	0.0788	0.8441	0.7653	+0.0643	0.8266	0.7618
0.25	0.0764	0.8420	0.7656	+0.0641	0.8242	0.7601
0.50	0.0694	0.8371	0.7677	+0.0578	0.8183	0.7605
0.75	0.0591	0.8273	0.7682	+0.0500	0.8069	0.7569
1.00	0.0460	0.8136	0.7676	+0.0390	0.7921	0.7531
1.25	0.0319	0.7992	0.7673	+0.0259	0.7784	0.7525
1.50	0.0187	0.7859	0.7672	+0.0139	0.7678	0.7539
1.75	0.0081	0.7762	0.7681	+0.0051	0.7619	0.7568
2.00	0.0016	0.7719	0.7703	-0.0001	0.7608	0.7609
2.25	0.0005	0.7711	0.7706	+0.0002	0.7618	0.7620
2.42	0.0000	0.7716	0.7716	-0.0000	0.7640	0.7640

TABLE 6.2 - CONSTITUENT PROPERTIES AND CURE CYCLES FOR PREPREG TAPES

Reinforcing filament	Boron (4 mil diameter)	Boron (5.6 mil diameter)	S-glass
Resin system	SP-272	SP-296	Scotchply 1009-26S
Resin content, by weight	29 to 34 percent	33 percent	26 ± 3 percent
Resin density	0.044 lbm/in ³	0.044 lbm/in ³	0.044 lbm/in ³ *
Filament density	0.094 lbm/in ³	0.091 lbm/in ³	0.092 lbm/in ³
Cloth backing	104 glass scrim	104 glass scrim	none
Nominal ply thickness	0.0052 inch	0.0075 inch	0.0075 inch
Cure cycle	Full vacuum 30 psi pressure 85 psi pressure 1 hr at 350°F 4 hr at 350°F	Full vacuum 30 psi pressure 85 psi pressure 1 hr at 350°F 4 hr at 350°F	2 mm of Hg vacuum 2 hr at 220°F 25 psi pressure 1 hr at 300°F 4 hr at 350°F

*Typical value for epoxy resins.

TABLE 6.3 - FIBER REINFORCED SPECIMEN DIMENSIONS AND TEST RESULTS

Specimen number	Material	O.D. in.	t in.	L in.	Type test performed on specimen	E _L , ksi	G _{LT} , ksi	Max. Stress, ksi
1-1	1	0.903	0.049	2.38	C	33,474	—	297
1-2	1	0.904	0.049	2.99	C	34,198	—	277
1-3	1	0.903	0.049	3.64	C	35,798	—	283
1-4	1	0.903	0.047	5.01	T	—	1,249	9.55
1-5	1	0.903	0.048	6.00	C&T	—	1,350	—
1-6	1	0.902	0.048	6.00	C&T followed by T	—	1,274	9.56
2-1	2	0.944	0.068	2.50	C	37,247	—	322
2-2	2	0.944	0.067	2.50	C	38,080	—	319
2-3	2	0.944	0.067	2.50	C	37,536	—	302
2-4	2	0.943	0.067	5.50	T	—	1,093	9.90
3-1	3	0.939	0.065	3.00	C	9,553	—	150
3-2	3	0.939	0.067	3.00	C	9,429	—	139
3-3	3	0.942	0.066	3.01	C	9,173	—	100
3-4	3	0.943	0.066	6.01	T	—	1,401	9.59
3-5	3	0.943	0.066	6.01	C&T followed by T	—	1,430	7.63
3-6	3	0.943	0.066	6.00	C&T	—	1,480	—

Materials:

- 1 4-mil boron/epoxy - 10 ply
 2 5.6 mil boron/epoxy - 11 ply
 3 S-glass/epoxy - 10 ply

Type Test:

- C axial compression
 T torsion
 C&T combined compression and torsion

TABLE 7.1 - THEORETICAL RESULTS FOR AN EIGHT LAYER SYMMETRIC BEAM

CASE A (Free Upper and Lower Surface)

E_1, E_4, psi	10^7	10^7	10^7	10^7	10^7	10^7	10^7	10^7
E_2, E_3, psi	1	10^2	10^4	10^6	10^7	10^7	10^7	10^7
G_1, G_4, psi	3.85×10^5	3.85×10^5	3.85×10^5	3.85×10^5	3.85×10^5	3.85×10^5	3.85×10^5	3.85
G_2, G_3, psi	3.85×10^{-2}	3.85	3.85×10^2	3.85×10^4	3.85×10^5	3.85×10^5	3.85×10^5	3.85×10^5
Axial Load, lbf	800	800	801	880	1600	800	800	800
ϕ_1 , rad.	-5.54×10^{-3}	-2.54×10^{-3}	-2.49×10^{-3}	-8.95×10^{-4}	-2.52×10^{-5}	1.64×10^{-3}	1.64×10^{-3}	1.64×10^{-3}
ϕ_2 , rad.	2.23×10^{-3}	2.24×10^{-3}	2.19×10^{-3}	7.43×10^{-4}	-5.56×10^{-5}	-1.64×10^{-3}	-1.64×10^{-3}	-1.64×10^{-3}
ϕ_3 , rad.	1.88×10^{-3}	1.87×10^{-3}	1.85×10^{-3}	5.59×10^{-4}	-1.53×10^{-4}	-1.64×10^{-3}	-1.64×10^{-3}	-1.64×10^{-3}
ϕ_4 , rad.	-3.13×10^{-3}	-3.13×10^{-3}	-3.07×10^{-3}	-1.24×10^{-3}	-4.33×10^{-4}	-1.02×10^{-3}	-1.02×10^{-3}	-1.02×10^{-3}
v , in.	4.43×10^{-2}	4.43×10^{-2}	4.43×10^{-2}	4.18×10^{-2}	4.09×10^{-2}	4.28×10^{-2}	4.28×10^{-2}	4.28×10^{-2}
T_{NA}, psi	490	490	490	269	259	0	0	0
$T_{1,1}, \text{psi}$	0	0	?	97	255	0	0	0
$T_{2,2}, \text{psi}$	0	0	2	77	234	316	316	316
$T_{3,3}, \text{psi}$	0	0	2	81	174	0	0	0
$T_{4,4}, \text{psi}$	0	0	0	0	0	0	0	0
V , lbf.	26.7	26.7	26.7	28.3	50.8	26.4	26.4	26.4
$W_{CBF}, \text{in.}$	4.01×10^{-2}	4.01×10^{-2}	4.01×10^{-2}	4.01×10^{-2}	4.01×10^{-2}	4.02×10^{-2}	4.02×10^{-2}	4.02×10^{-2}

TABLE 7.1 CONCLUDED
CASE B (Restrained Upper and Lower Surface)

E_1, E_4, psi	10^7	10^7	10^7	10^7	10^7	10^7	10^2
E_2, E_3, psi	1	10^2	10^4	10^6	10^7	10^7	10^7
G_1, G_4, psi	3.85×10^5	3.85×10^5	3.85×10^5	3.85×10^5	3.85×10^5	3.85×10^5	2.85
G_2, G_3, psi	3.85×10^{-2}	3.85	3.85×10^2	3.85×10^4	3.85×10^5	3.85×10^5	3.85×10^5
Axial load, lbf	800	800	801	880	1600	800	800
ϕ_1 , rad	-1.64×10^{-3}	-1.64×10^{-3}	-1.62×10^{-3}	-6.64×10^{-4}	0	1.64×10^{-3}	1.64×10^{-3}
ϕ_2 , rad	1.64×10^{-3}	1.64×10^{-3}	1.62×10^{-3}	6.64×10^{-4}	0	-1.64×10^{-3}	-1.64×10^{-3}
ϕ_3 , rad	1.64×10^{-3}	1.64×10^{-3}	1.62×10^{-3}	6.64×10^{-4}	0	-1.64×10^{-3}	-1.64×10^{-3}
ϕ_4 , rad	-1.64×10^{-3}	-1.64×10^{-3}	-1.62×10^{-3}	-6.64×10^{-4}	0	1.64×10^{-3}	1.64×10^{-3}
v , in.	4.28×10^{-2}	4.28×10^{-2}	4.28×10^{-2}	4.14×10^{-2}	4.07×10^{-2}	4.28×10^{-2}	4.28×10^{-2}
T_{NA}, psi	316	316	313	204	203	0	0
$T_{1,1}, \text{psi}$	0	0	2	76	203	0	0
$T_{2,2}, \text{psi}$	0	0	1	63	203	316	316
$T_{3,3}, \text{psi}$	0	0	2	76	203	0	0
$T_{4,4}, \text{psi}$	316	316	313	204	203	0	0
V , lbf	26.3	26.3	26.4	28.5	50.8	26.3	26.3
W_{CBT}	4.01×10^{-2}	4.01×10^{-2}	4.01×10^{-2}	4.01×10^{-2}	4.01×10^{-2}	4.01×10^{-2}	4.02×10^{-2}

TABLE 7.2 - INFLUENCE OF LOAD INCREMENT SIZE ON RESULTS FROM THE INTERLAMINAR SHEAR STRESS COMPUTER PROGRAM

ΔP_1 , lbf.	ϕ_1 , rad.	ϕ_2 , rad.	ϕ_3 , rad.	ϕ_4 , rad.	v, in.	τ_{NA} , psi	$\tau_{1,1}$, psi	$\tau_{2,2}$, psi	$\tau_{3,3}$, psi	Q, lbf.
40.00	-8.944×10^{-4}	7.420×10^{-4}	5.589×10^{-4}	-1.235×10^{-3}	4.184×10^{-2}	269.0	96.6	76.5	81.4	28.32
20.00	-8.923×10^{-4}	7.403×10^{-4}	5.576×10^{-4}	-1.232×10^{-3}	4.184×10^{-2}	268.4	96.4	76.3	81.2	28.26
13.33	-8.917×10^{-4}	7.397×10^{-4}	5.572×10^{-4}	-1.231×10^{-3}	4.184×10^{-2}	268.2	96.3	76.2	81.1	28.23
8.00	-8.911×10^{-4}	7.393×10^{-4}	5.569×10^{-4}	-1.231×10^{-3}	4.184×10^{-2}	268.0	96.3	76.2	81.1	28.22

(a) Four layer beam

$E_1 = E_4 = 10^7$ psi

$E_2 = E_3 = 10^6$ psi

$G_1 = G_4 = 3.85 \times 10^5$ psi

$G_2 = G_3 = 3.85 \times 10^4$ psi

$h_2 = 0.125$ in.

$h_3 = 0.250$ in.

$h_4 = 0.375$ in.

$h_5 = 0.500$ in.

$b = 0.500$ in.

$a_0 = 0.020$ in.

$L = 4.00$ in.

TABLE 1.3 - INFLUENCE OF BOUNDARY CONDITIONS ON DISPLACEMENT, ROTATIONS AND INTERLAMINAR SHEAR STRESS

Boundary Condition	Case A (a)	Case B (b)	Case A	Case B	Case A	Case B
E_f , psi	10^7	10^7	10^7	10^7	10^7	10^7
E_m , psi	10^5	10^5	10^6	10^6	10^7	10^7
G_f , psi	$3.846(10^6)$	$3.846(10^6)$	$3.846(10^6)$	$3.846(10^6)$	$3.846(10^6)$	$3.846(10^6)$
G_m , psi	$3.846(10^4)$	$3.846(10^4)$	$3.846(10^5)$	$3.846(10^5)$	$3.846(10^6)$	$3.846(10^6)$
ϕ_f , rad.	$-9.901(10^{-3})$	$-8.500(10^{-3})$	$-1.160(10^{-3})$	$-8.234(10^{-4})$	$-1.693(10^{-4})$	0
ϕ_m , rad.	$9.897(10^{-3})$	$8.500(10^{-3})$	$1.001(10^{-3})$	$8.234(10^{-4})$	$1.703(10^{-4})$	0
w_1 , in.	$5.294(10^{-2})$	$5.111(10^{-2})$	$4.179(10^{-2})$	$4.129(10^{-2})$	$4.081(10^{-2})$	$4.041(10^{-2})$
τ , psi	772	663	926	706	1793	1261

(a) 19 ply laminate (10 fiber and 9 matrix laminae)

(b) 4 ply laminate (2 fiber and 2 matrix laminae)

TABLE 7.4 - LAMINATE SPECIMEN TEST RESULTS

Specimen number	Failure load, lb_f	a_0 , in.
1	6100	.0349
2	7000	.0311
3	2340	.0402
4	3590	.0336

TABLE 7.5 - COMPARISON OF THEORY WITH LAMINATE SPECIMEN TEST RESULTS

Specimen number	a ₀ ' in.	Failure load lbf	Deflection, in.						τ _{1,1} psi	τ _{8,8} psi	τ _{9,9} psi	Bond strength psi
			x = L/4		x = L/2		x = 3L/4					
			Theory	Exp	Theory	Exp	Theory	Exp				
1	.0349	6100	.0026	.0025	.0052	.0044	.0026	.0023	396	337	334	290
2	.0311	7000	.0027	----- ^a	.0054	----- ^a	.0027	----- ^a	396	349	346	290
3	.0402	2340	.0028	.0042	.0057	.0066	.0028	.0047	414	264	281	290
4	.0036	3590	.0041	.0055	.0079	.0090	.0041	.0053	509	373	369	290

^a Reliable deflection data was not obtained on specimen 2.

TABLE 7.6.- EFFECT OF AXIAL COMPRESSIVE STRESS AND FIBER CURVATURE ON SHEAR MODULUS.

a_o in.	a_o/t	a_o/L	σ_c ksi	τ_{max} psi	τ_{ave} psi	G_m ksi	G_{LT} ksi	G^* ksi
.0005	.2	.000625	156	709	451	592	1220	1064
.0005	.2	.000625	312	1669	1063	592	1220	908
.0005	.2	.000625	468	2379	1515	592	1220	752
.0010	.4	.001250	156	1418	903	592	1220	1064
.0010	.4	.001250	312	2905	1849	592	1220	908
.0010	.4	.001250	468	4626	2946	592	1220	752
.0015	.6	.001875	156	2127	1354	592	1220	1064
.0015	.6	.001875	234	3132	1994	592	1220	986
.0015	.6	.001875	312	4228	2691	592	1220	908
.0015	.6	.001875	390	5415	3447	465	960	570
.0015	.6	.001875	468	6693	4261	394	814	346
.0030	1.2	.003750	156	3879	2469	592	1220	1064
.0030	1.2	.003750	312	8086	5148	333	689	377
.0030	1.2	.003750	468	13345	8495	139	289	-179 ^a

(a) Shear instability is predicted to occur at $G^* = 0$, therefore negative values have no significance.

TABLE C.1 - FIBER COORDINATES

Spec. no.	Fiber			1		2		3		4		5	
	t, in.	z, in.	x, in.	y, in.	x, in.	y, in.	x, in.	y, in.	x, in.	y, in.	x, in.	y, in.	x, in.
1	.1526	0	.04336	.01423	.0404	.0086	.1916	.0382	.4040	.0314	.3024	.0406	
2	.1010	.2226	.04332	.01347	.0408	.0085	.1908	.0374	.4030	.0306	.3012	.0401	
3	.0985	.3936	.04332	.01323	.0408	.0080	.1896	.0374	.4031	.0311	.3010	.0402	
4	.0995	.5621	.04417	.01314	.0419	.0086	.1891	.0380	.4031	.0312	.3005	.0406	
5	.1010	.7314	.04489	.01333	.0428	.0085	.1889	.0377	.4035	.0310	.3006	.0400	
6	.1005	.9026	.04574	.01385	.0446	.0085	.1879	.0378	.4033	.0314	.2994	.0410	
7	.0121	1.0731	.04670	.01342	.0447	.0083	.1880	.0381	.4037	.0311	.2986	.0414	
8	.1025	1.2452	.04746	.01357	.0465	.0082	.1877	.0380	.4038	.0313	.2975	.0404	
9	.1083	1.4177	.04836	.01399	.0479	.0086	.1863	.0381	.4045	.0315	.2969	.0406	
10	.1002	1.5960	.04922	.01414	.0484	.0086	.1864	.0390	.4059	.0315	.2975	.0403	
11	.1020	1.7662	.05003	.01347	.0497	.0084	.1862	.0389	.4066	.0314	.2977	.0399	
12	.0988	1.9382	.05088	.01347	.0511	.0085	.1859	.0380	.4066	.0311	.2973	.0403	
13	.1002	2.1070	.05150	.01342	.0511	.0082	.1847	.0392	.4057	.0312	.2963	.0409	
14	.1004	2.2772	.05250	.01338	.0525	.0078	.1851	.0392	.4067	.0315	.2963	.0408	
15	.0995	2.4476	.05312	.01330	.0527	.0080	.1842	.0393	.4069	.0314	.2952	.0409	
16	.1028	2.6178	.05322	.01347	.0533	.0081	.1835	.0395	.4073	.0312	.2948	.0403	
17	.1005	2.7899	.05374	.01299	.0534	.0080	.1826	.0343	.4068	.0315	.2936	.0409	
18	.1000	2.9604	.05388	.01342	.0541	.0083	.1819	.0397	.4068	.0319	.2925	.0402	
19	.1010	3.1304	.05431	.01342	.0542	.0080	.1818	.0390	.4078	.0315	.2921	.0404	
20	.1003	3.3024	.05431	.01299	.0534	.0079	.1800	.0391	.4071	.0310	.2903	.0407	
21	.1009	3.4717	.05474	.01323	.0544	.0081	.1795	.0395	.4078	.0312	.2898	.0408	
22	.1013	3.6426	.05569	.01428	.0555	.0091	.1779	.0421	.4077	.0329	.2882	.0421	

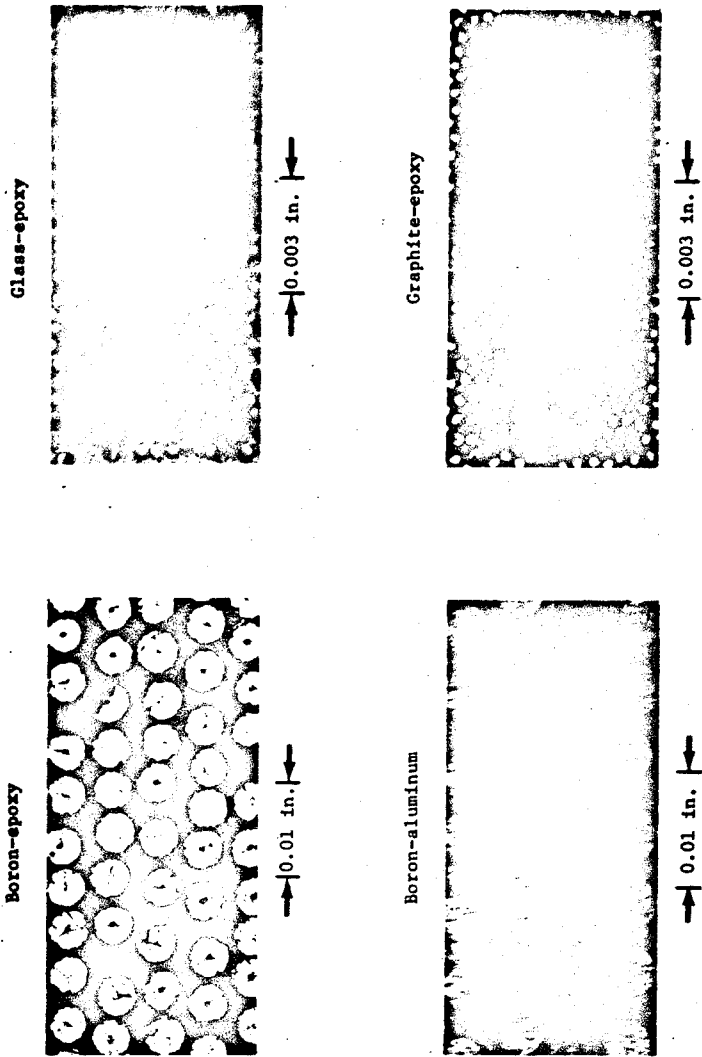


Figure 1.1 - Photomicrographs of composite materials.

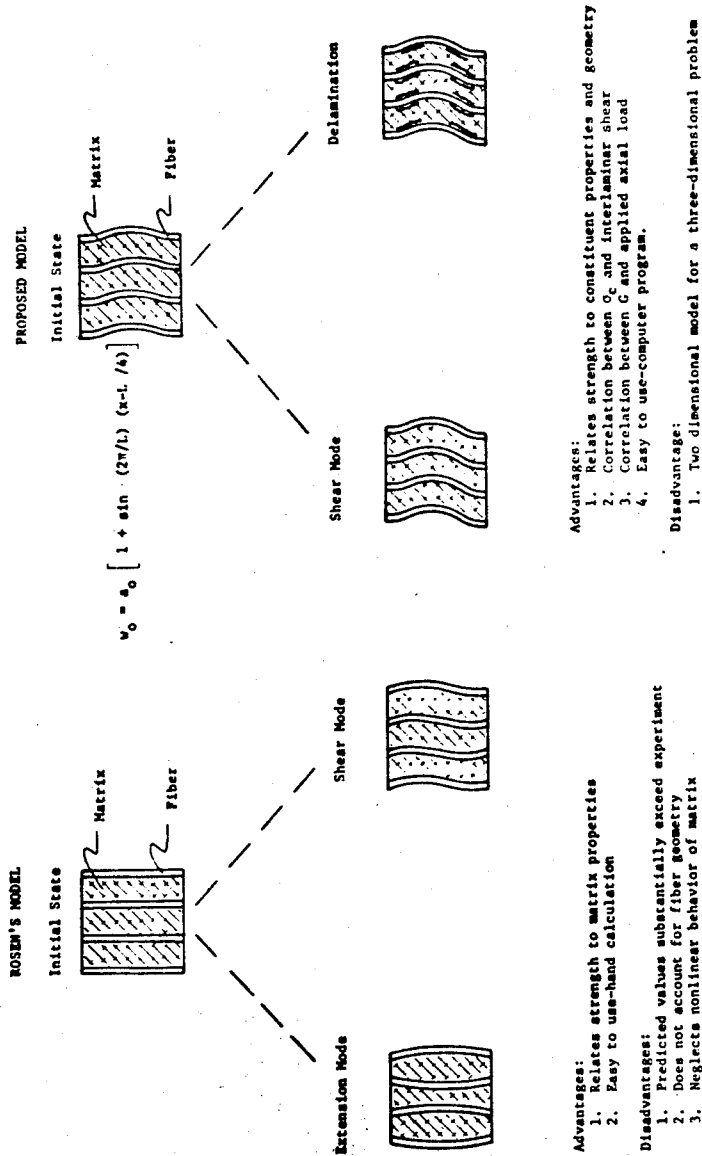
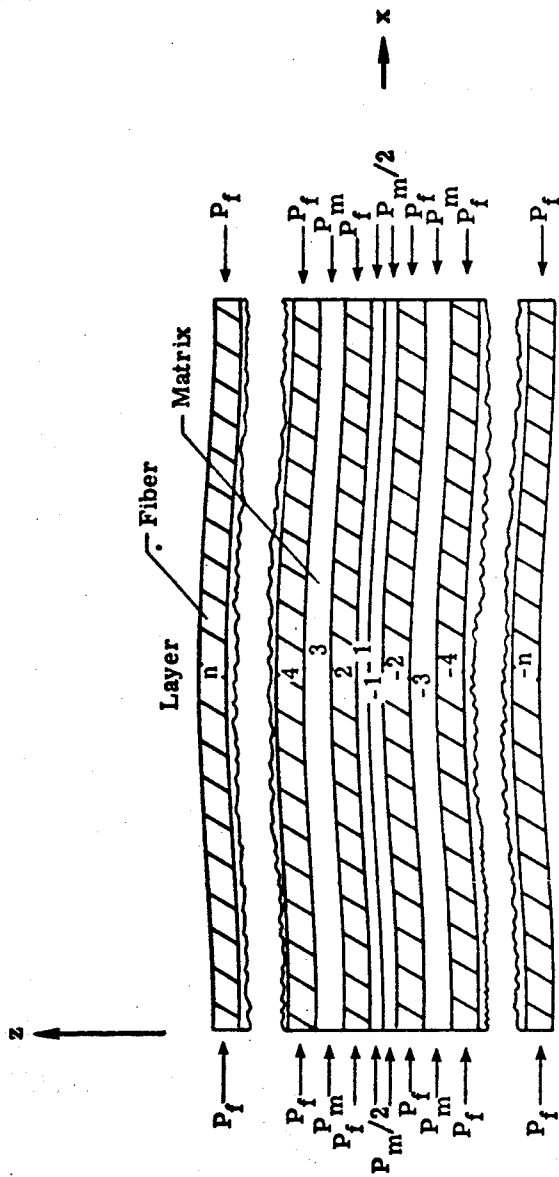
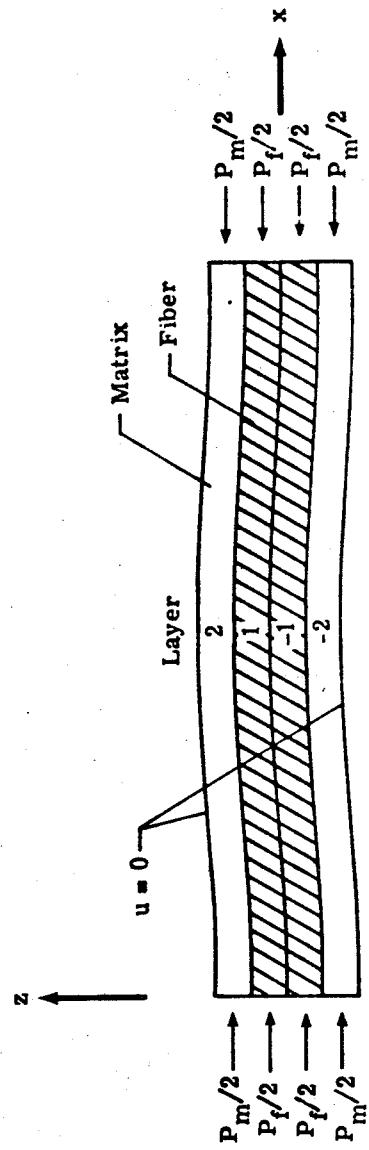


Figure 3.1 - Analytical models of composite material.



a. Case A

Figure 4.1 - Laminated beam model of composite material.



b. Case B

Figure 4.1 - Concluded.

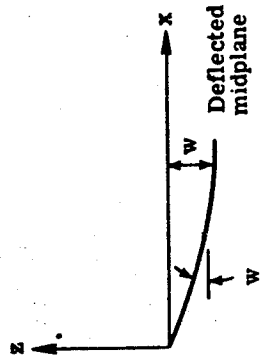
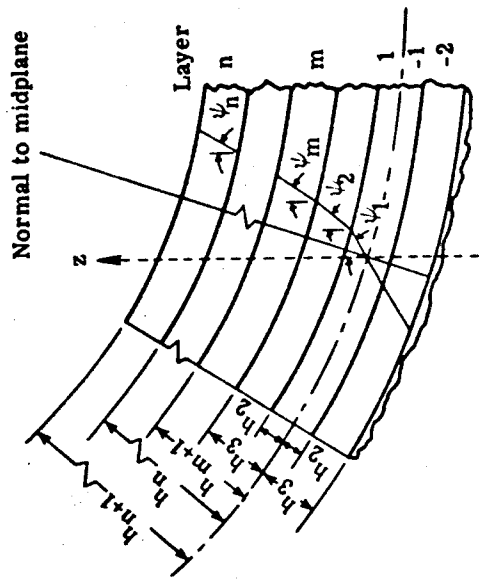
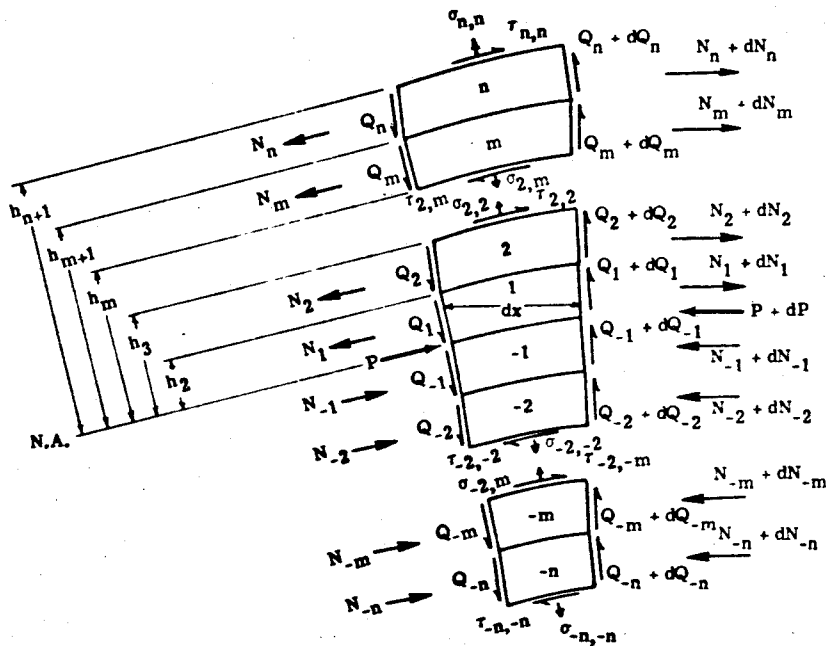
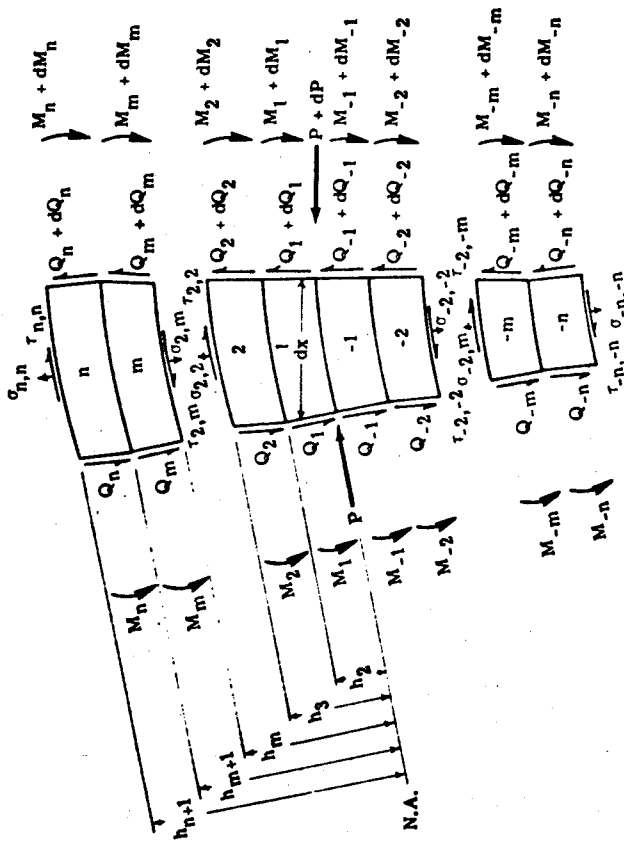


Figure 4.2 - Notation for multilayered beam.



(a) Diagram for summing forces

Figure 4.3 - Equilibrium of beam element.



(b) Diagram for summing moments

Figure 4.3 - Concluded.

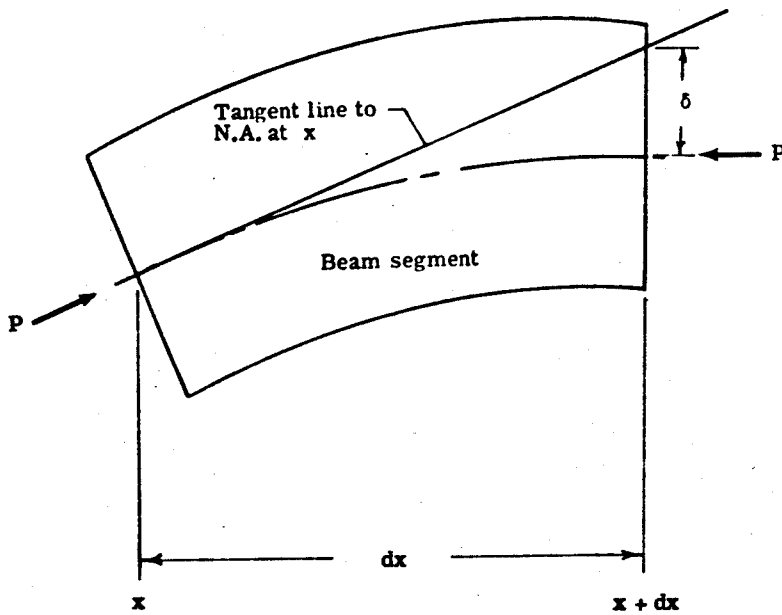


Figure 4.4 - Moment arm (δ) for axial force.

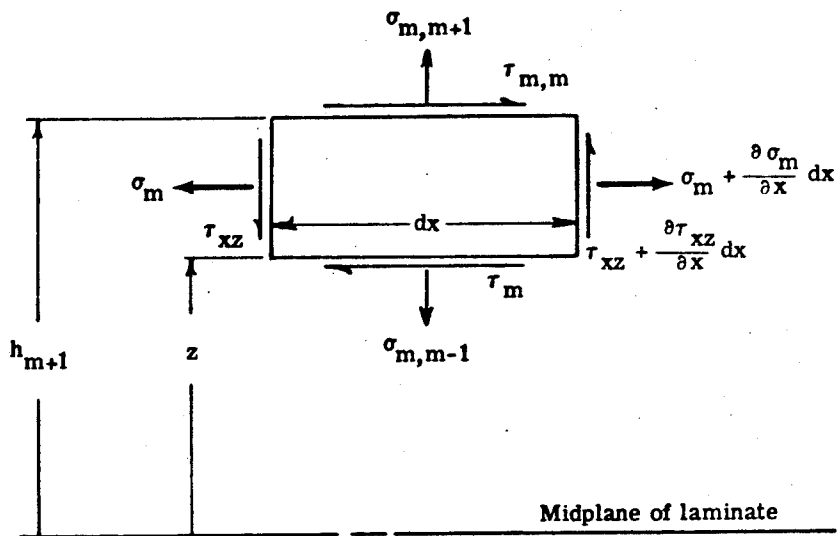
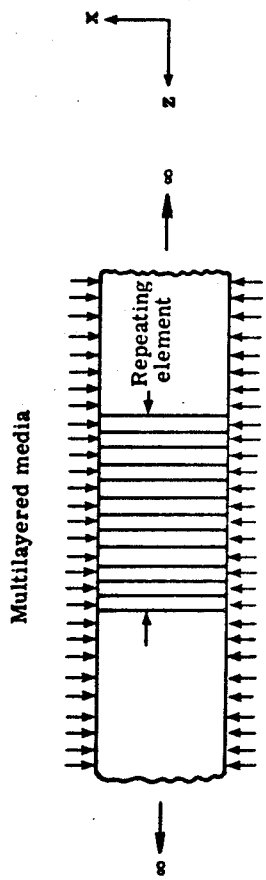
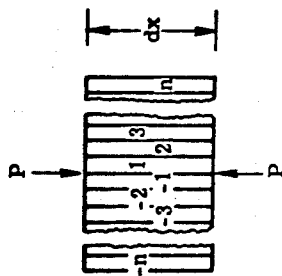


Figure 4.5 - Free body diagram of an element from the m^{th} layer in a multilayered beam.



Initial position of repeating element



Buckled position of repeating element

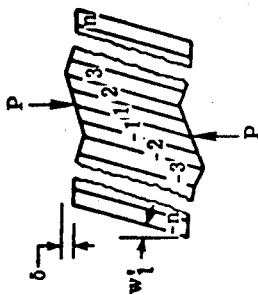


Figure 5.1 - Shear buckling of multilayered media.

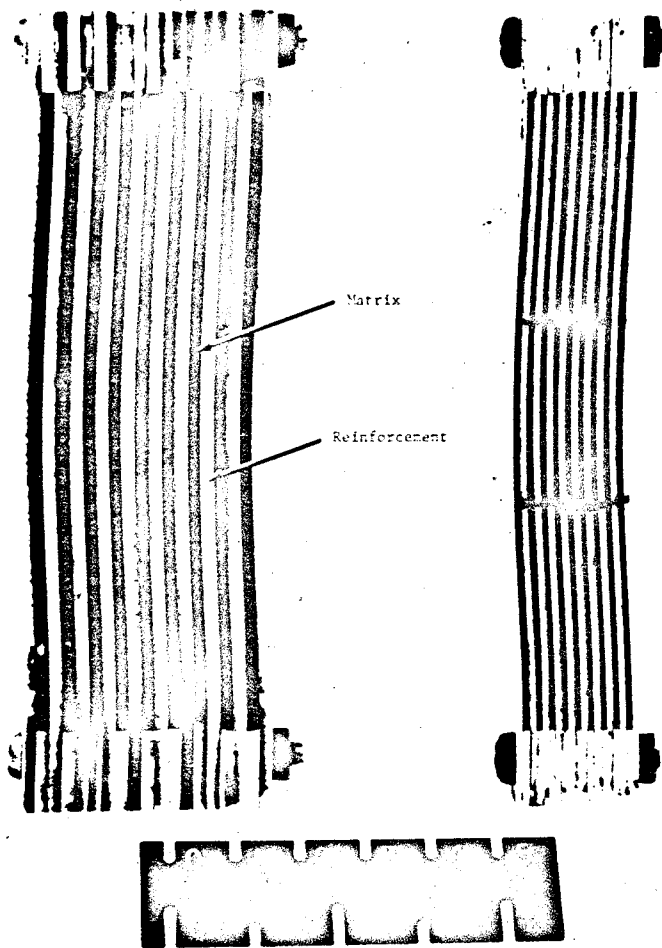


Figure 6.1 - Front view of lamina reinforced test specimens.

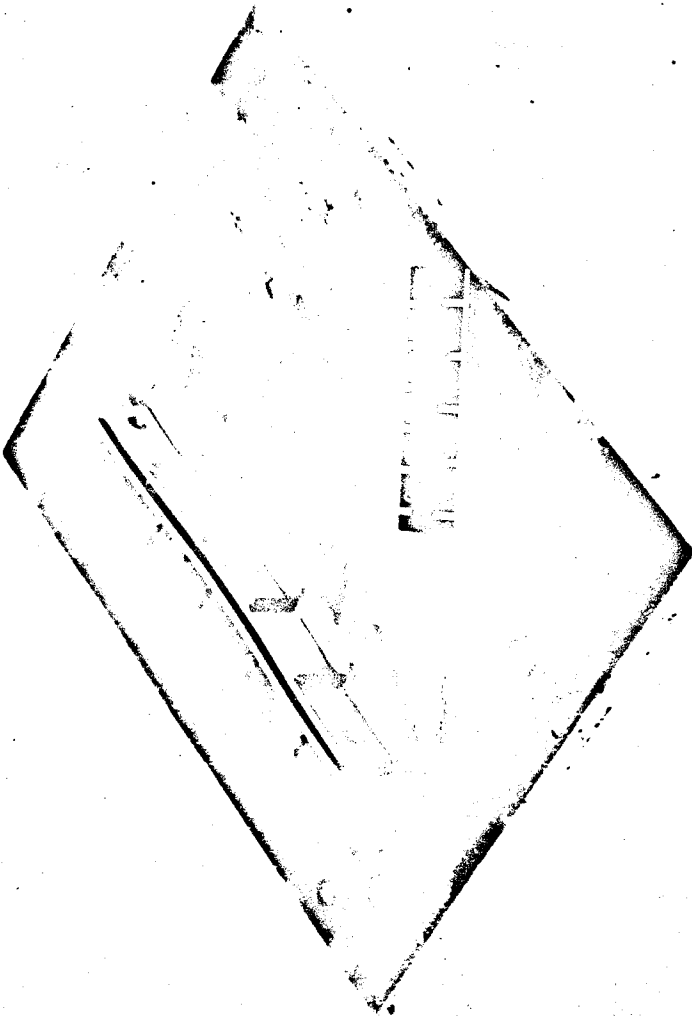


Figure 6.2 - Alignment plate for fabricating lamina reinforced specimens.

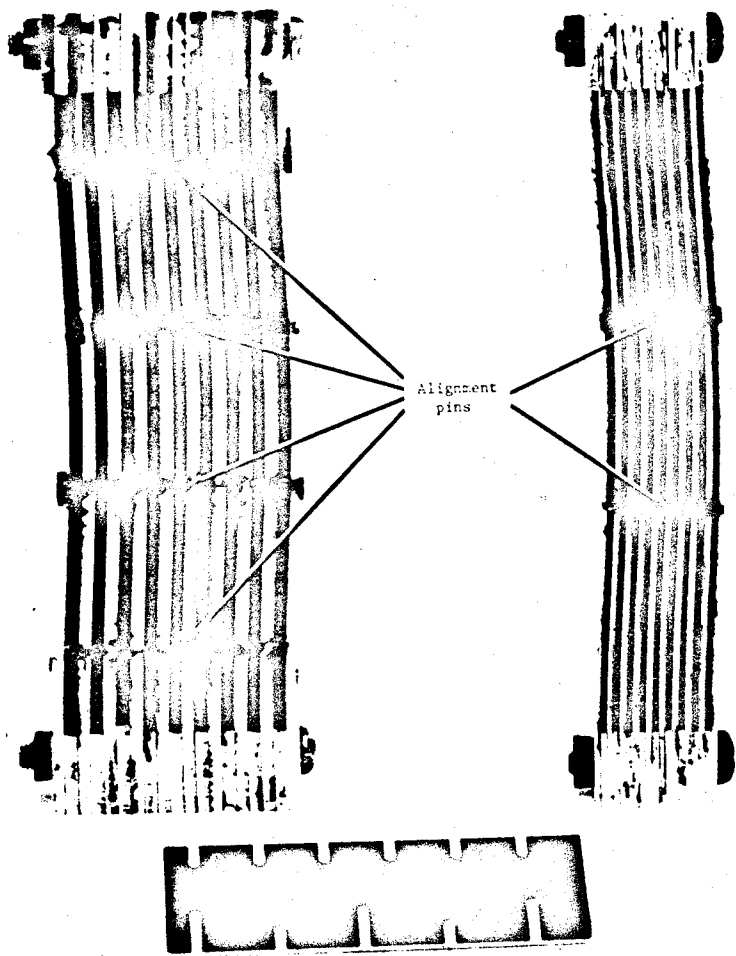


Figure 6.3 - Rear view of lamina reinforced test specimens.

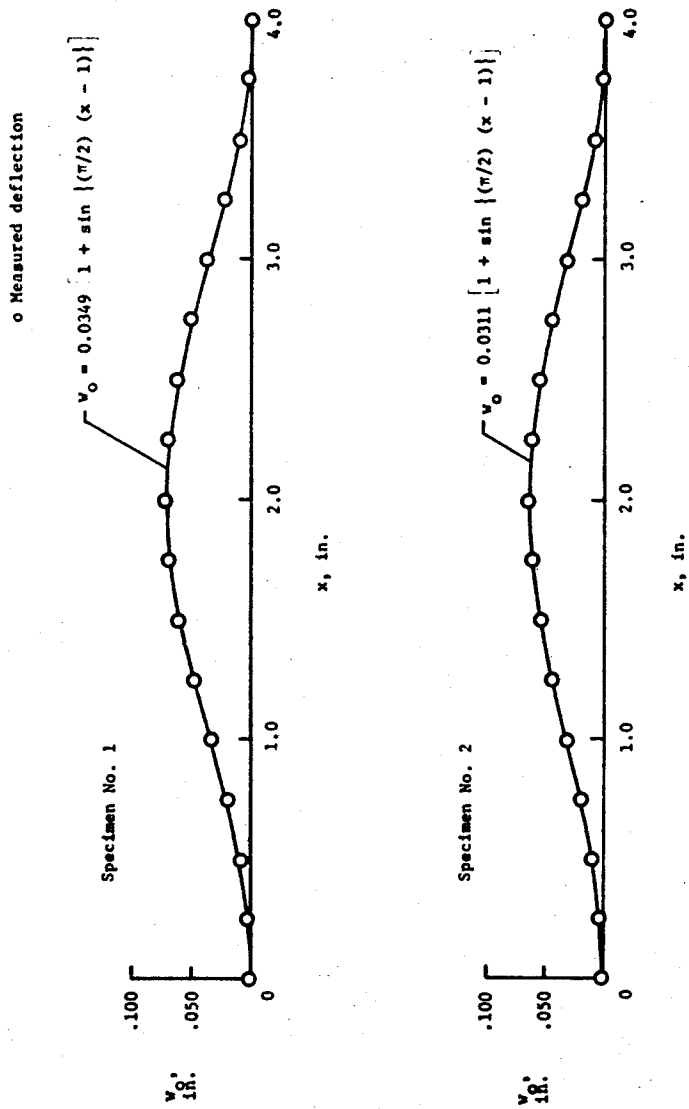


Figure 6.4 - Initial transverse displacement for lamina reinforced specimens.

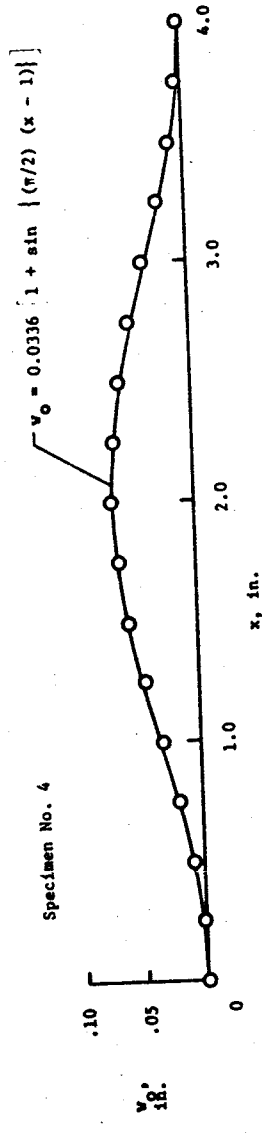
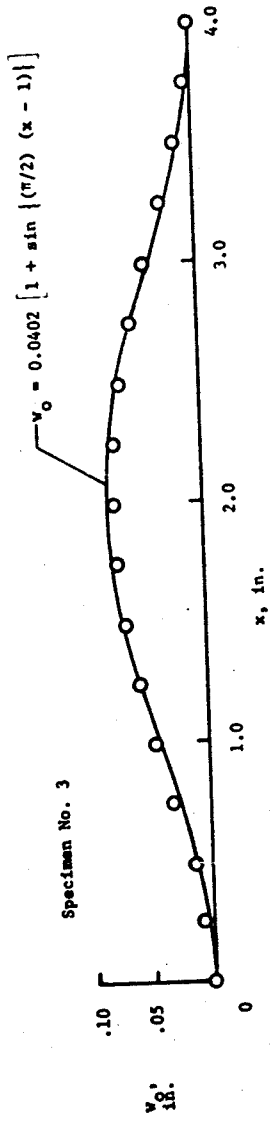


Figure 6.4 - Concluded.

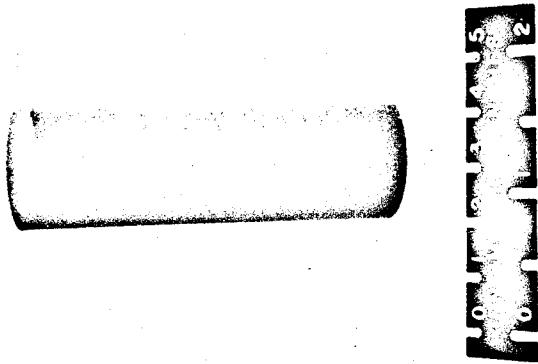


Figure 6.5 - Matrix compression test specimen.

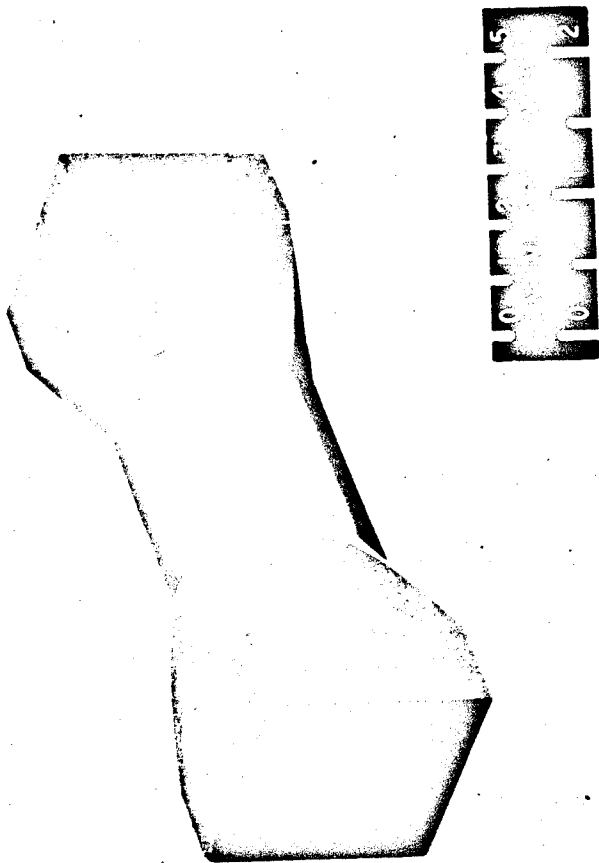


Figure 6.6 - Matrix shear test specimen.

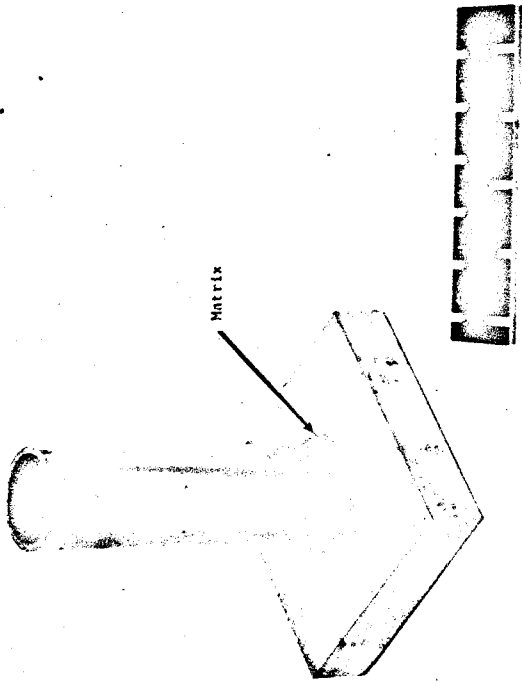


Figure 6.7 - Matrix-reinforcement bond strength specimen.

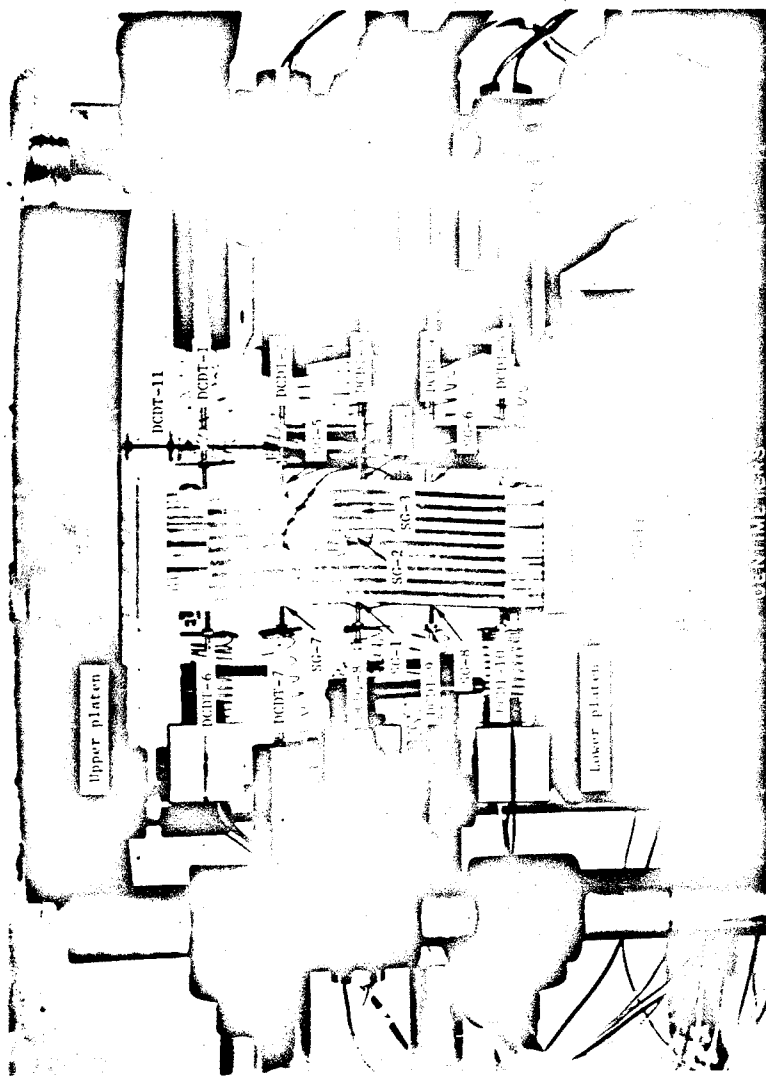


Figure 6.8 - Compression test of a lamina reinforced specimen.

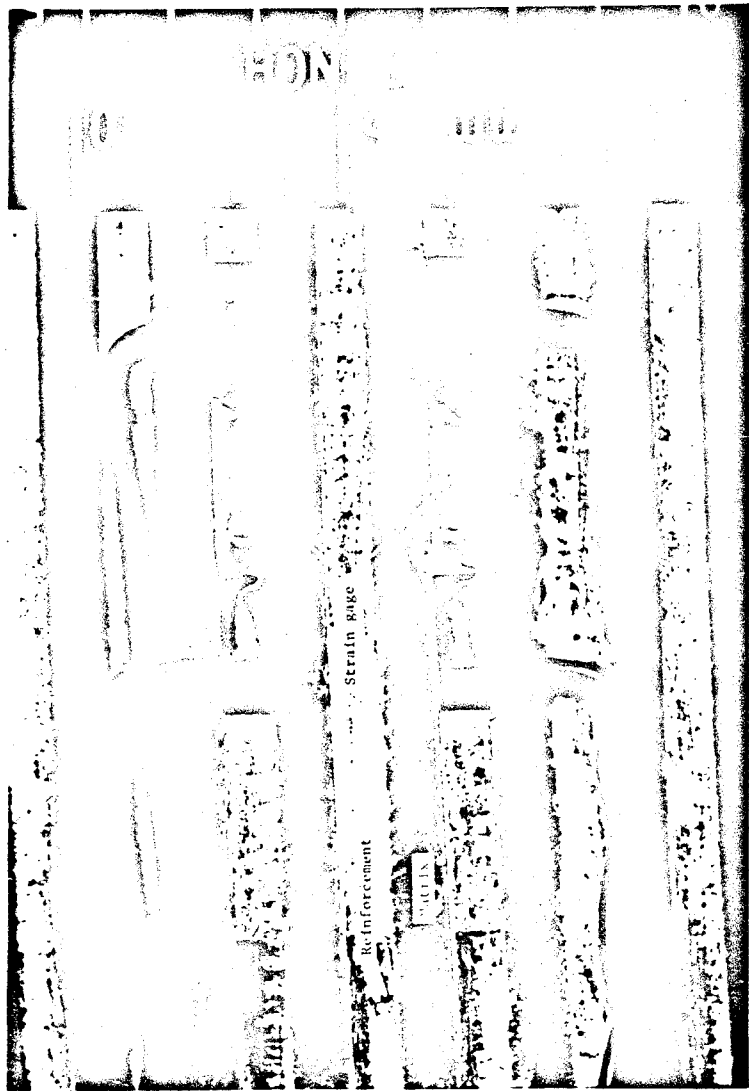


Figure 6.9 - Close-up view of a strain gage mounted on the edge of a reinforcing lamina.

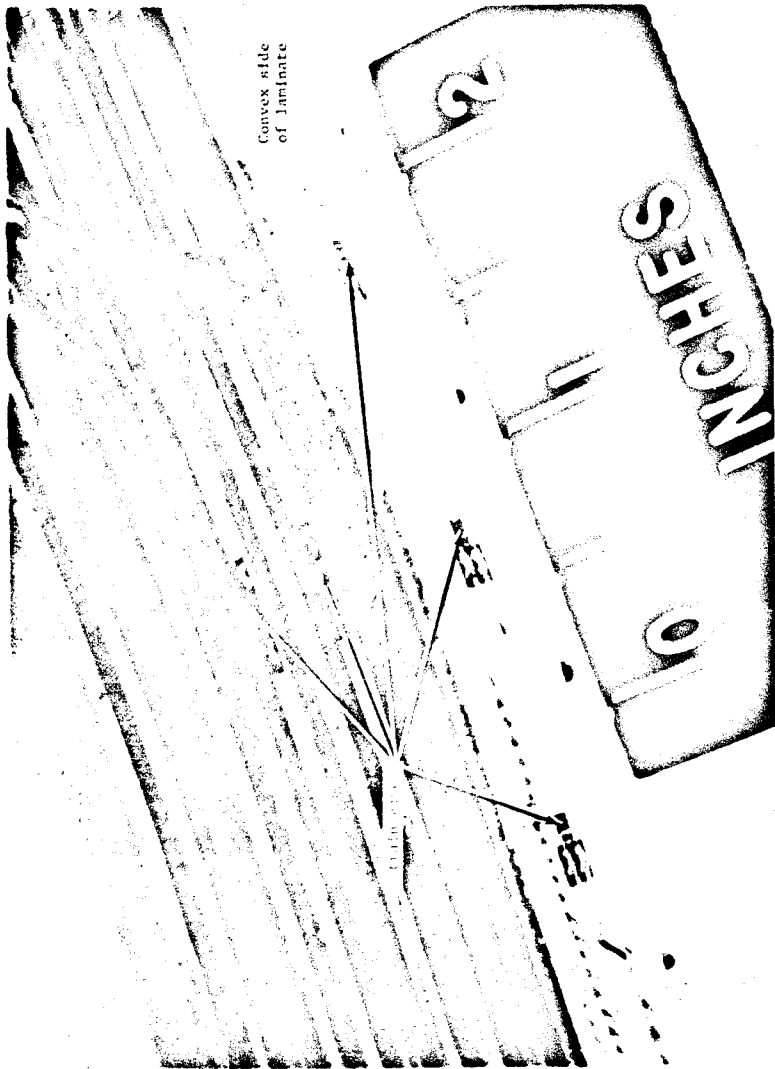


Figure 6.10 - Strain gages on lamina reinforced specimen.

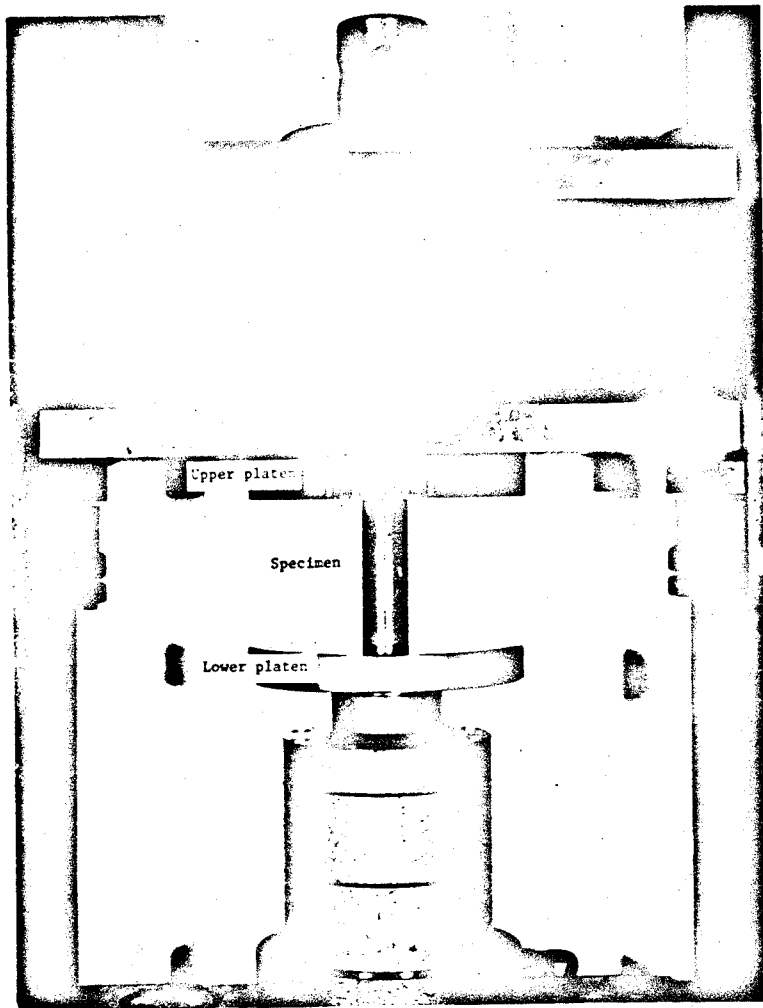


Figure 6.11 - Compression test of a matrix specimen.

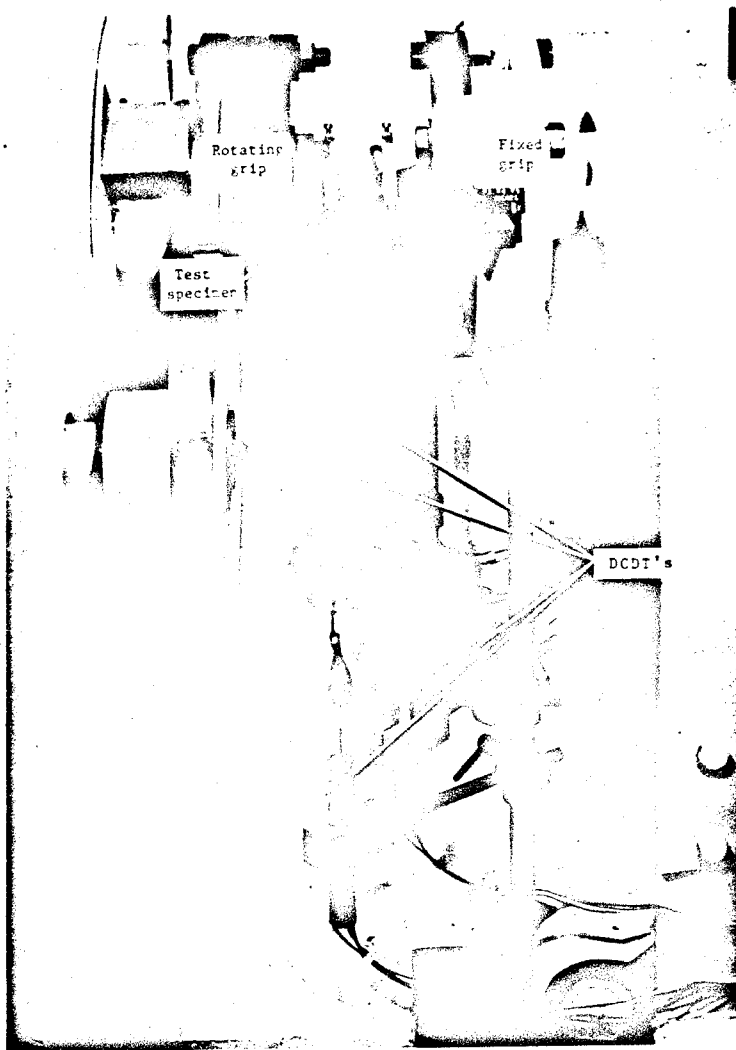


Figure 6.12 - Torsion test of a matrix specimen.

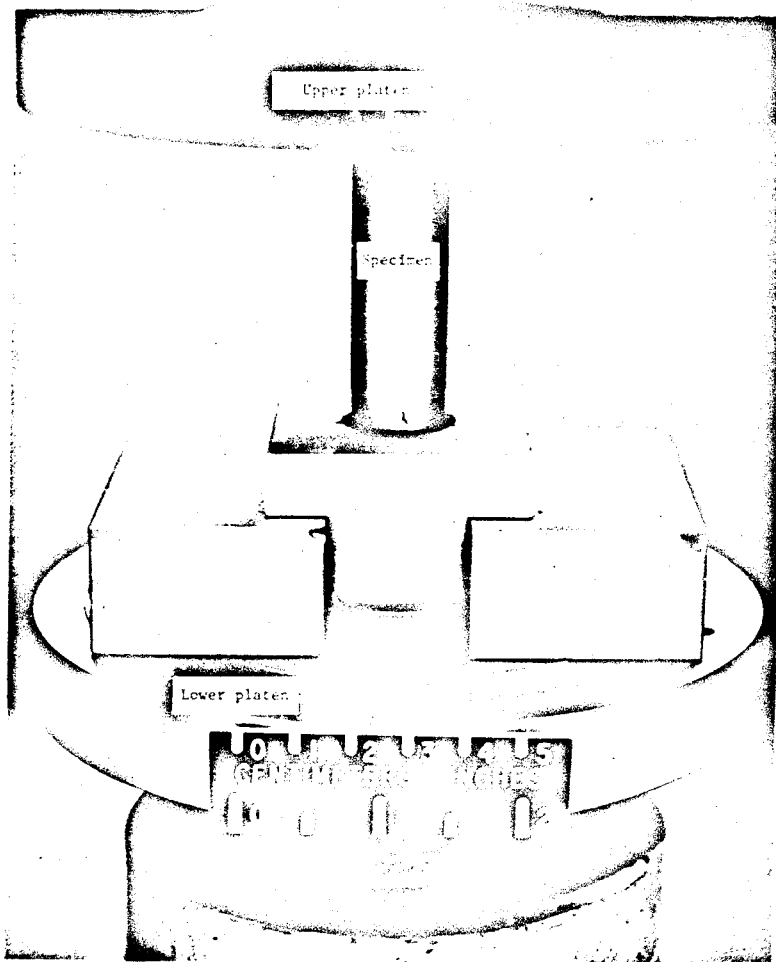


Figure 6.13 - Bond strength test setup.

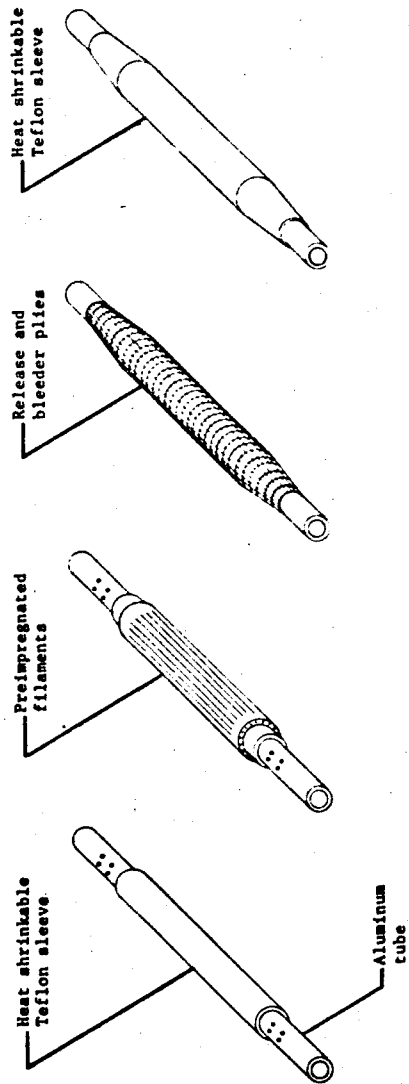
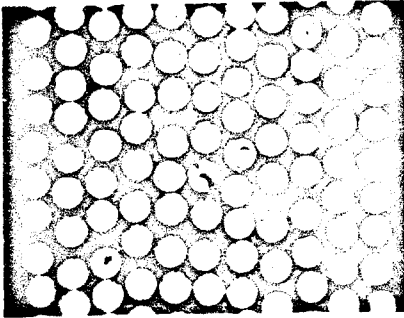


Figure 6.14 - Flow diagram of process for fabricating uniaxial filament-reinforced epoxy tubes.



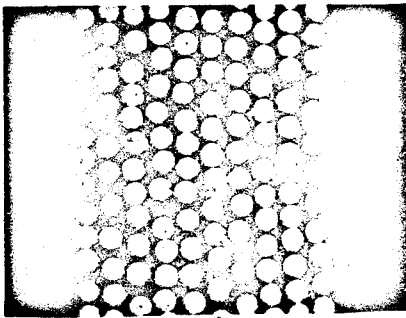
0.004 in.

S-glass-epoxy



0.02 in.

Boron-epoxy
(5.6 mil dia. fiber)



0.02 in.

Boron-epoxy
(4 mil dia. fiber)

Figure 6.15 - Photomicrographs of tube cross sections.

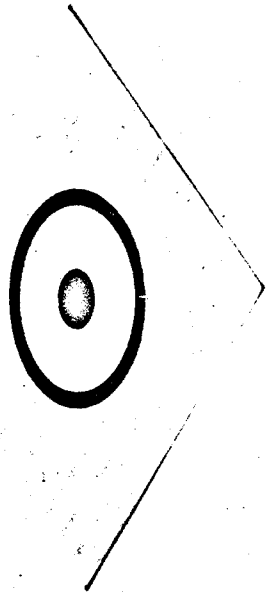


Figure 6.16 - End plug.

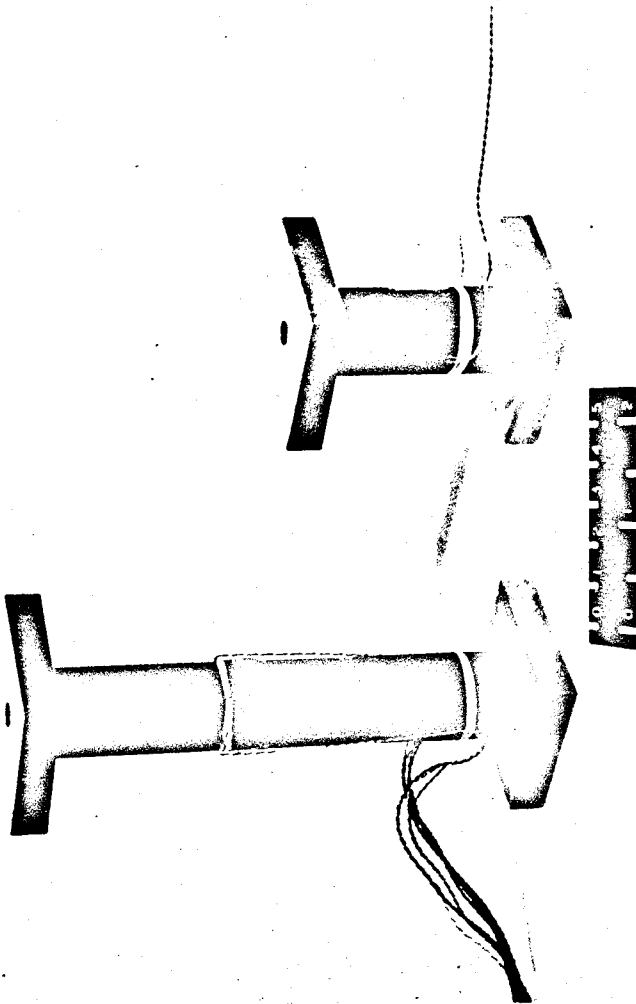


Figure 6.17 - Boron-epoxy tubular specimens.

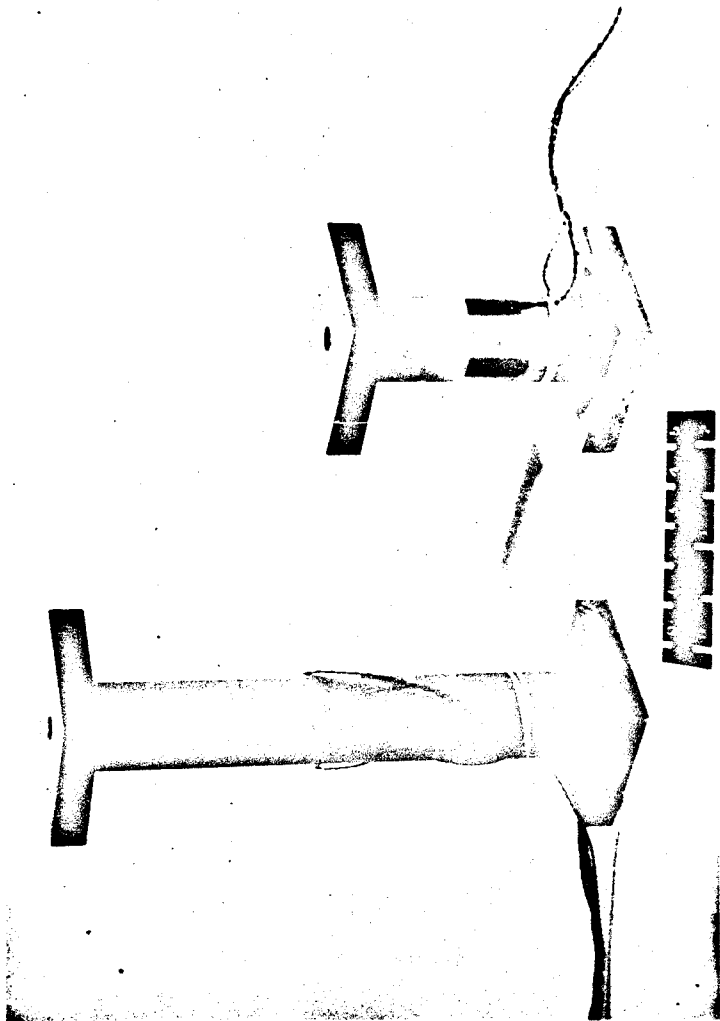


Figure 6.18 - S-glass-epoxy tubular specimens.

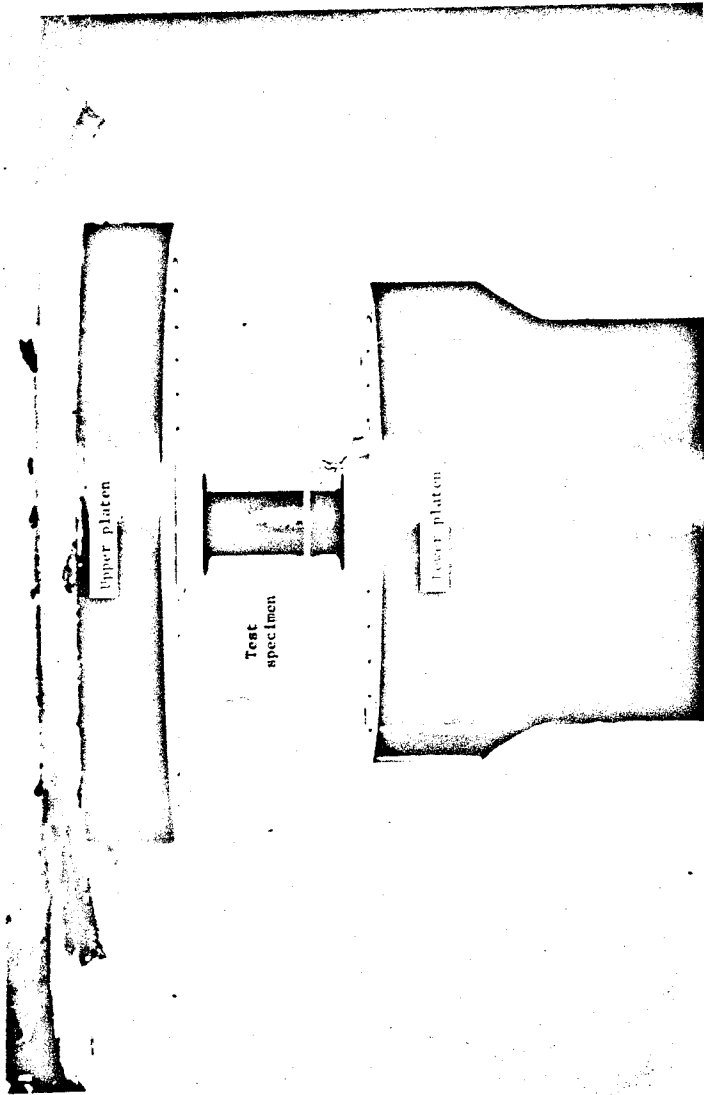


Figure 6.19 - Compression test of a boron-epoxy tubular specimen.

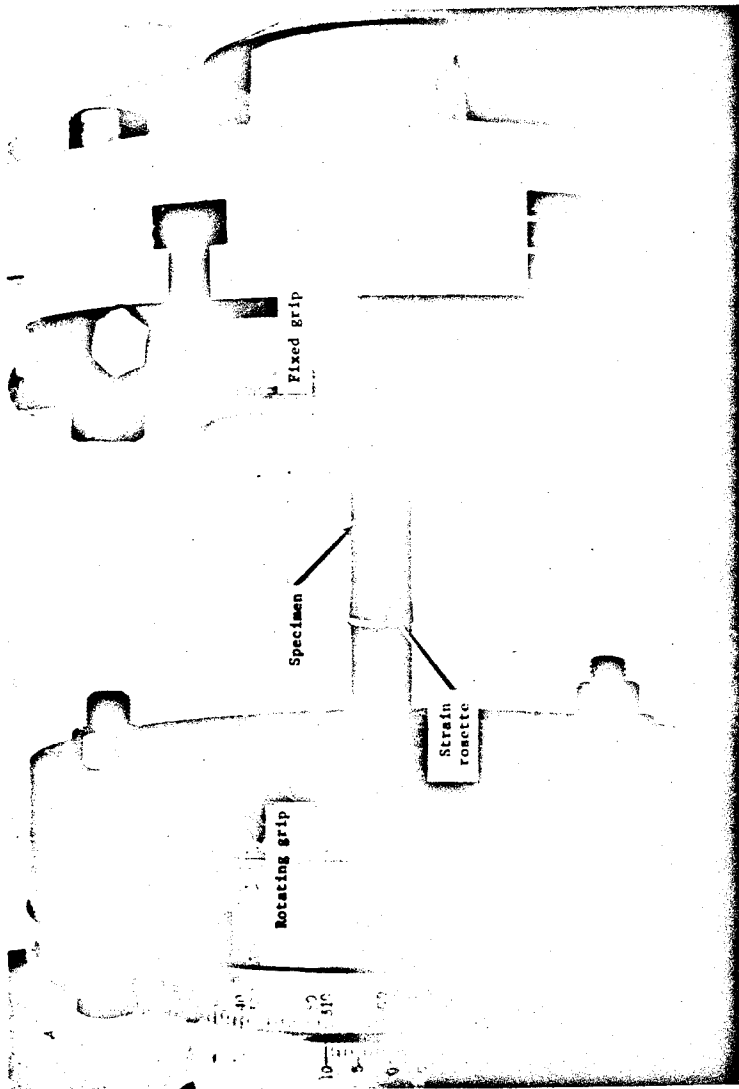


Figure 6.20 - Torsion test of a boron-epoxy tubular specimen.

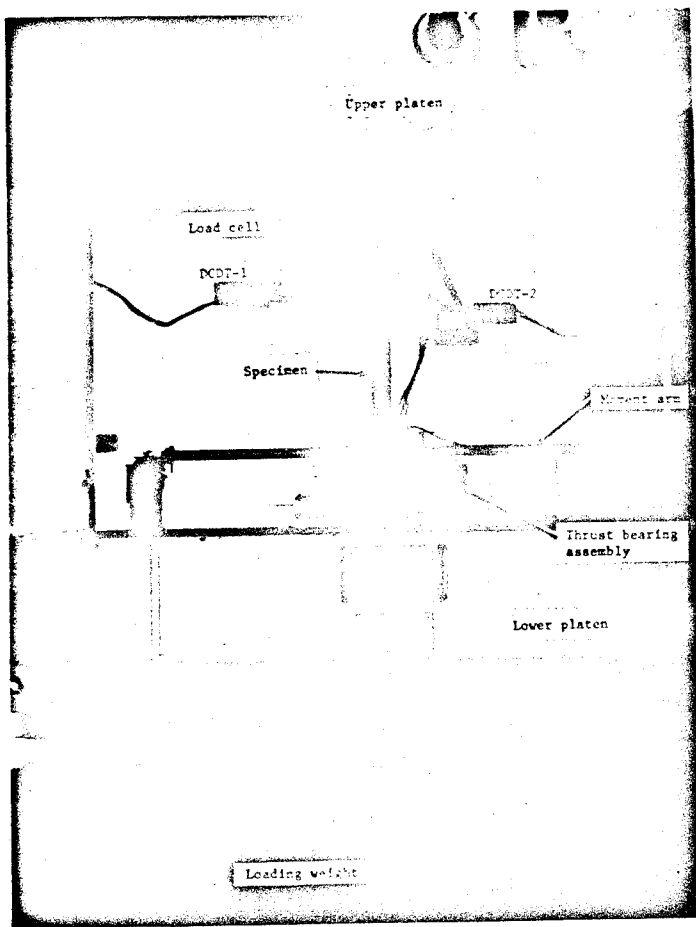


Figure 6.21 - Combined compression and torsion test of a boron-epoxy tubular specimen.

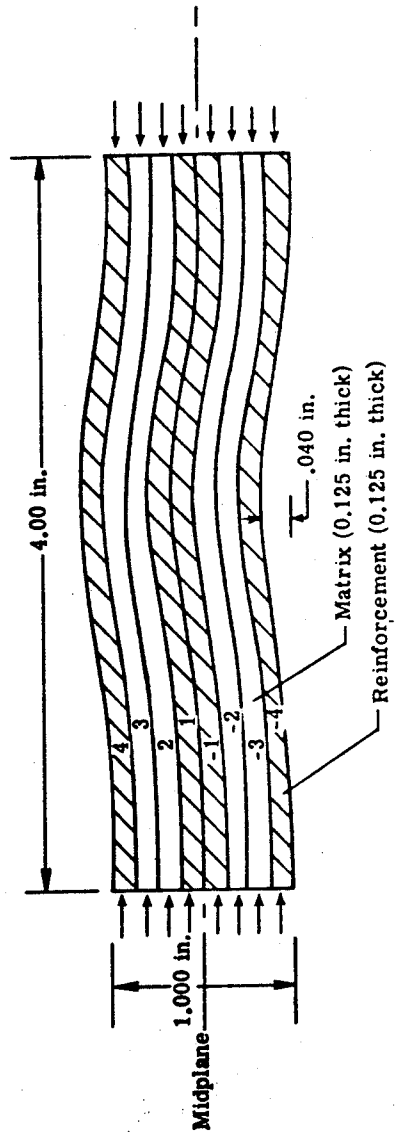


Figure 7.1 - Multilayered beam utilized to generate theoretical results.

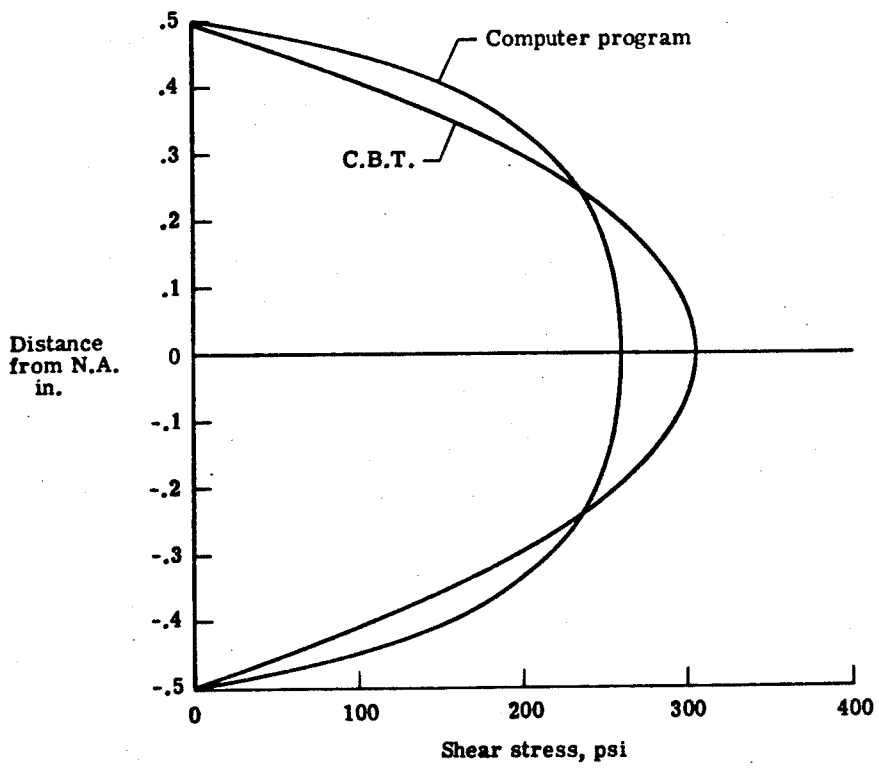


Figure 7.2 - Shear stress distribution at $x = L/4$.

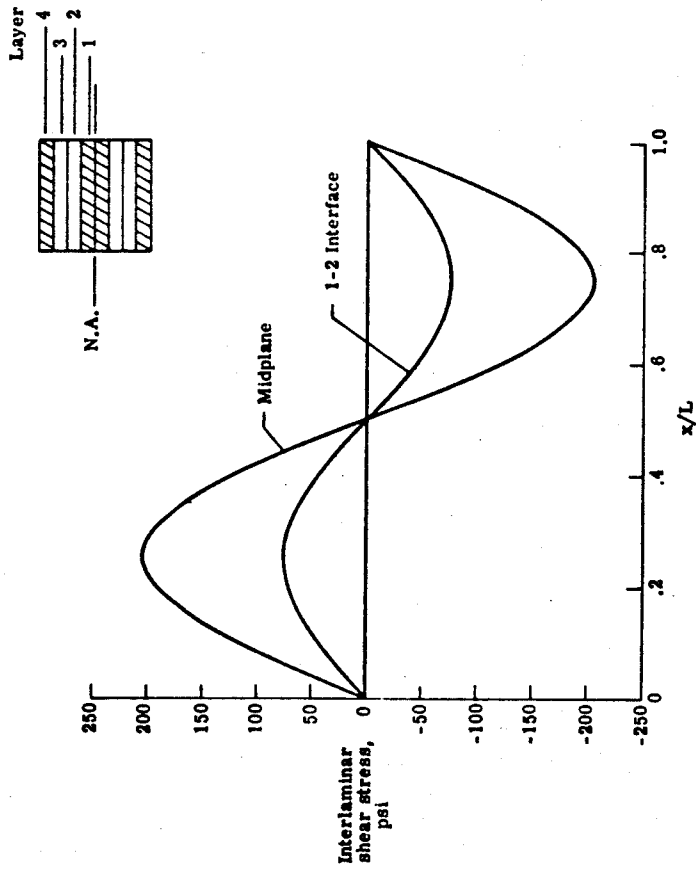


Figure 7.3 - Interlaminar shear stress based on linear stress-strain behavior.

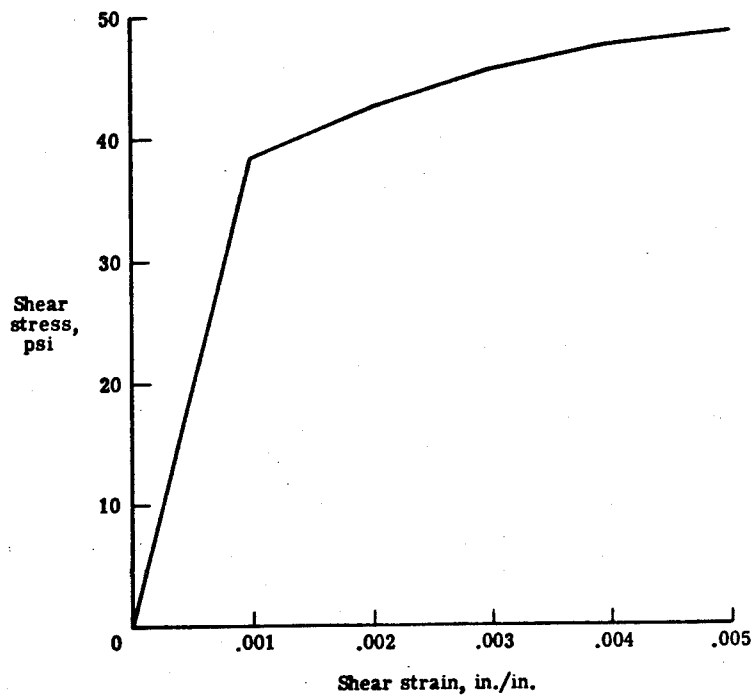


Figure 7.4 - Nonlinear shear stress-strain curve used to generate theoretical results.

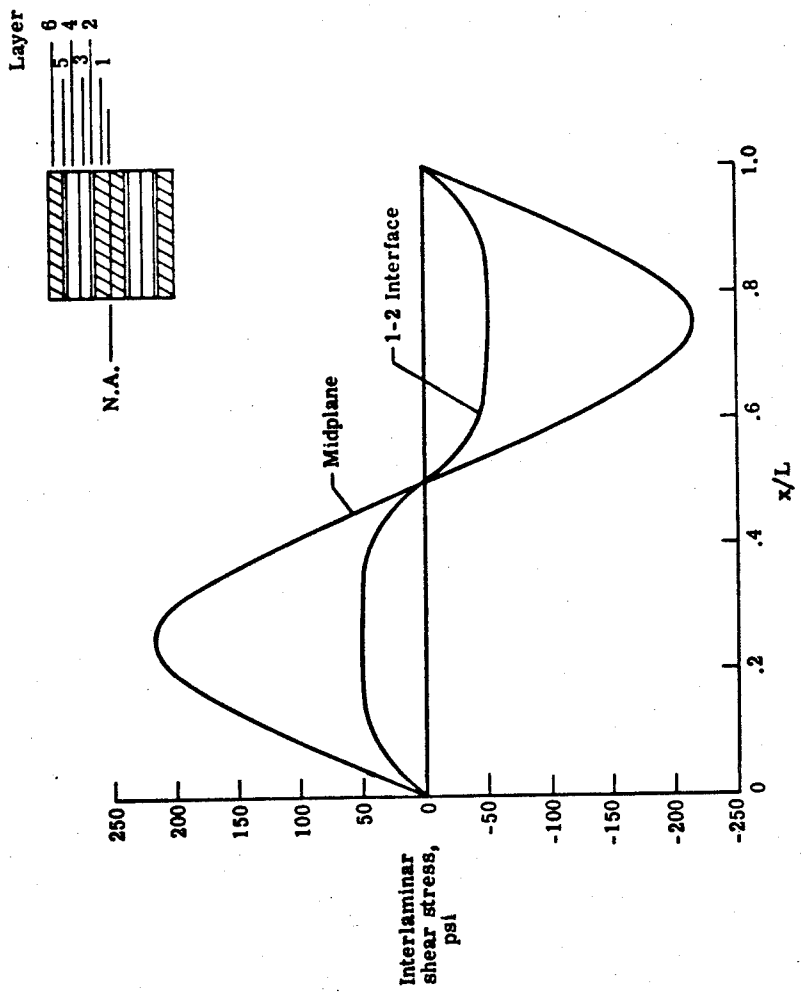


Figure 7.5 - Effect of nonlinear stress-strain behavior on interlaminar shear.

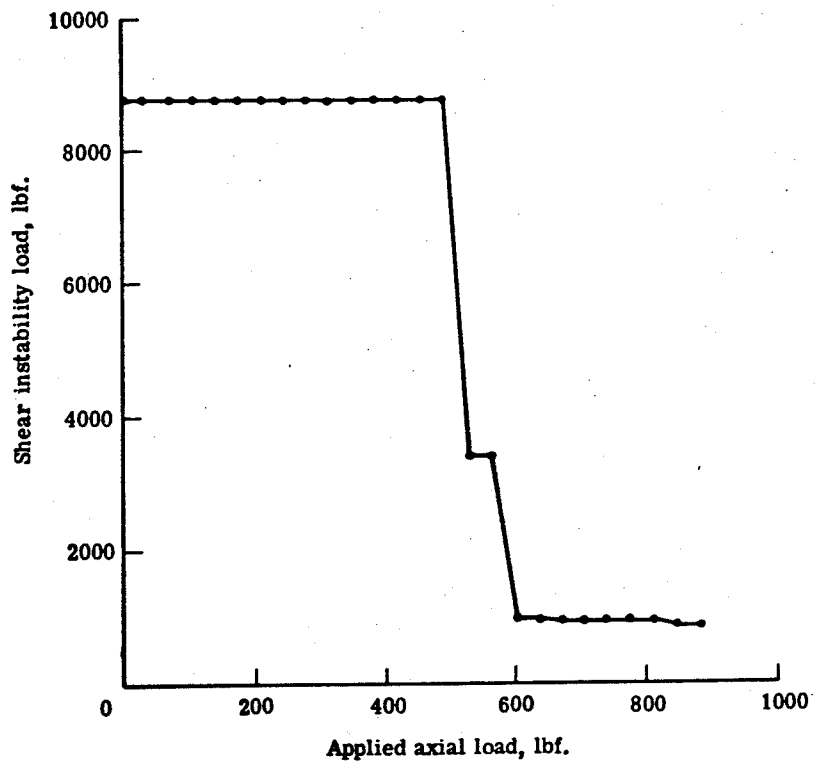


Figure 7.6 - Effect of nonlinear stress-strain behavior on shear instability load.

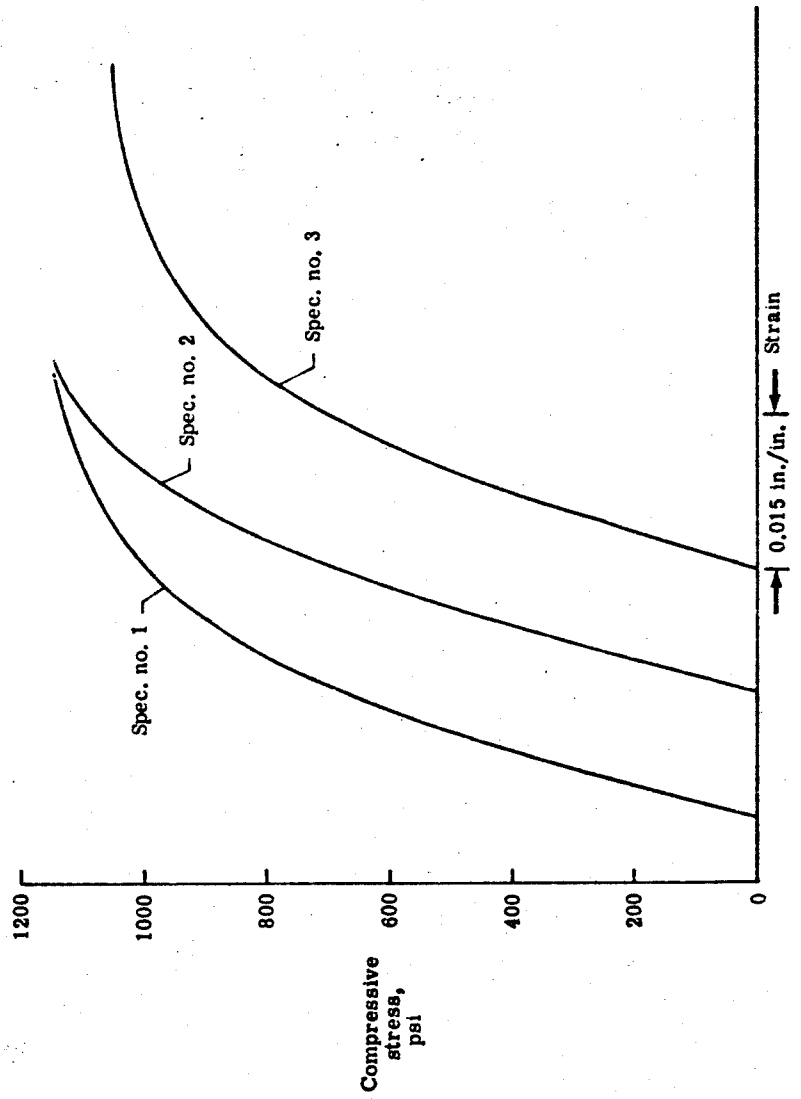


Figure 7.7 - Compressive stress-strain curves for matrix material.

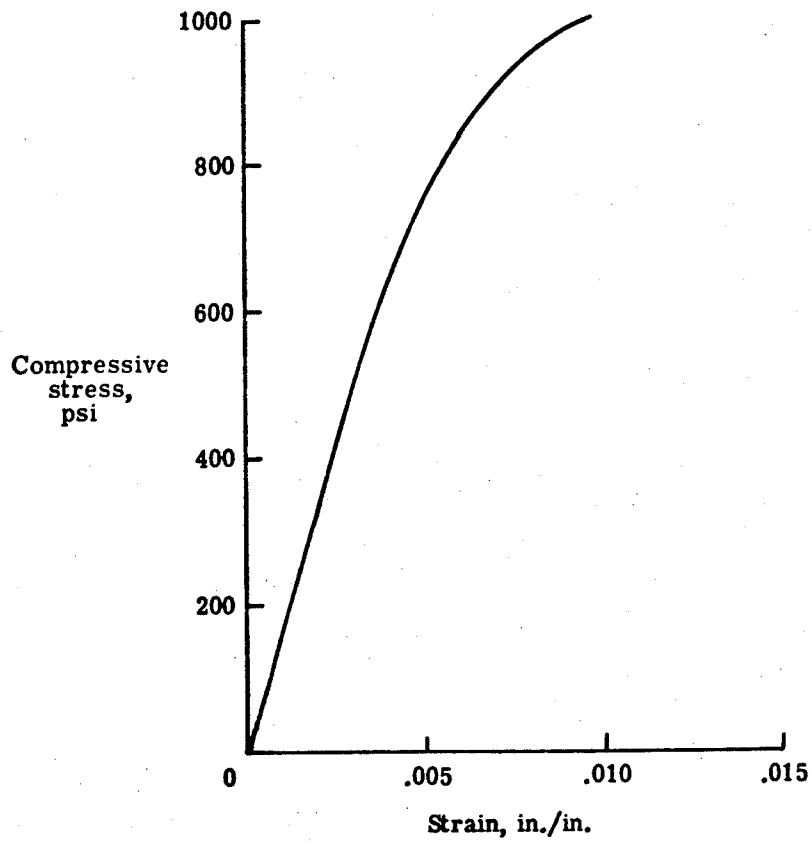


Figure 7.8 - Compressive stress-strain curve for matrix material.

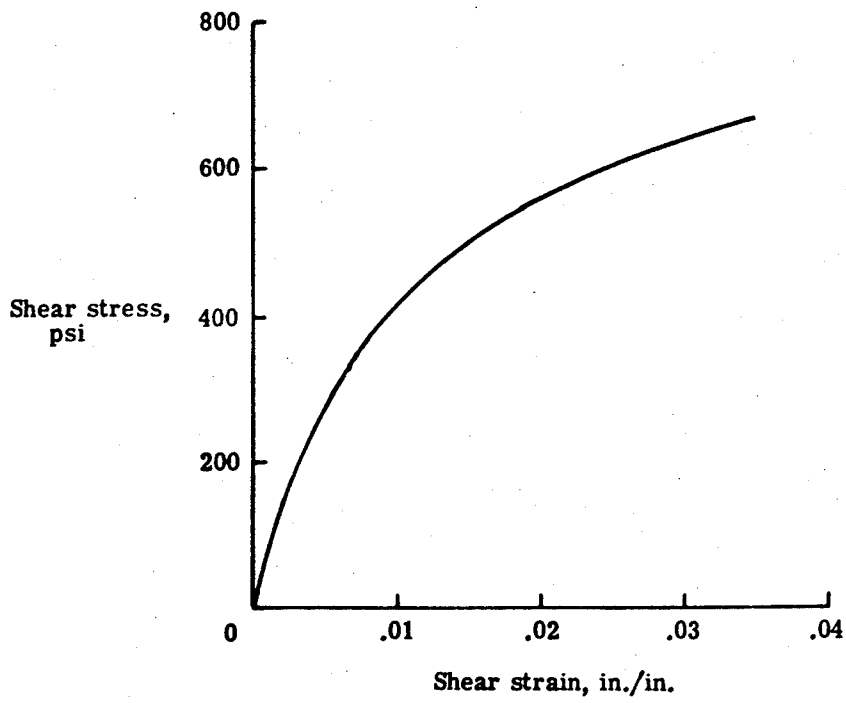


Figure 7.9 - Shear stress strain curve for matrix material.

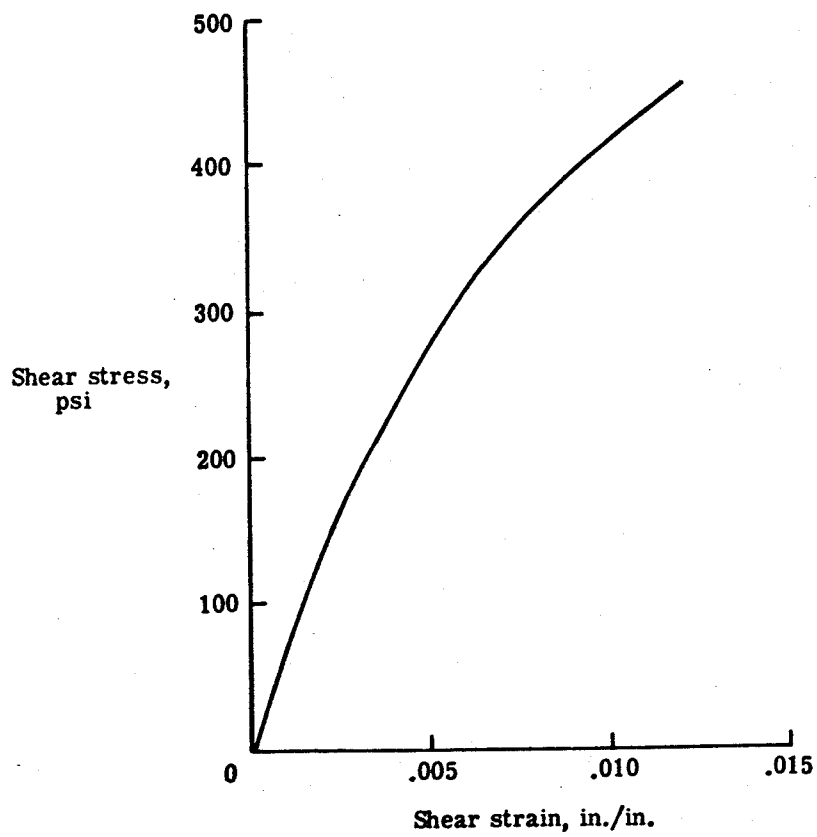


Figure 7.10 - Shear stress-strain curve for matrix material (curve terminated at 0.012 strain).

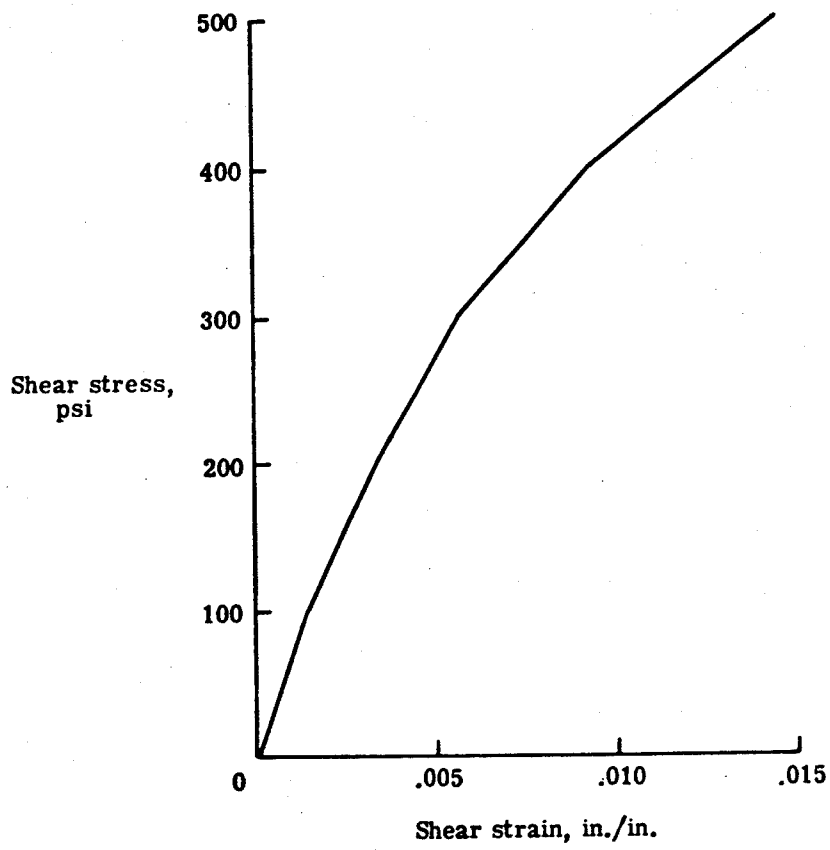


Figure 7.11 - Piecewise linear representation of the shear stress-strain curve for the matrix.

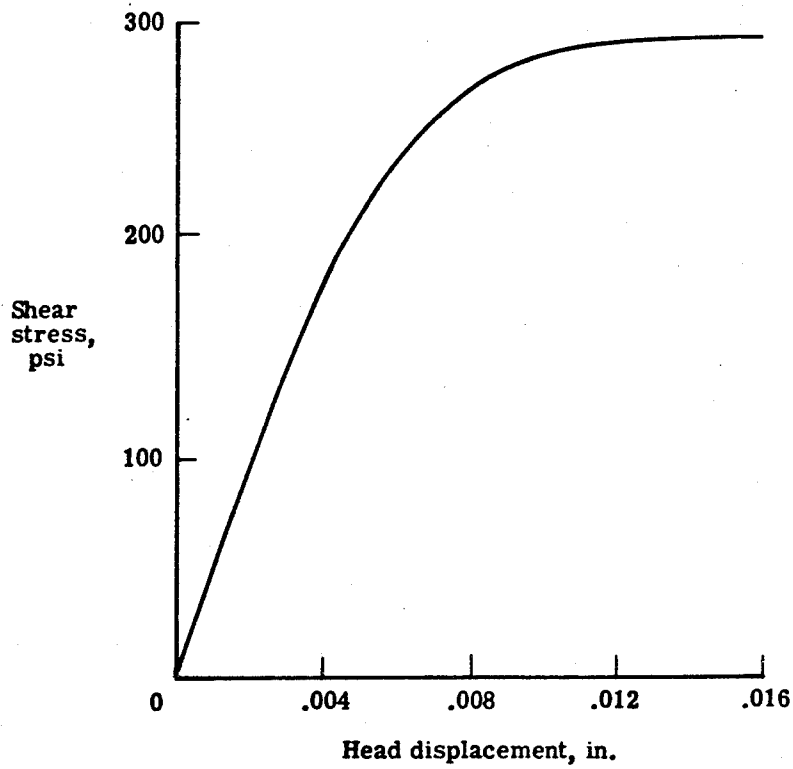


Figure 7.12 - Shear stress-head displacement plot for aluminum-wax bond strength specimen.

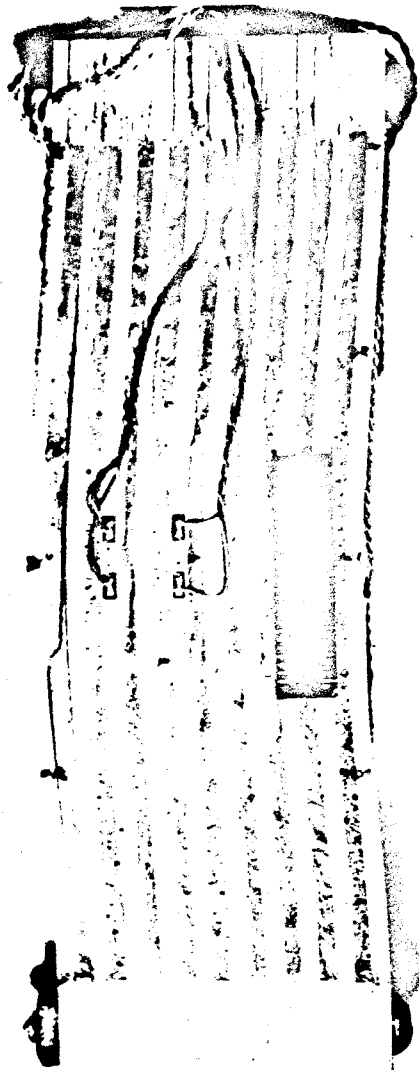


Figure 7.13 - Laminate specimen 1 after failure.



Figure 7.14 - Enlarged view of laminate specimen 1 after failure.

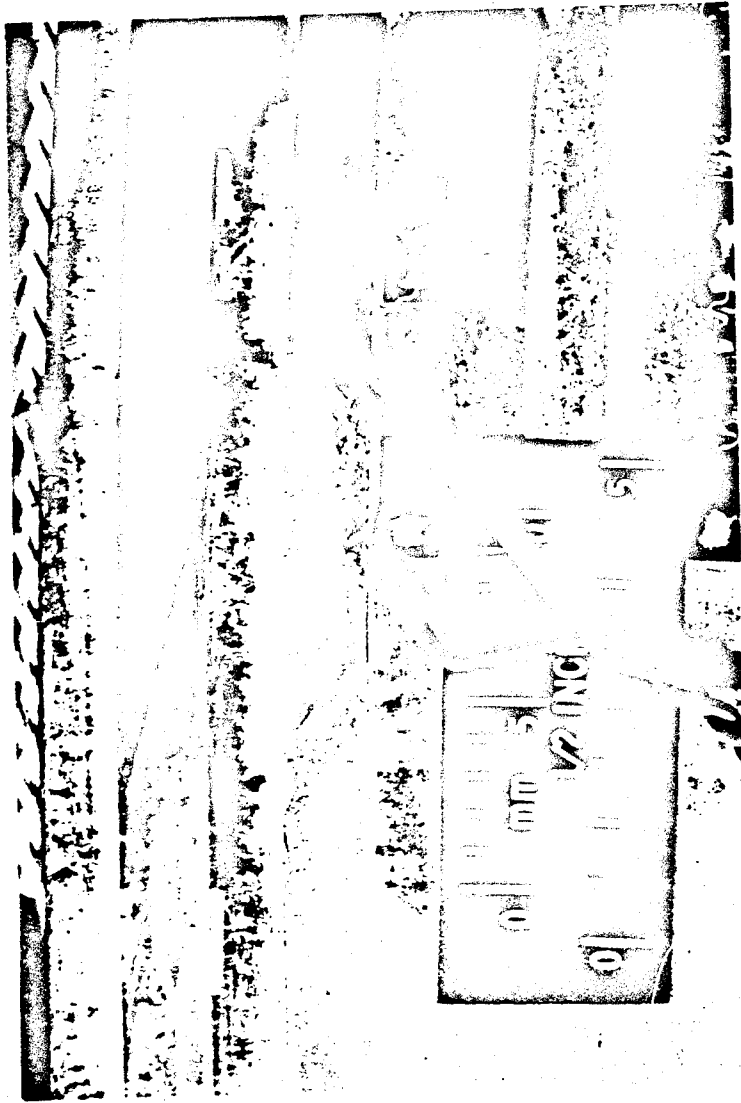


Figure 7.15 - Enlarged view of laminate specimen 2 after failure.

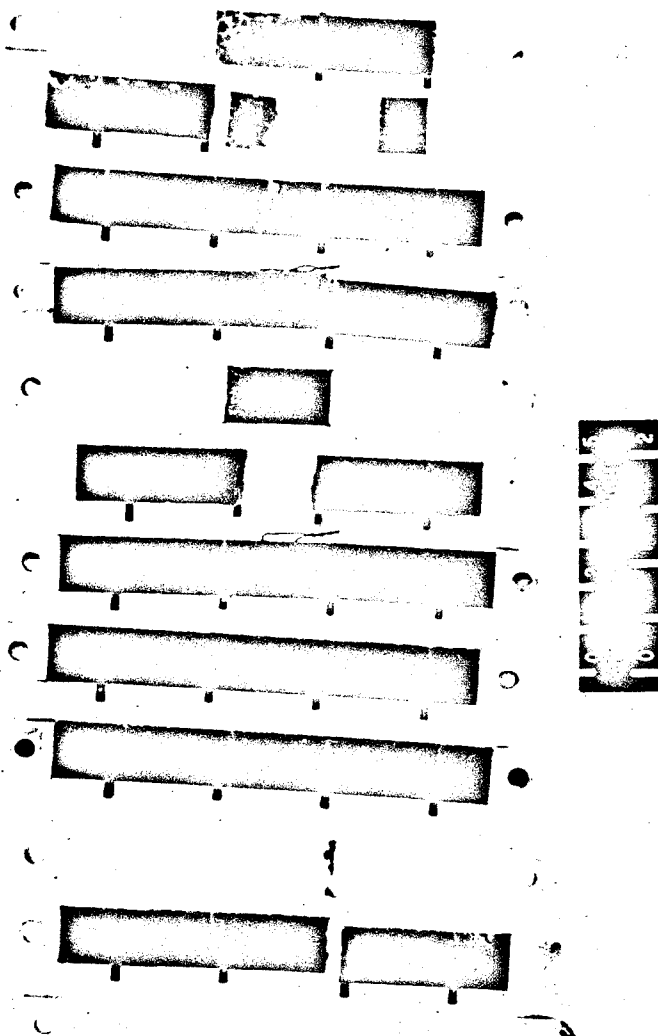


Figure 7.16 - Laminar from specimen 1.

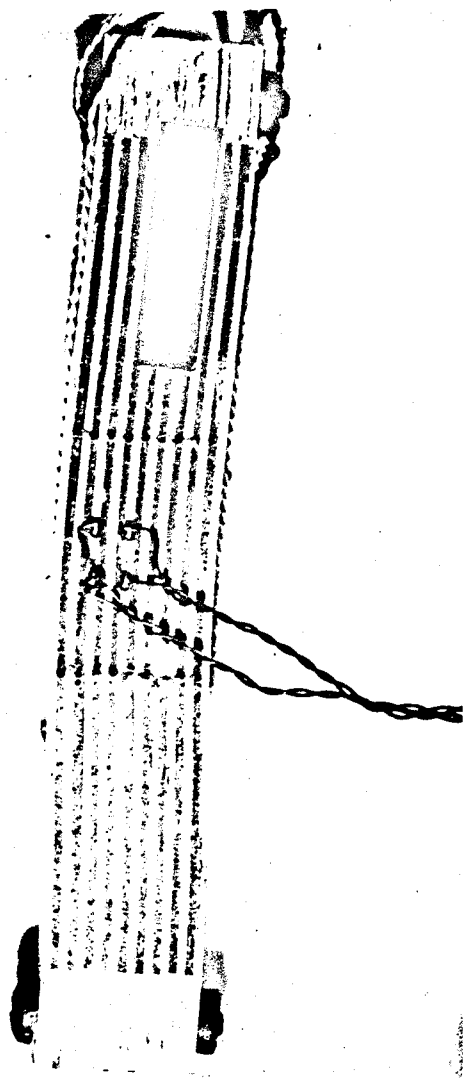


Figure 7.17 - Laminate specimen 4 after failure.



Figure 7.18 - Enlarged view of laminate specimen 4 after failure.

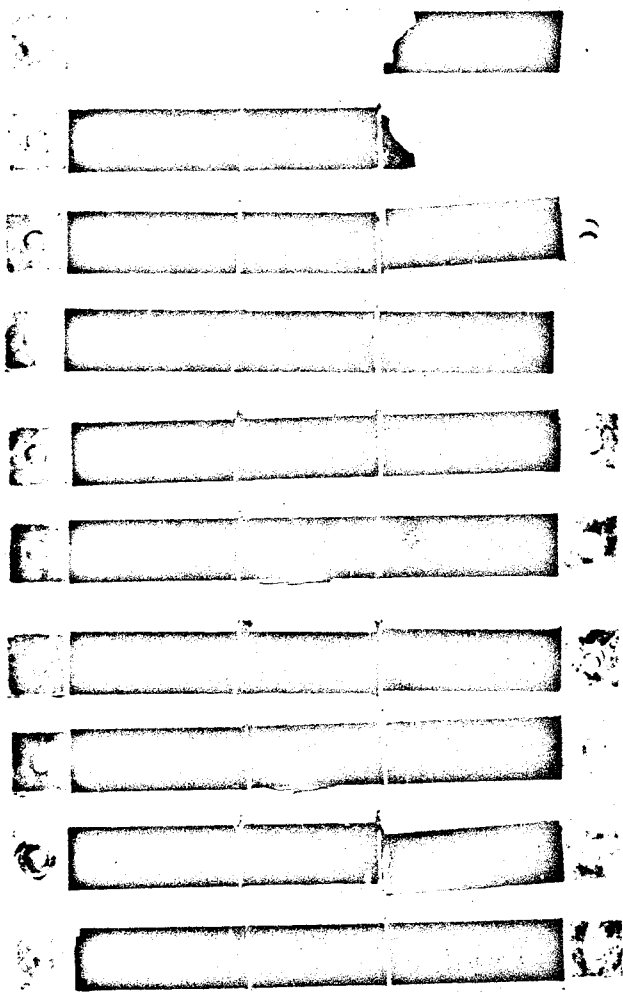


Figure 7.19 - Laminae from specimen 4.

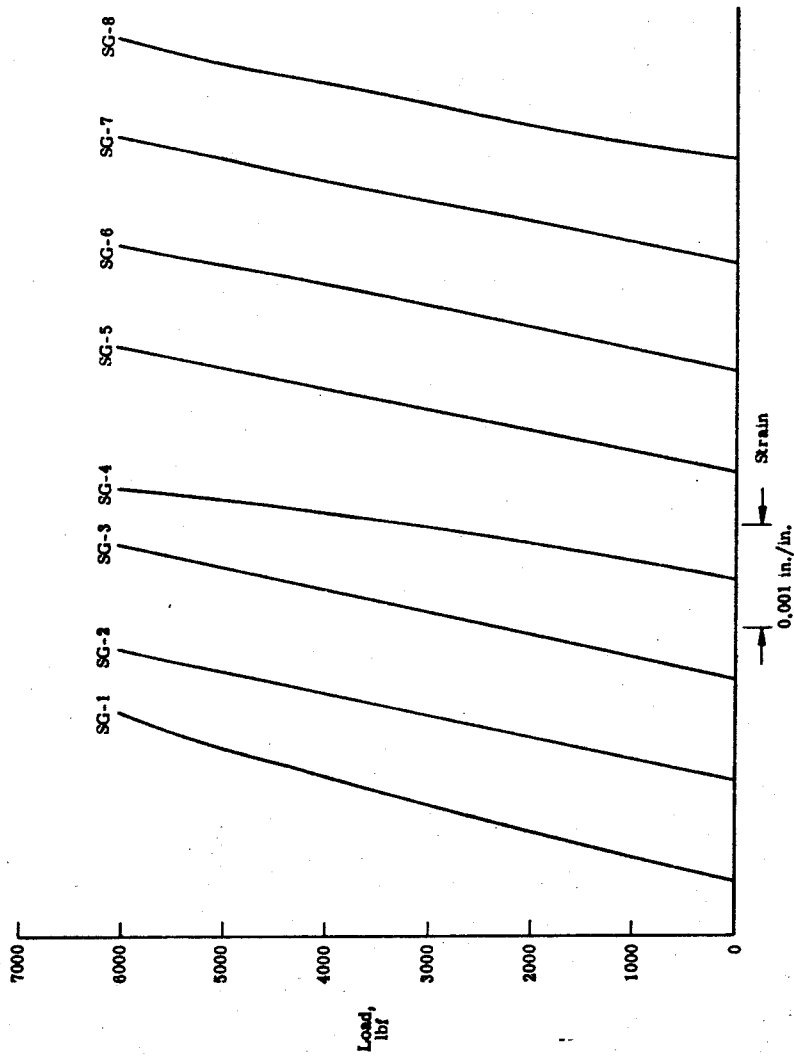


Figure 7.20 - Load-strain plots for laminate specimen 1.

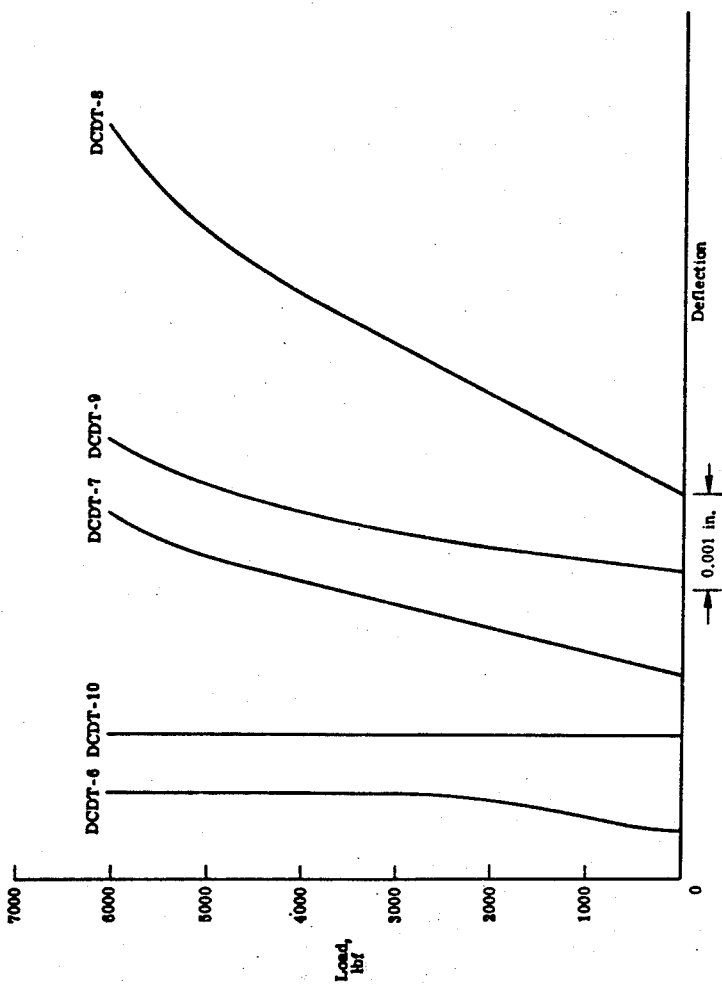


Figure 7.21 - Concluded.

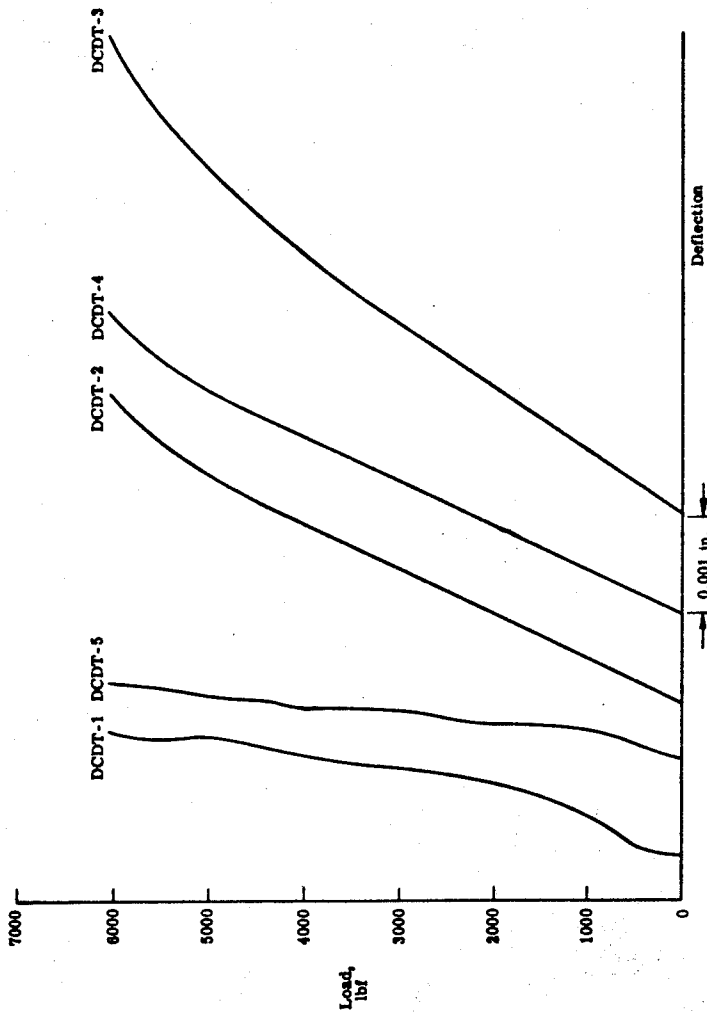


Figure 7.21 - Load-deflection plots for laminate specimen 1.

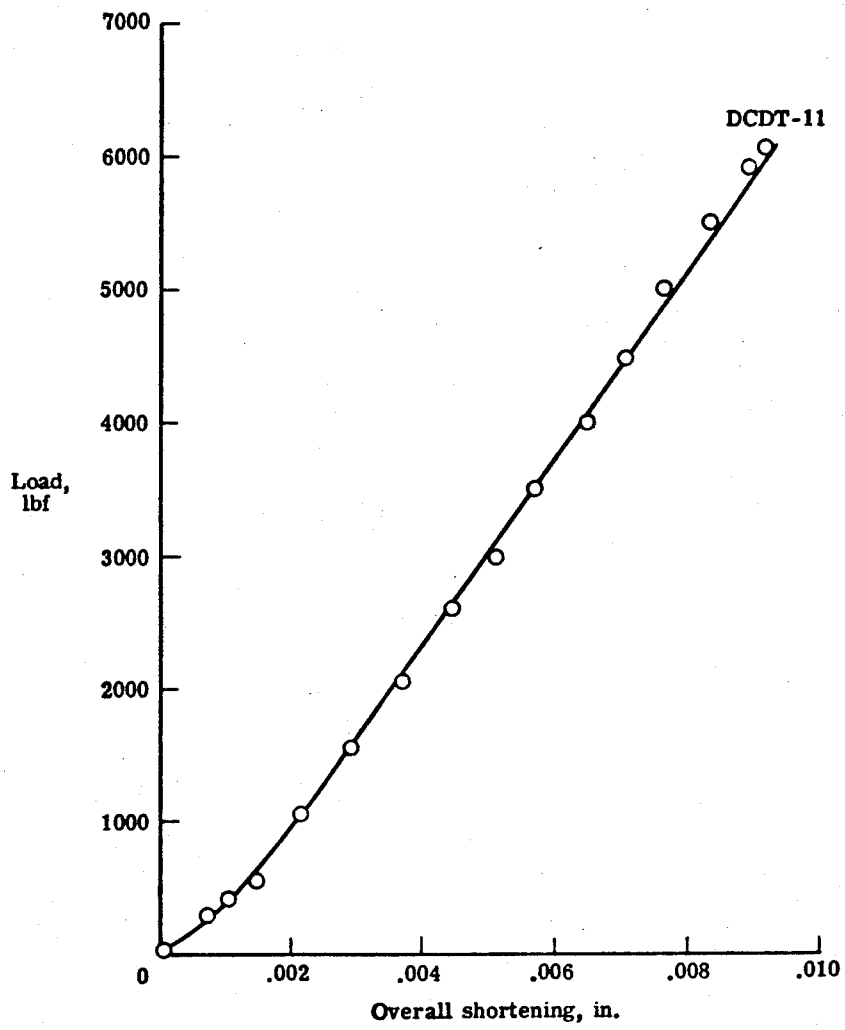


Figure 7.22 - Load-shortening plot for laminate specimen 1.

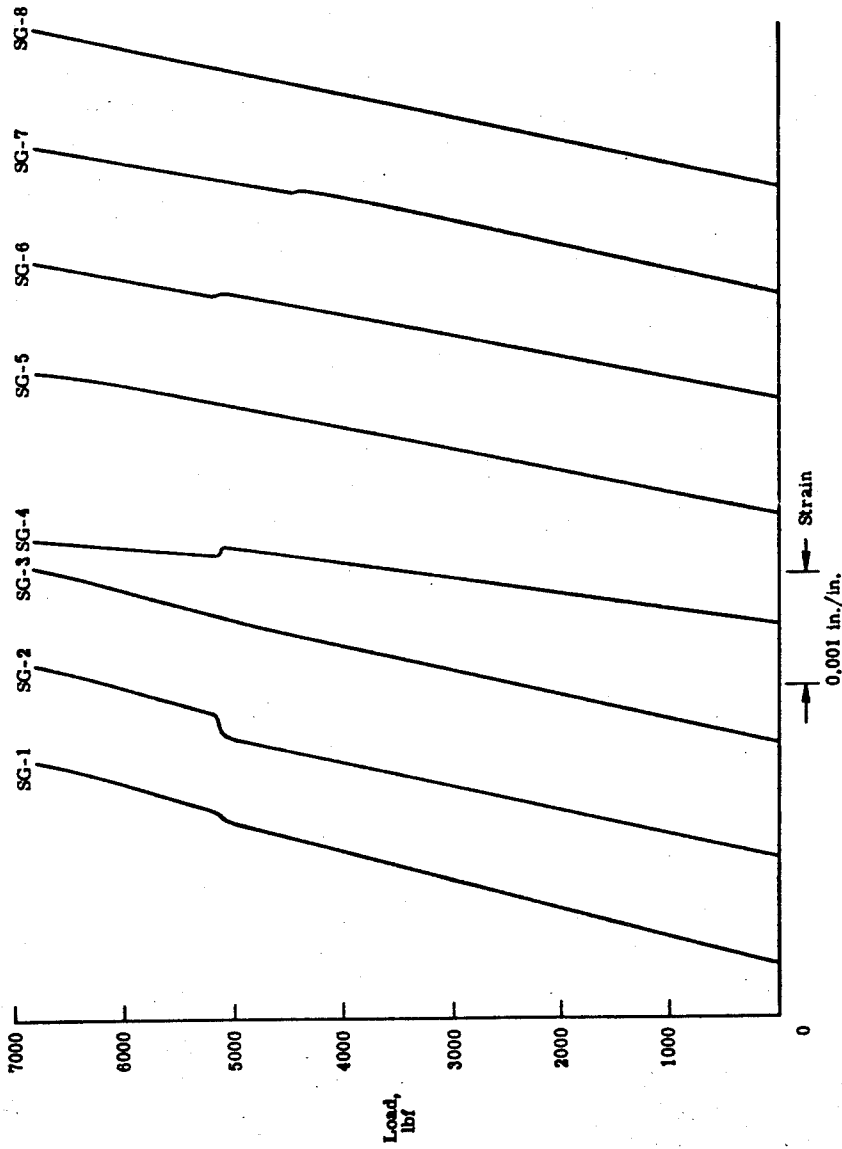


Figure 7.23 - Load-strain plots for laminate specimen 2.

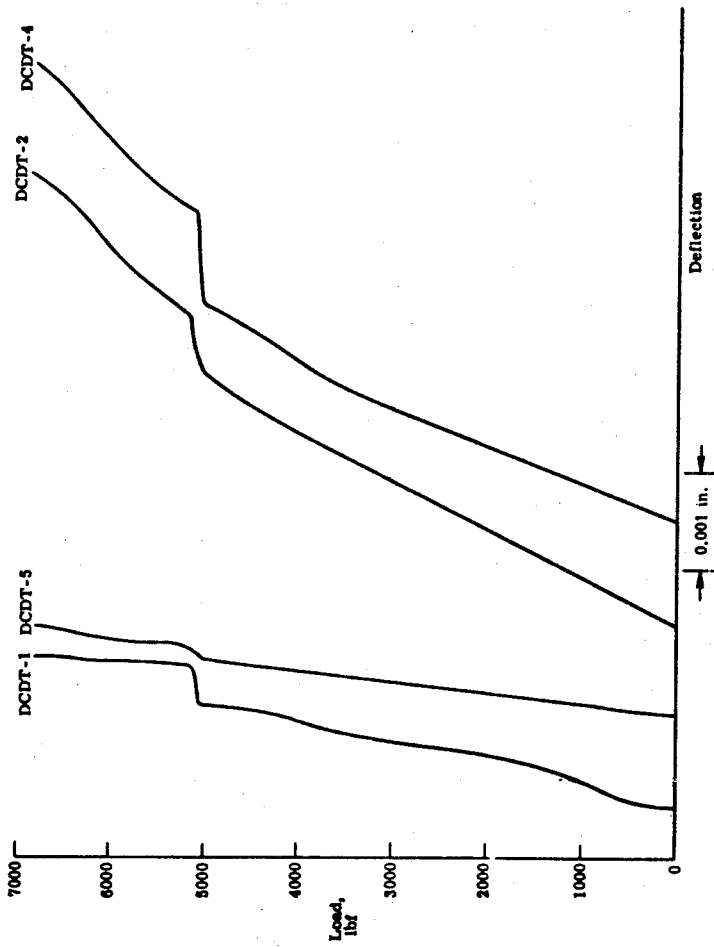


Figure 7.24 - Load-deflection plots for laminate specimen 2.

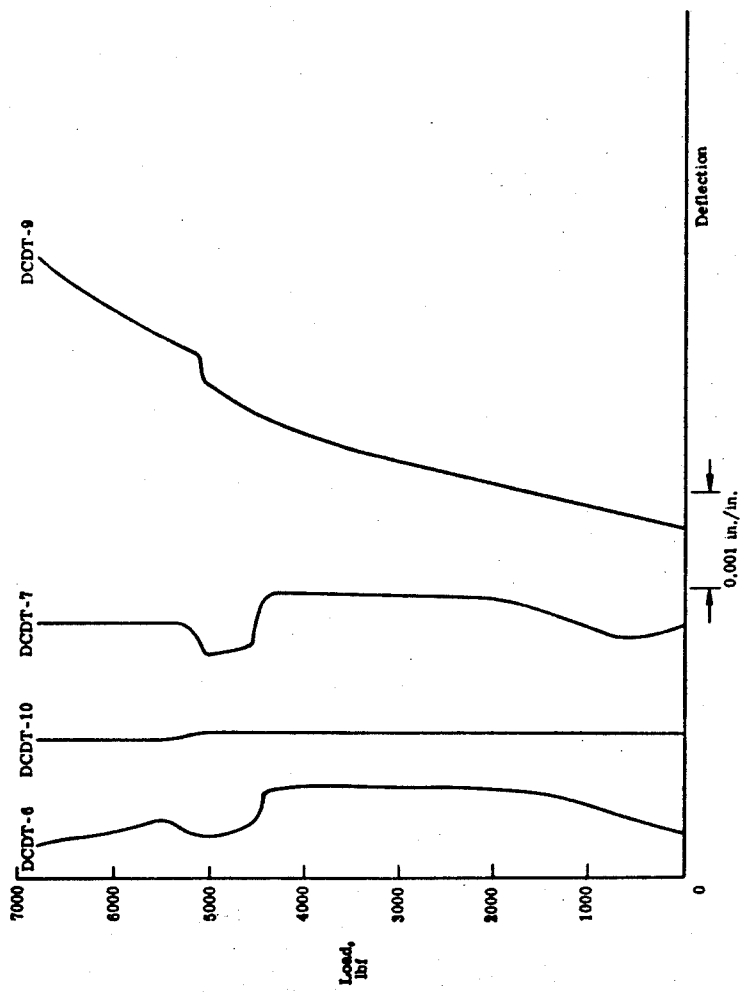


Figure 7.24 - Continued.

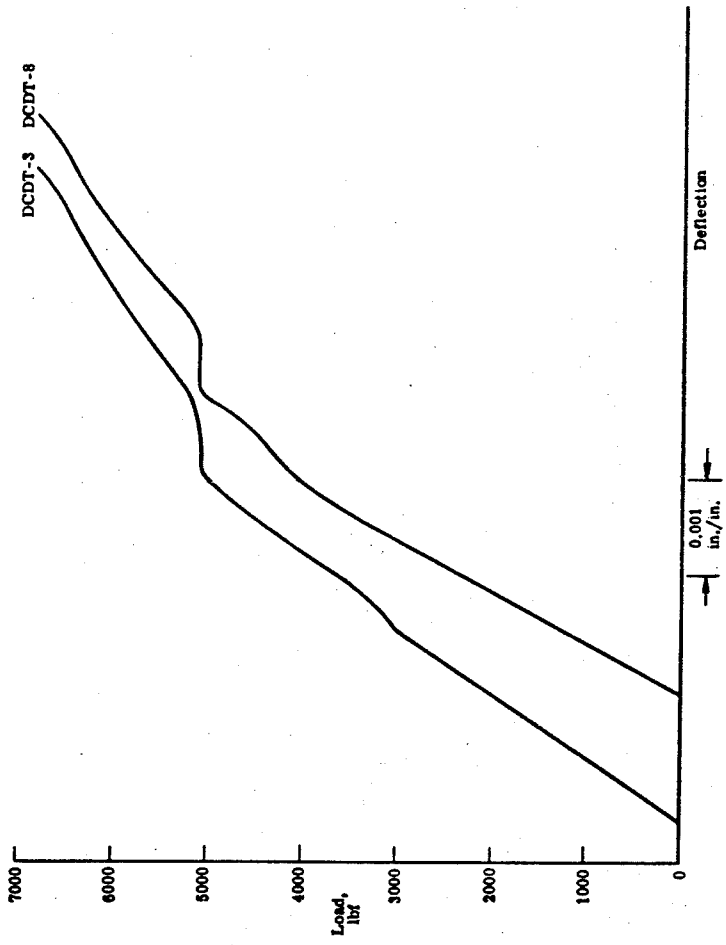


Figure 7.24 - Concluded.

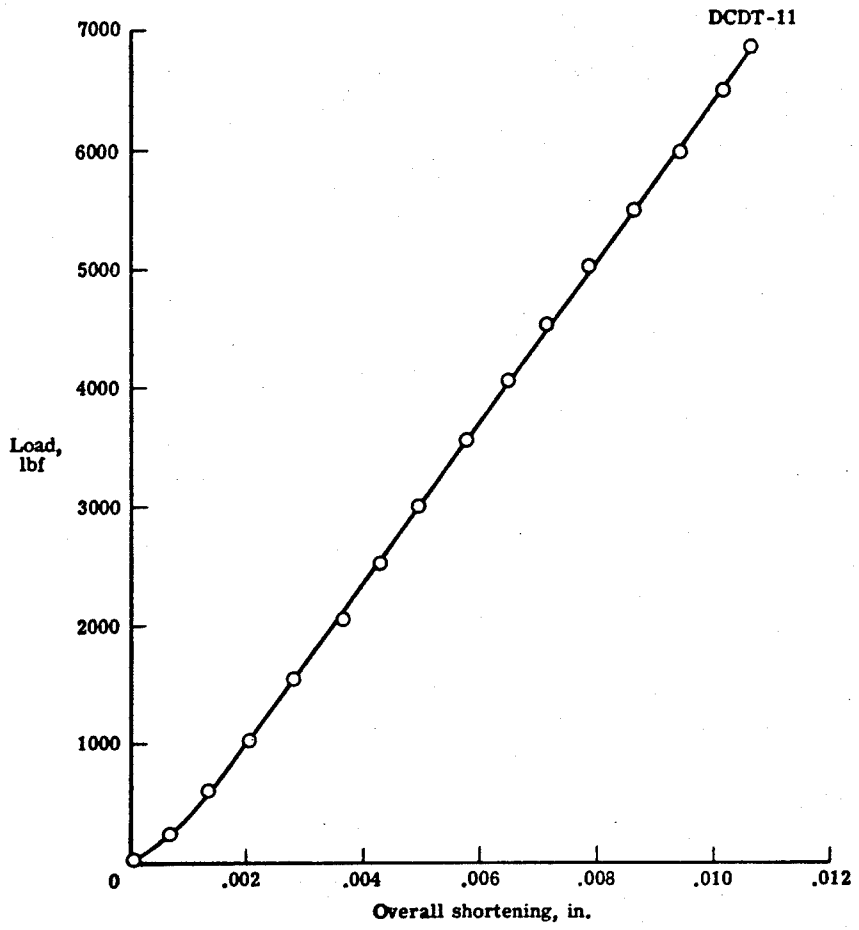


Figure 7.25 - Load-shortening plot for laminate specimen 2.

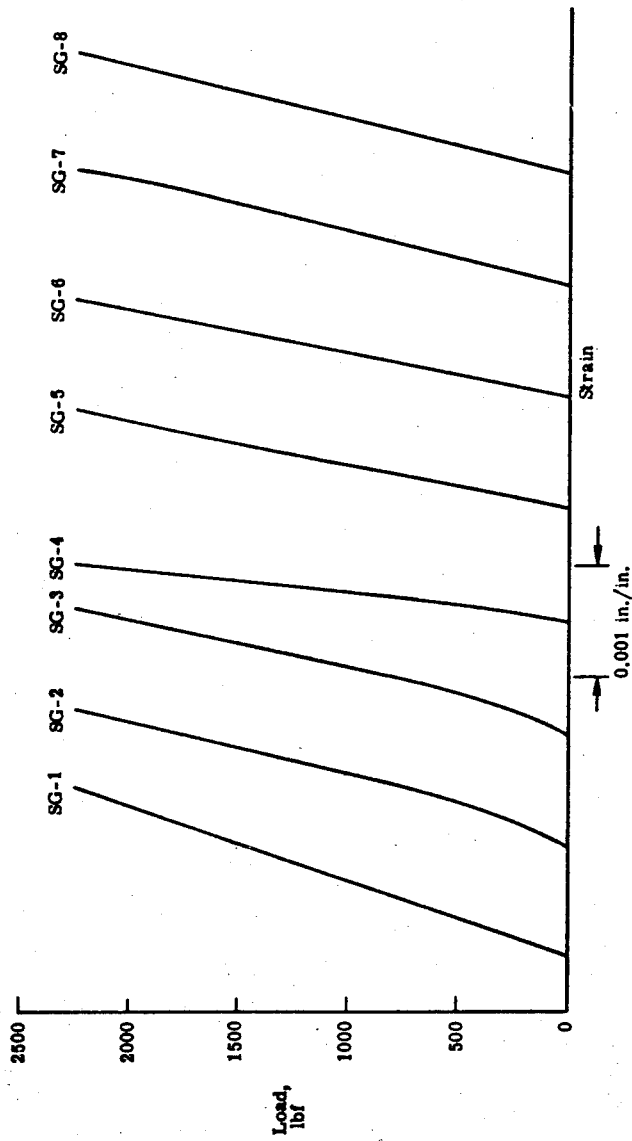


Figure 7.26 - Load-strain plots for laminate specimen 3.

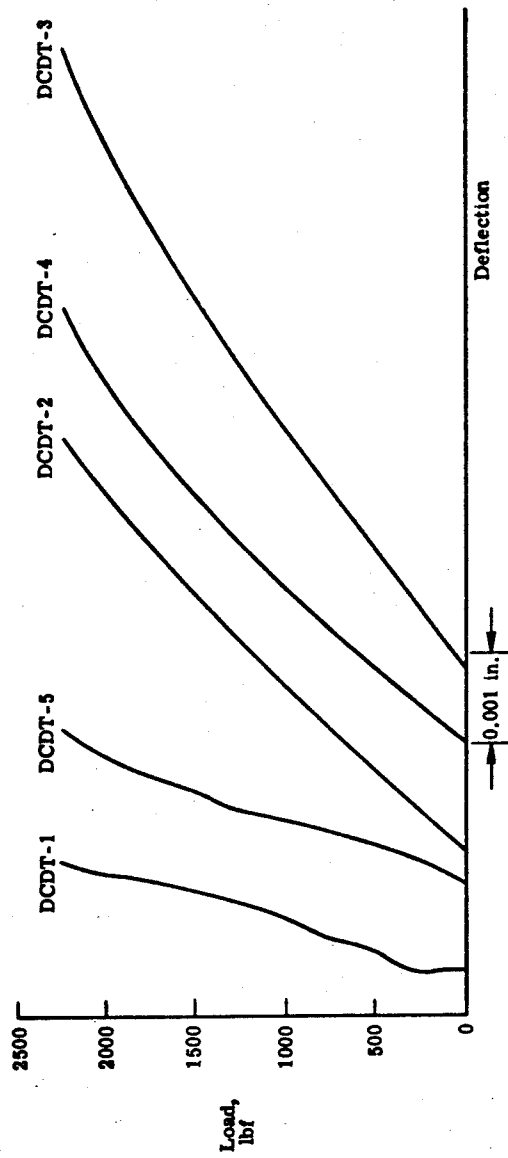


Figure 7.27 - Load-deflection plots for laminate specimen 3.

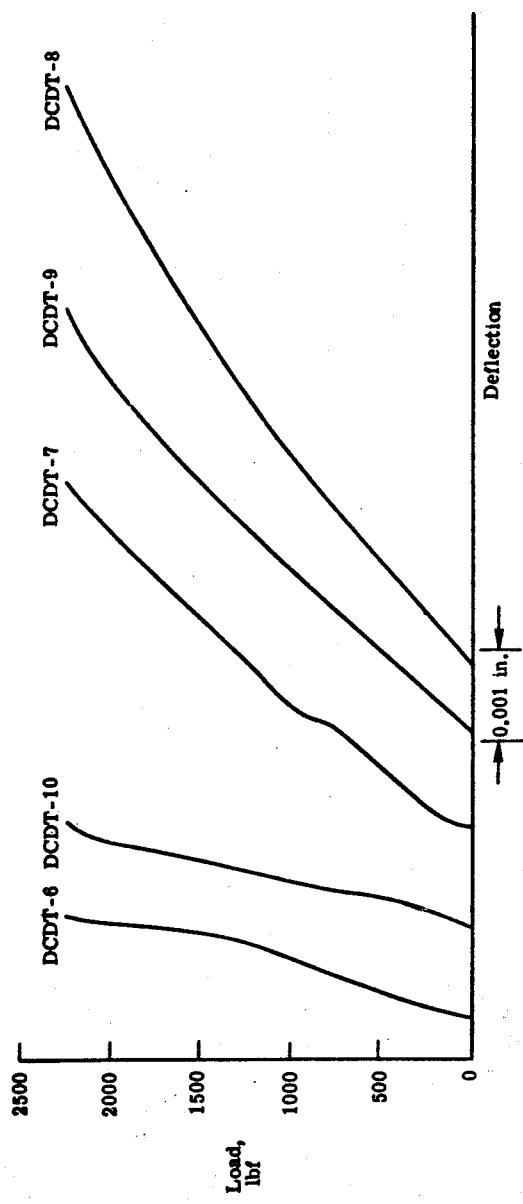


Figure 7.27 - Concluded.

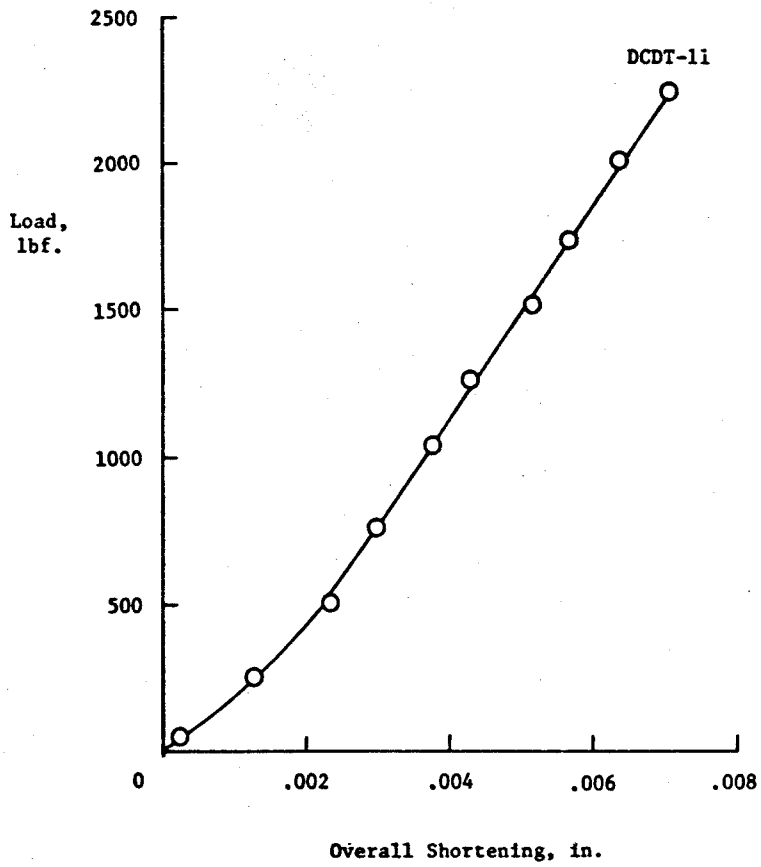


Figure 7.28 - Load-shortening plot for laminate specimen 3.

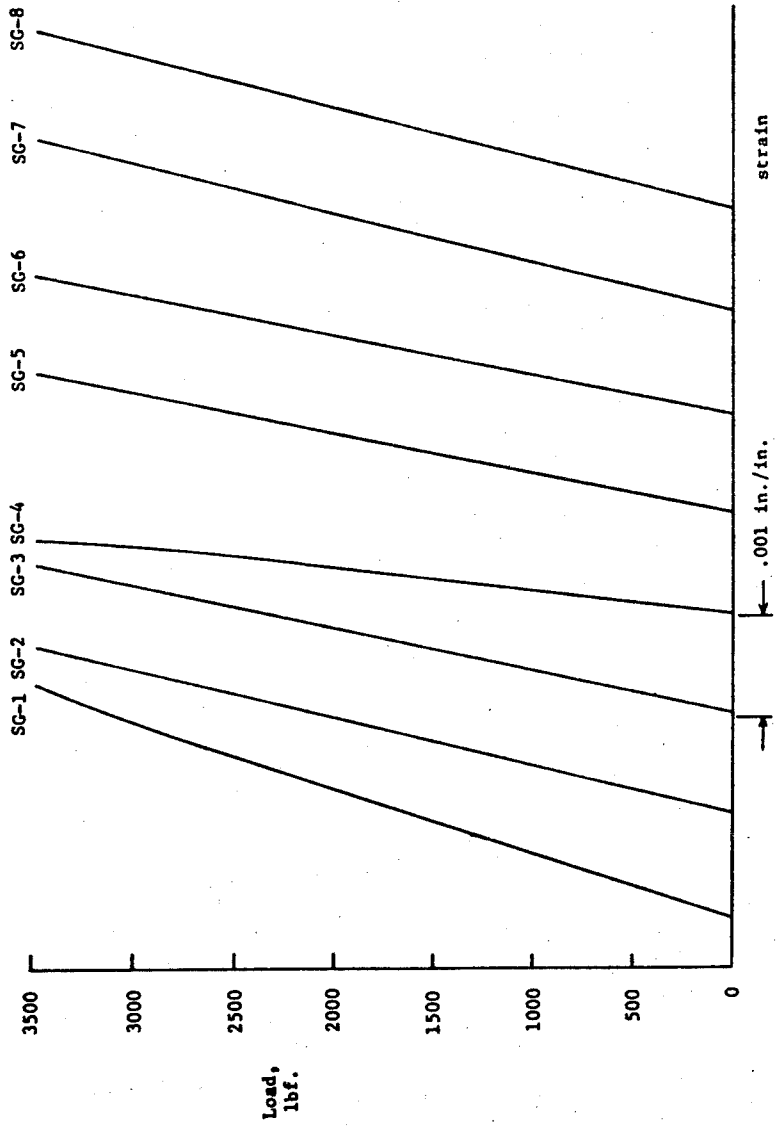


Figure 7.29 - Load-strain plots for laminate specimen 4.

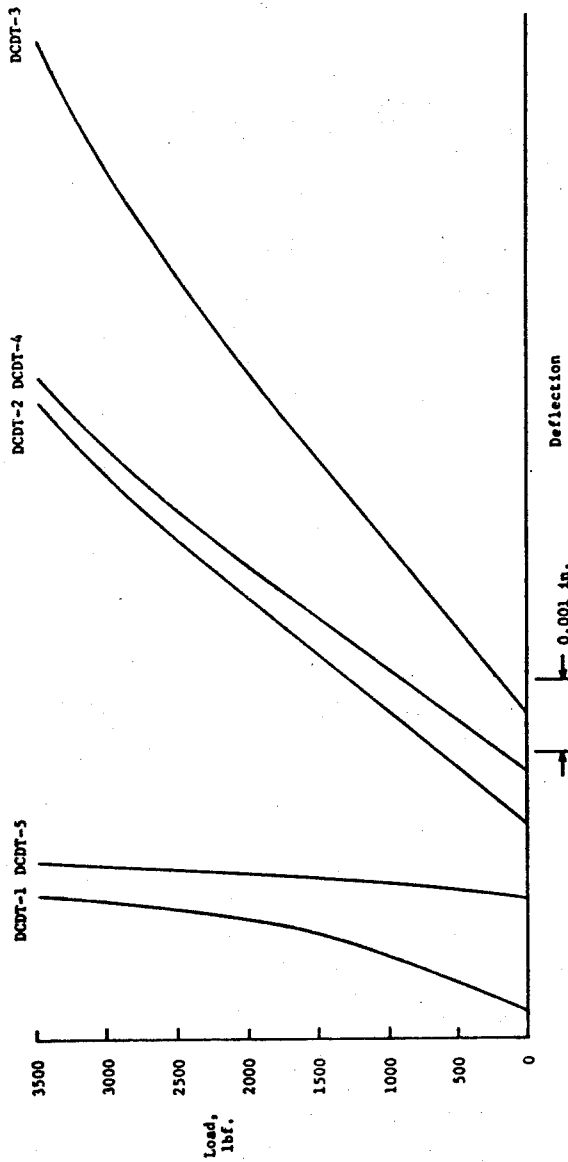


Figure 7.30 - Load-deflection plots for laminate specimen 4.

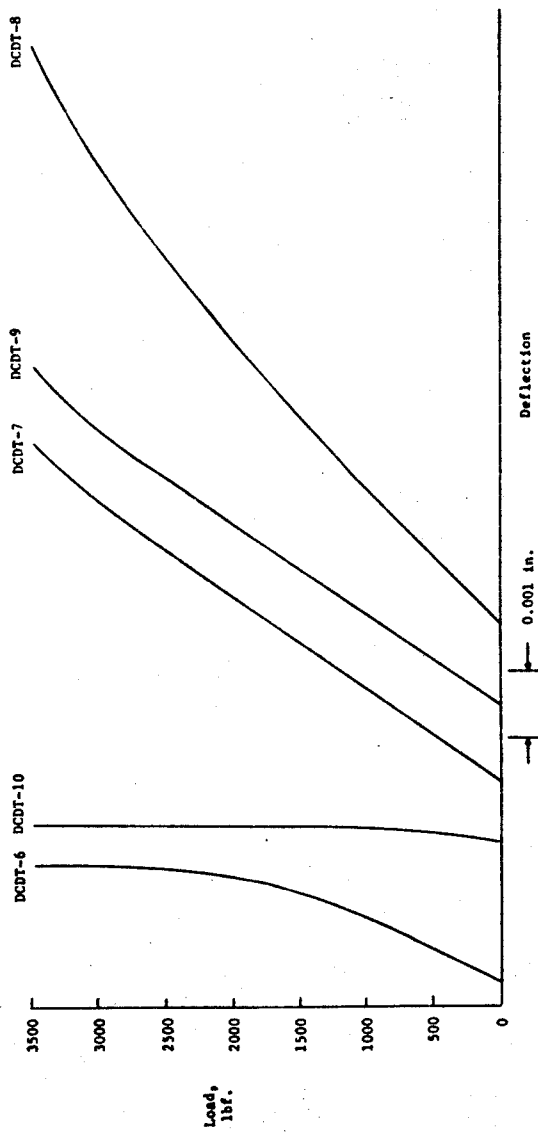


Figure 7.30 - Concluded.

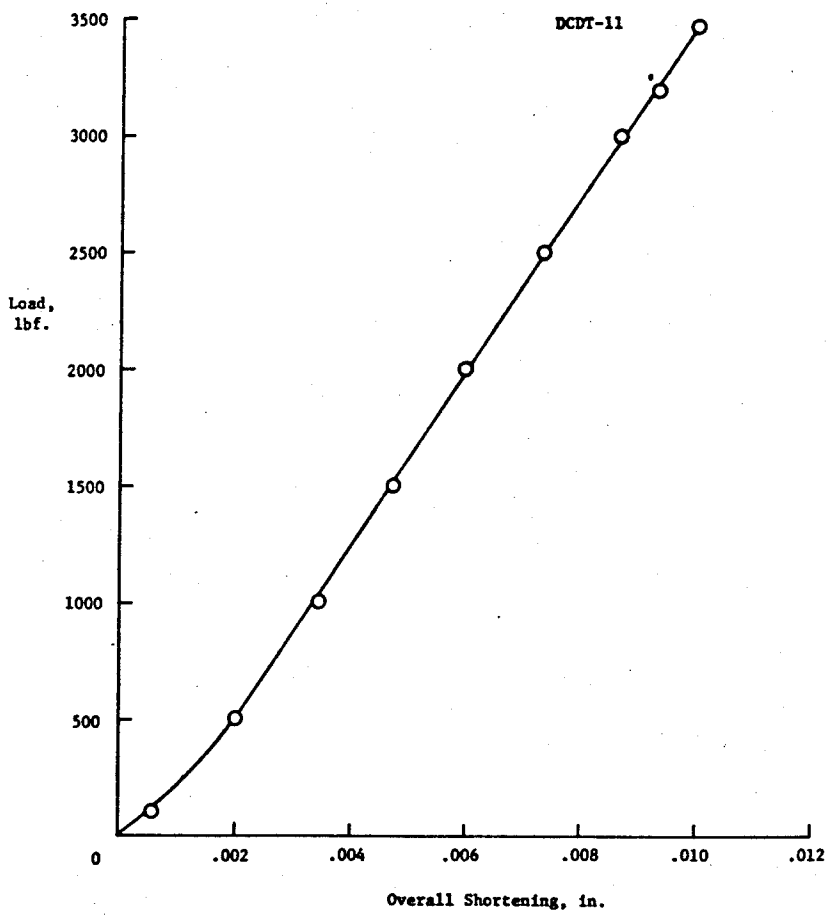


Figure 7.31 - Load-shortening plot for laminate specimen 4.

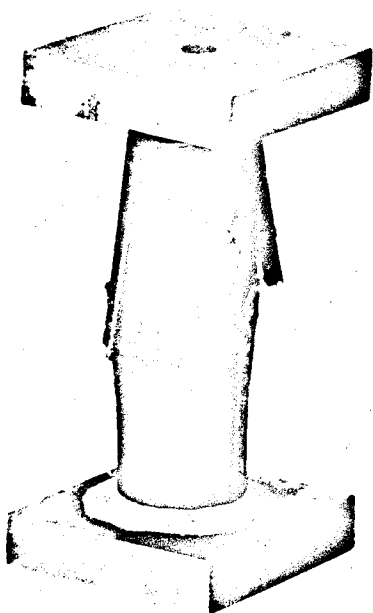


Figure 7.32 - Failed boron-epoxy compression specimen (4 mil fiber).

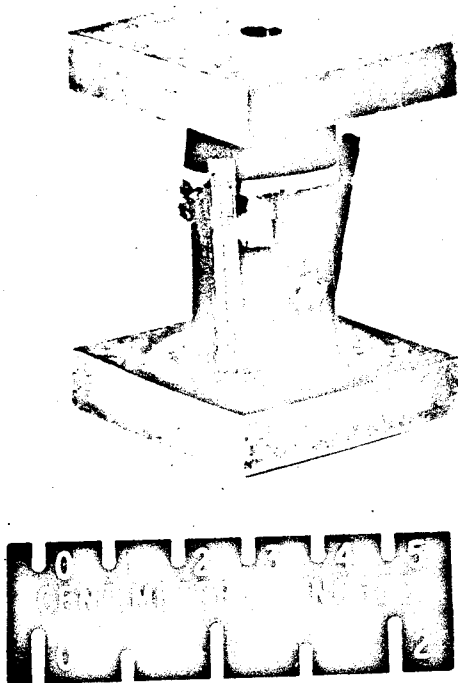


Figure 7.33 - Failed boron-epoxy compression specimen (5.6 mil fiber).

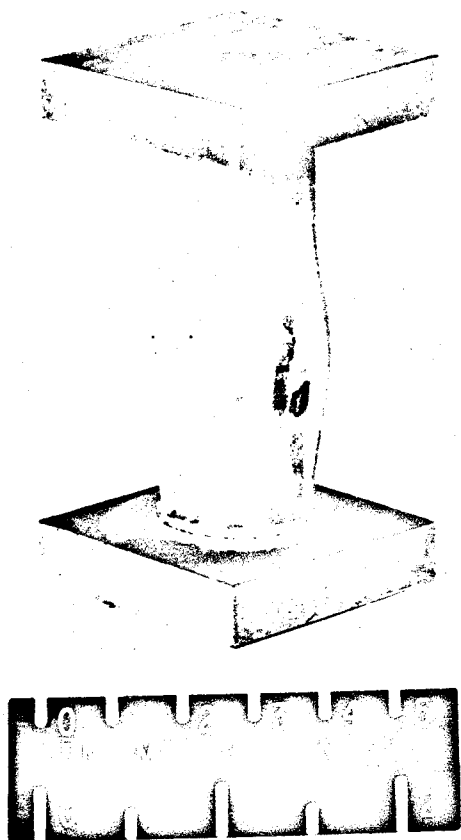


Figure 7.34 - Failed glass-epoxy compression specimen.

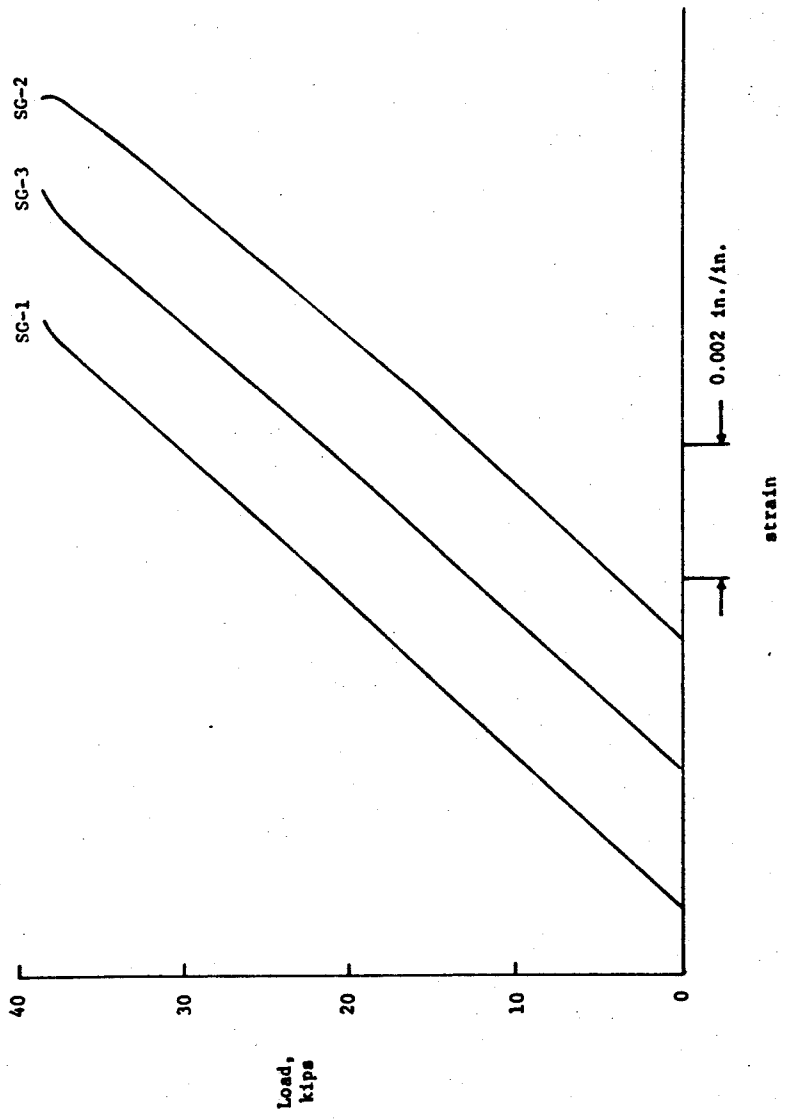


Figure 7.35 - Compressive load-strain plots for boron-epoxy specimen 1-1.

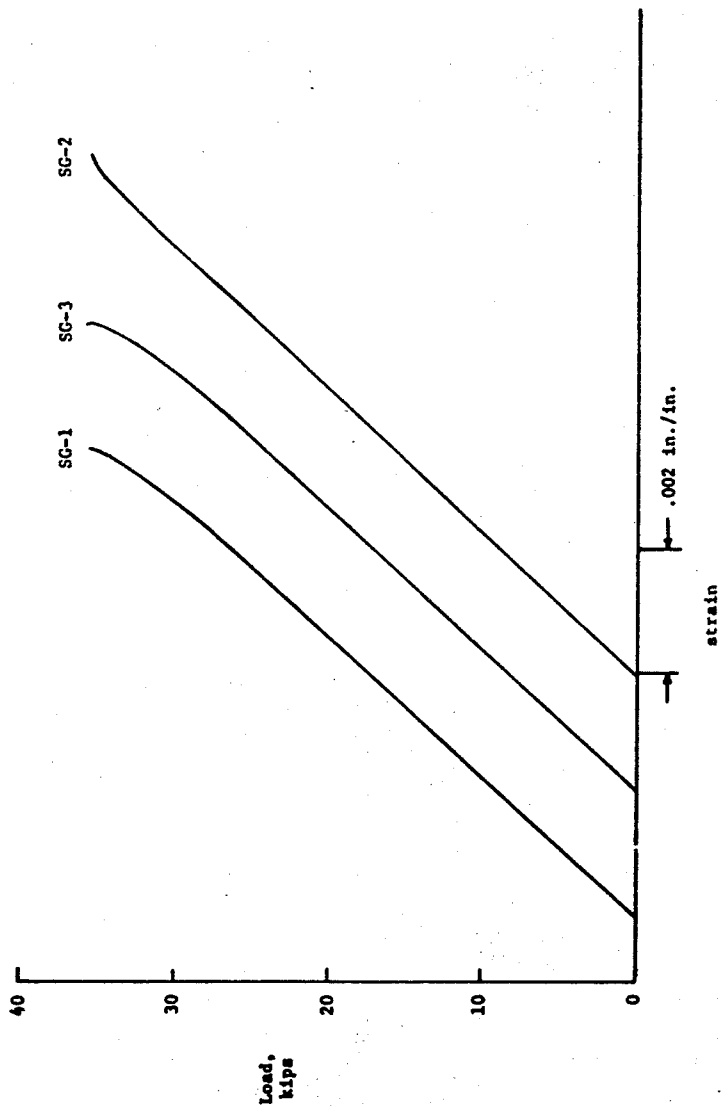


Figure 7.36 - Compressive load-strain plots for boron-epoxy specimen 1-2.

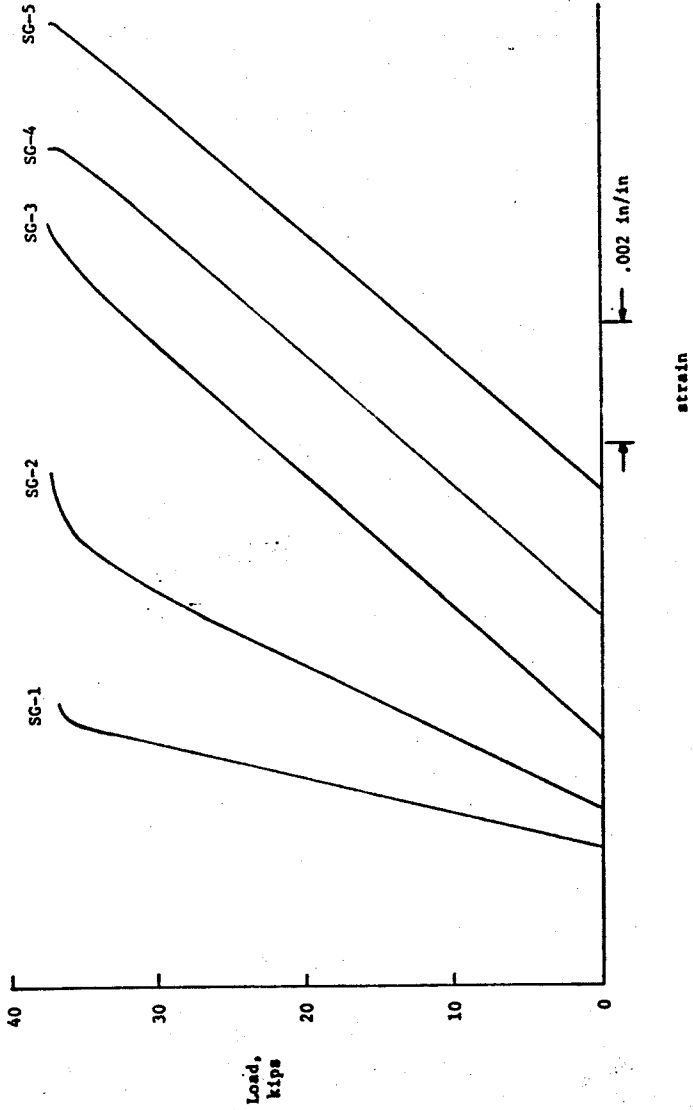


Figure 7.37 - Compressive load-strain plots for boron-epoxy specimen 1-3.

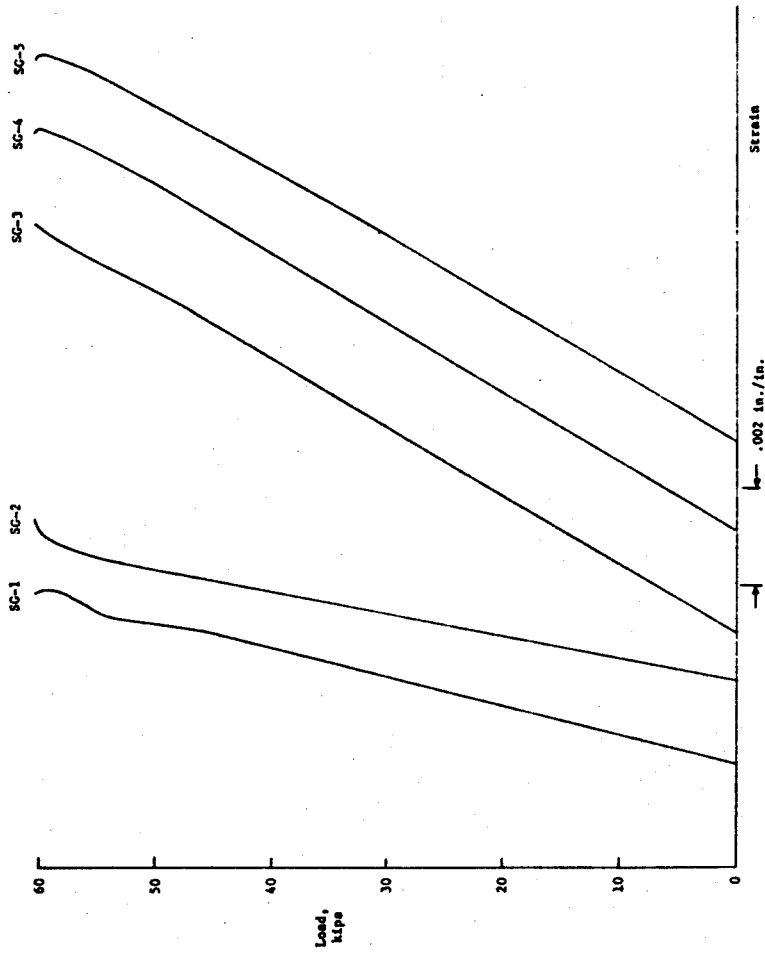


Figure 7.38 - Compressive load-strain plots for boron-epoxy specimen 2-1.

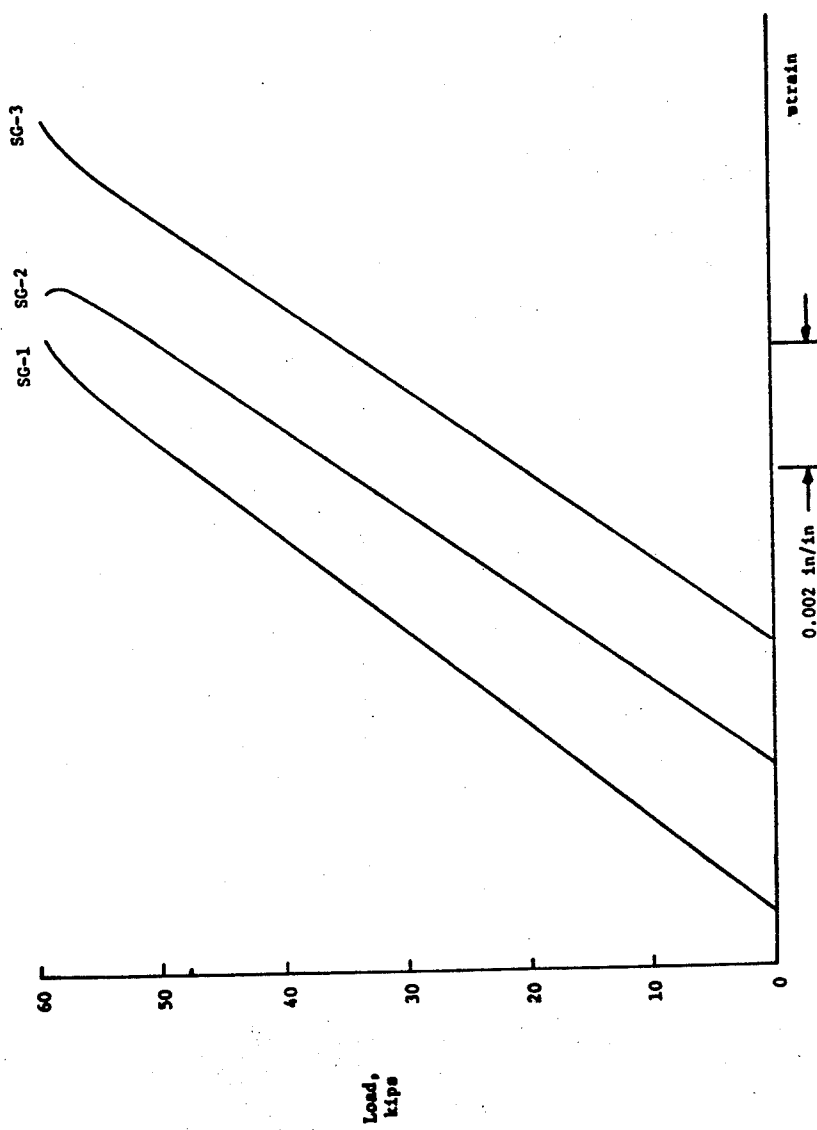


Figure 7.39 - Compressive load-strain plots for boron-epoxy specimen 2-2.

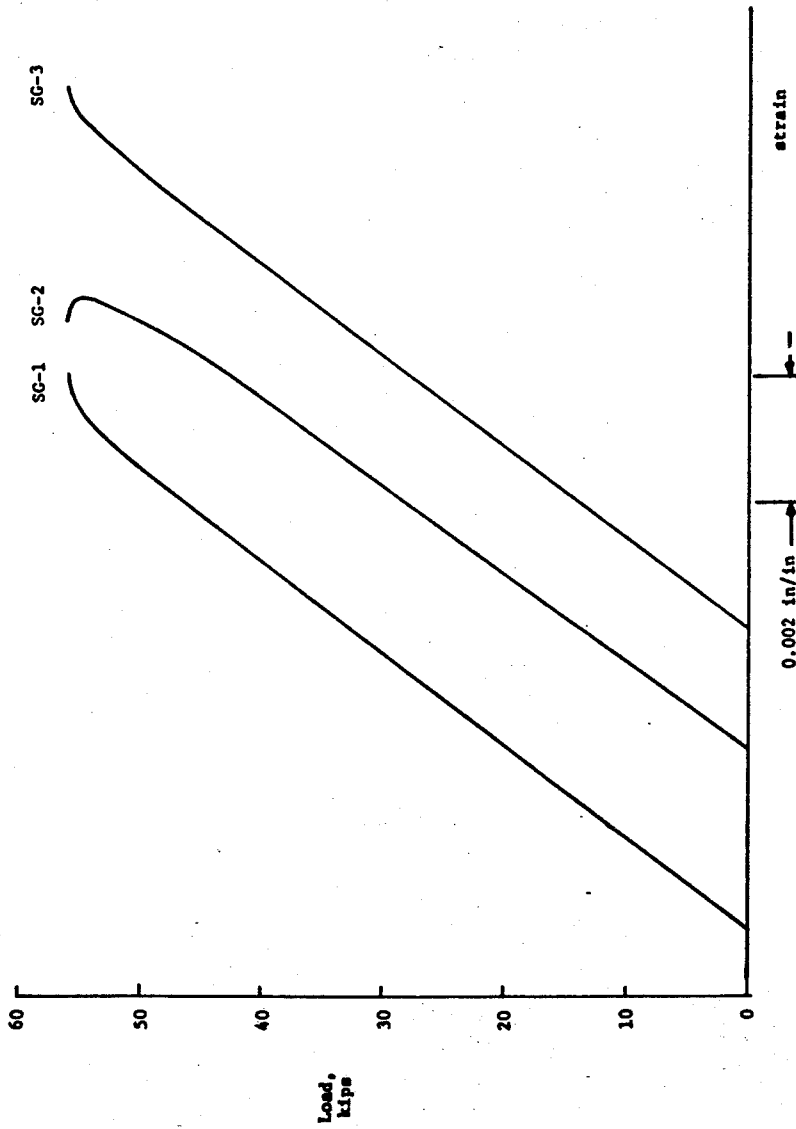


Figure 7.40 - Compressive load-strain plot for boron-epoxy specimen 2-3.

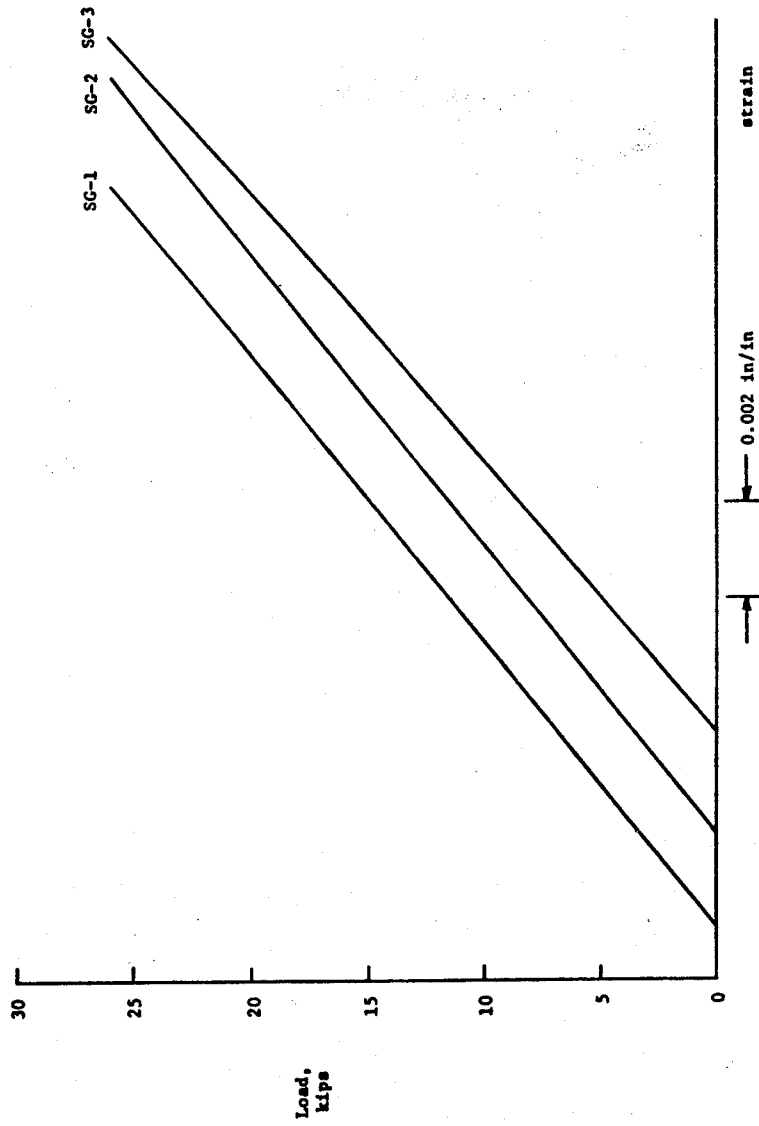


Figure 7.41 - Compressive load-strain plots for glass-epoxy specimen 3-1.

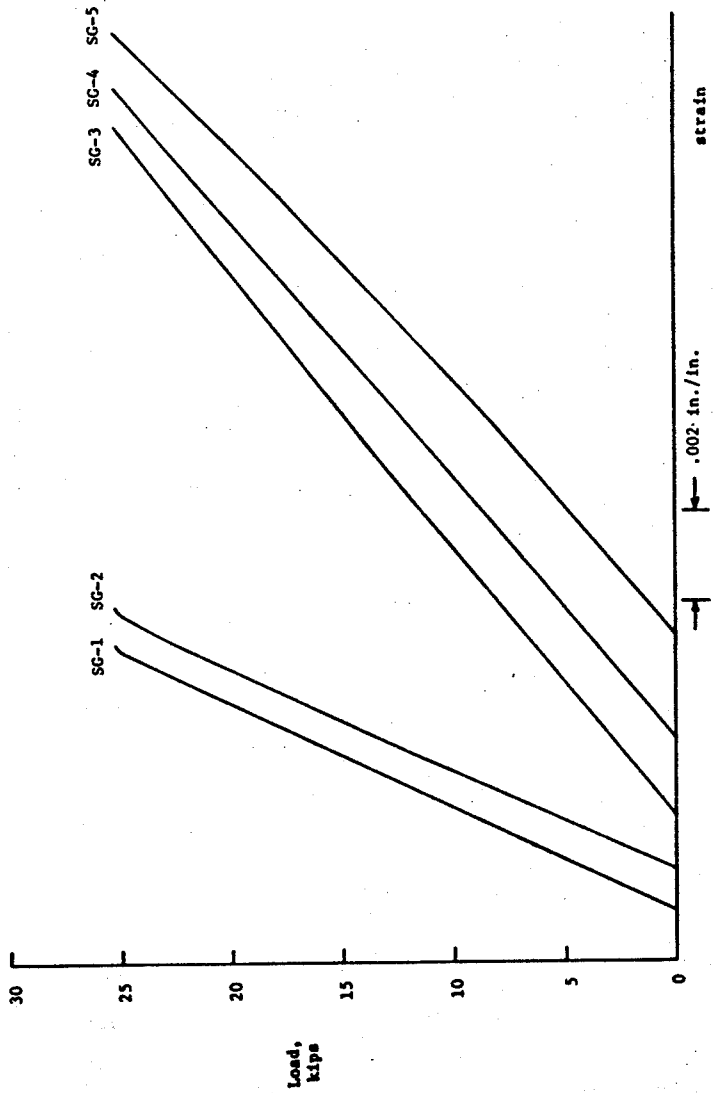


Figure 7.42 - Compressive load-strain plots for glass-epoxy specimen 3-2.

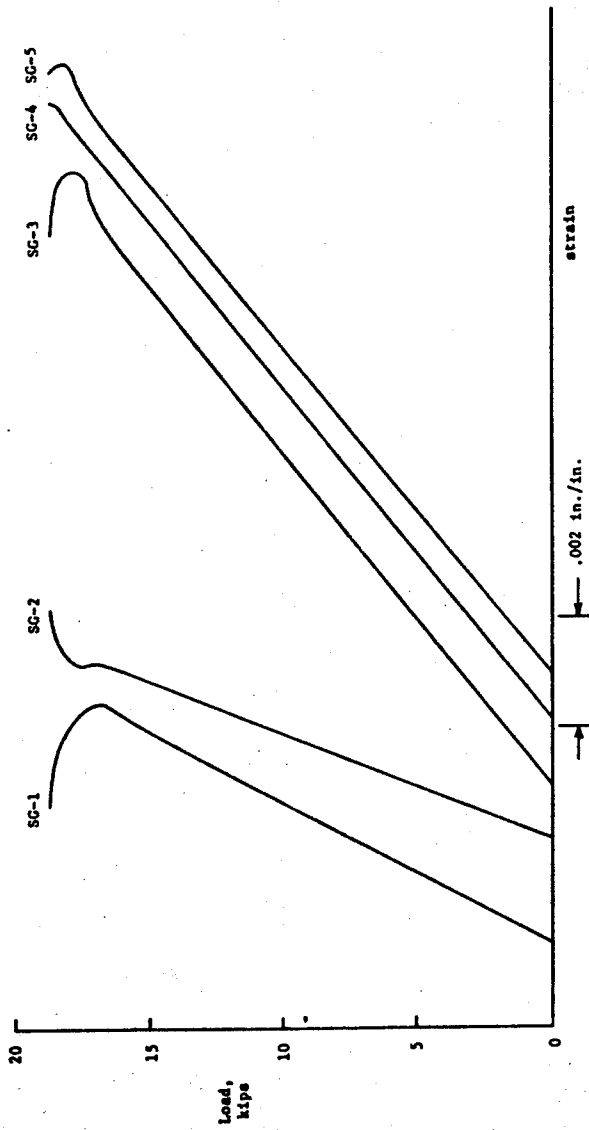


Figure 7.13 - Compressive load-strain plots for glass-epoxy specimen 3-3.

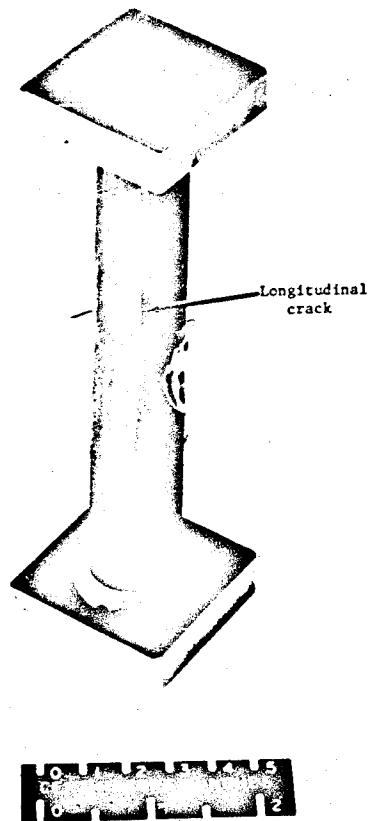


Figure 7.44 - Failed boron-epoxy torsion specimen.

203

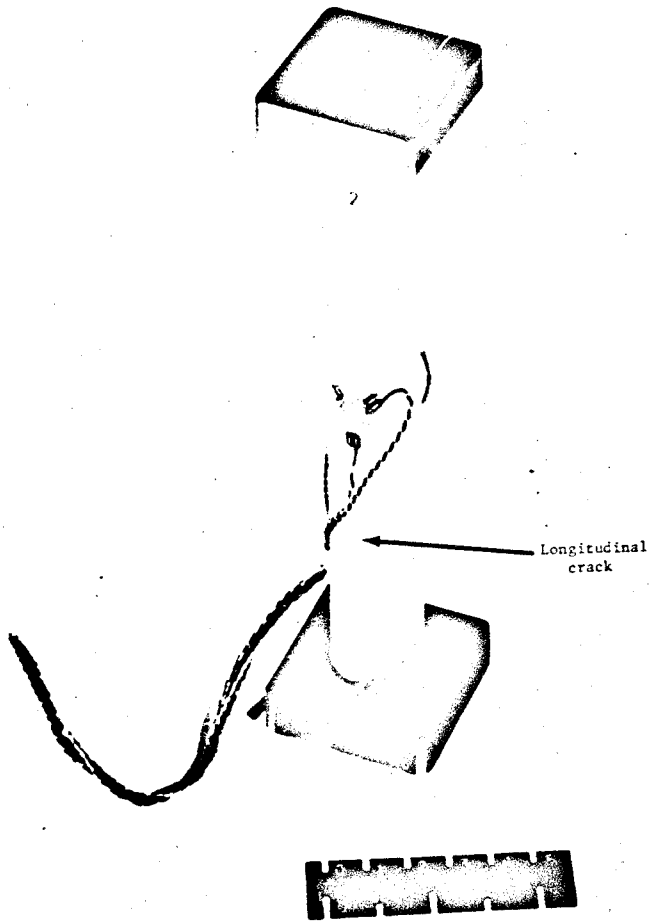


Figure 7.45 - Failed glass-epoxy torsion specimen.

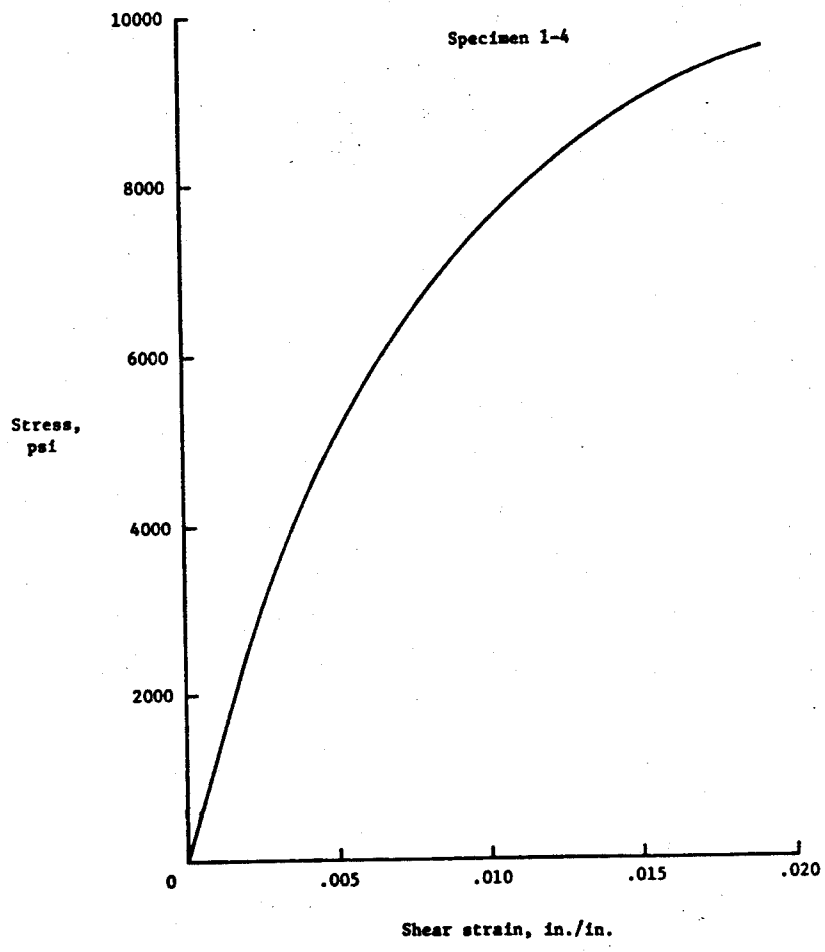


Figure 7.46 - Shear stress-strain curve for boron-epoxy (4.0 mil filaments).

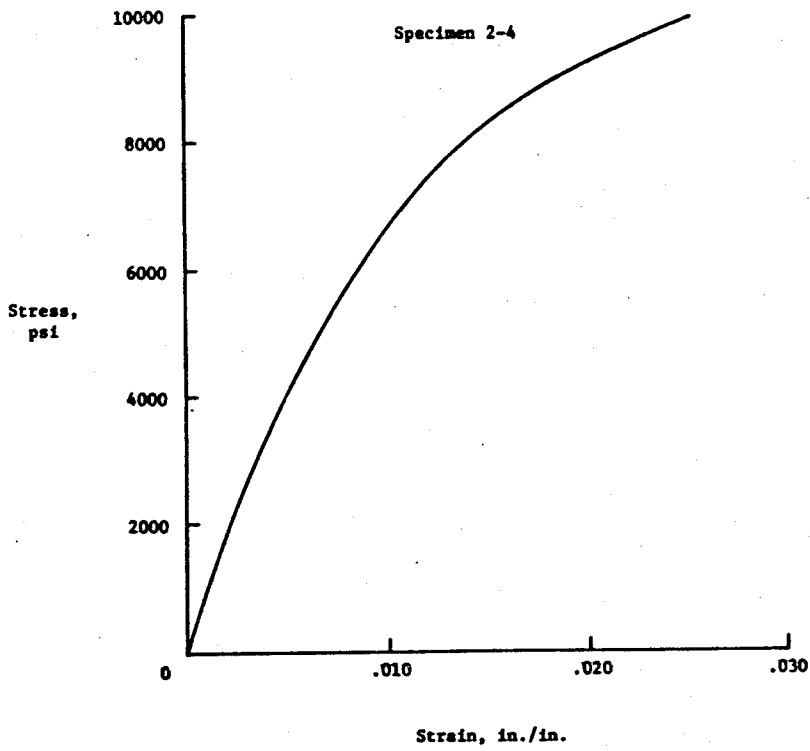


Figure 7.47 - Shear stress-strain curve for boron-epoxy (5.6 mil filaments).

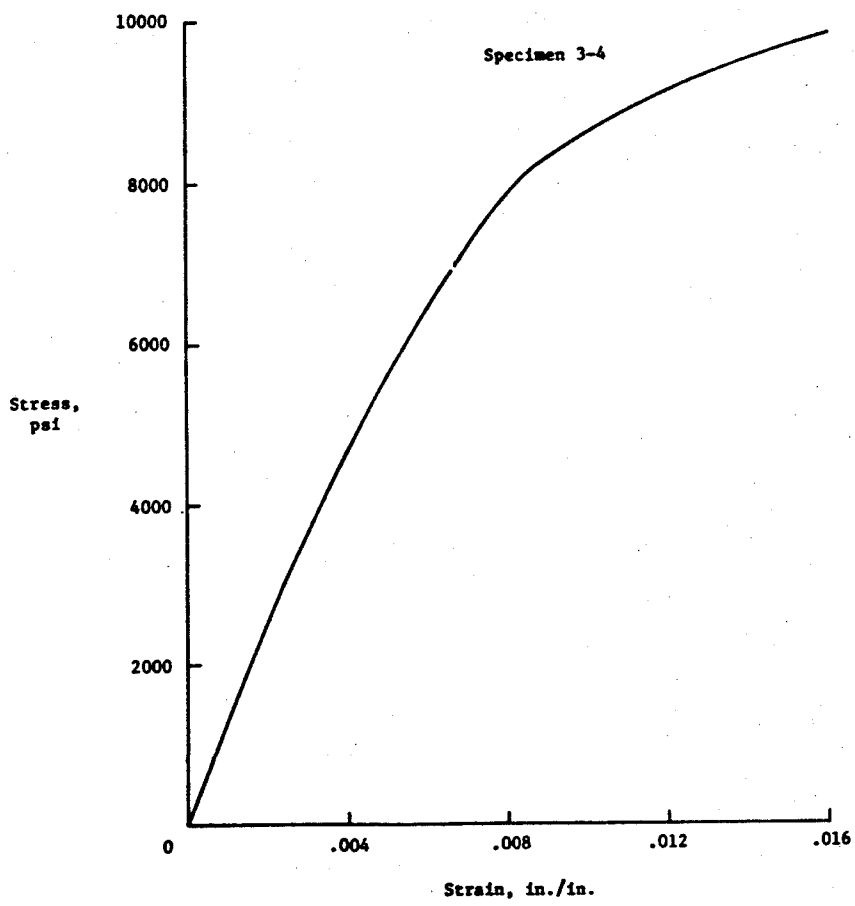


Figure 7.48 - Shear stress-strain curve for glass-epoxy.

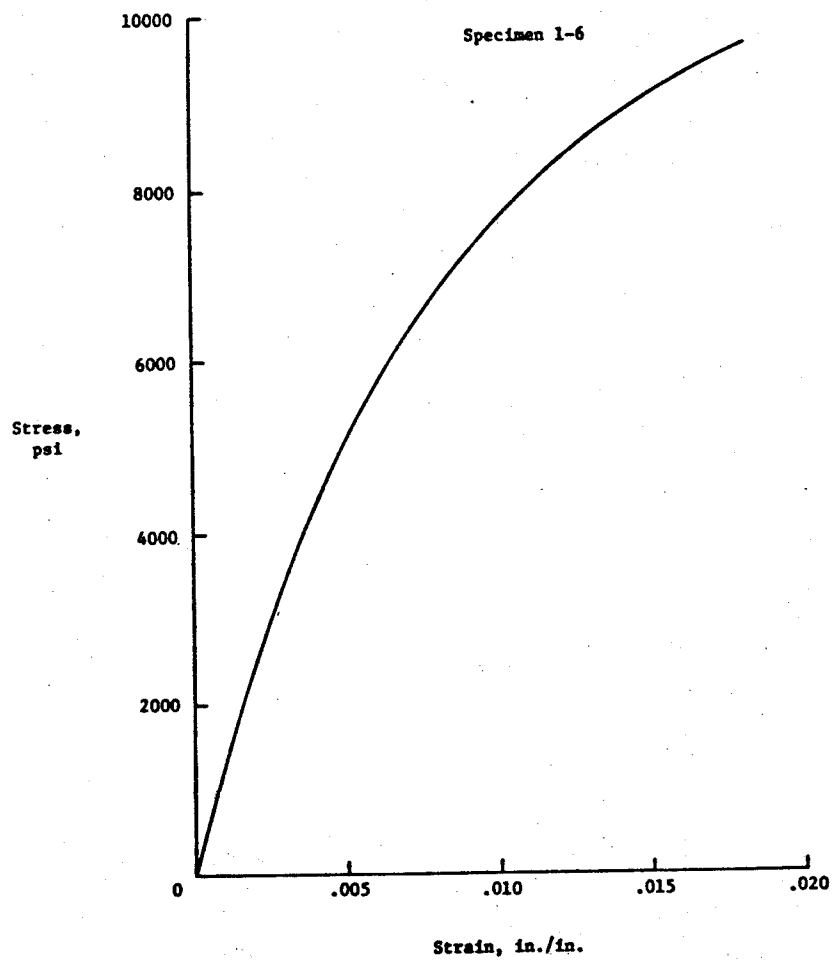


Figure 7.49 - Shear stress-strain curve for boron-epoxy (4.0 mil filaments).

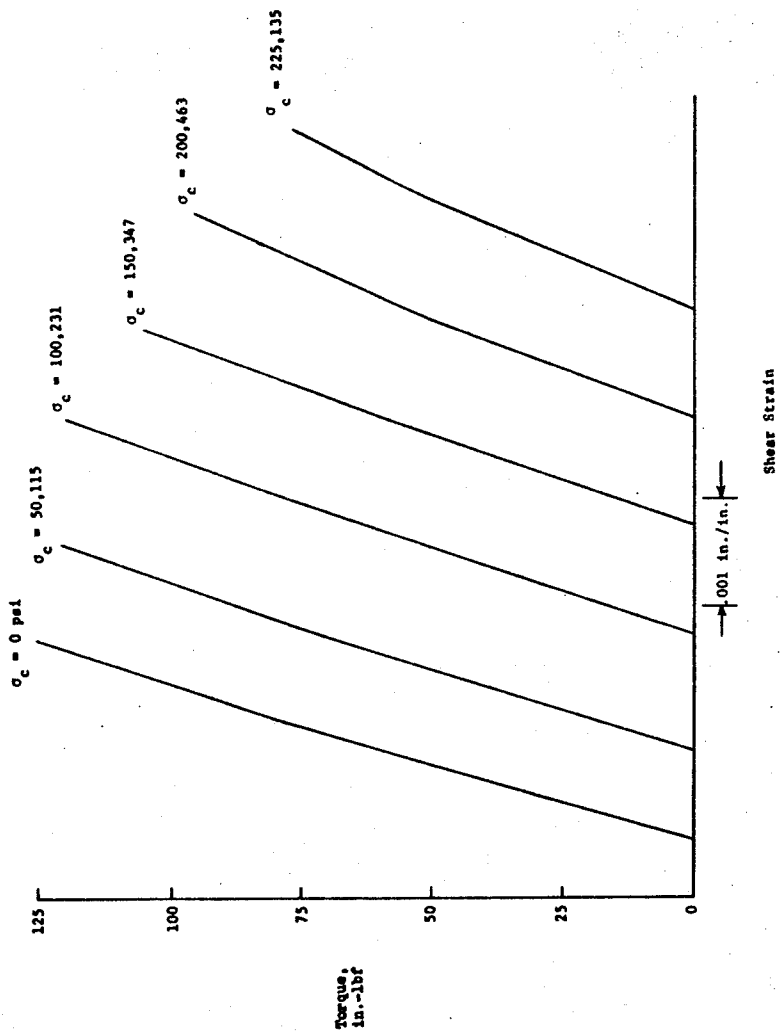


Figure 7.50 - Torque-strain plots for boron-epoxy specimen 1-5.

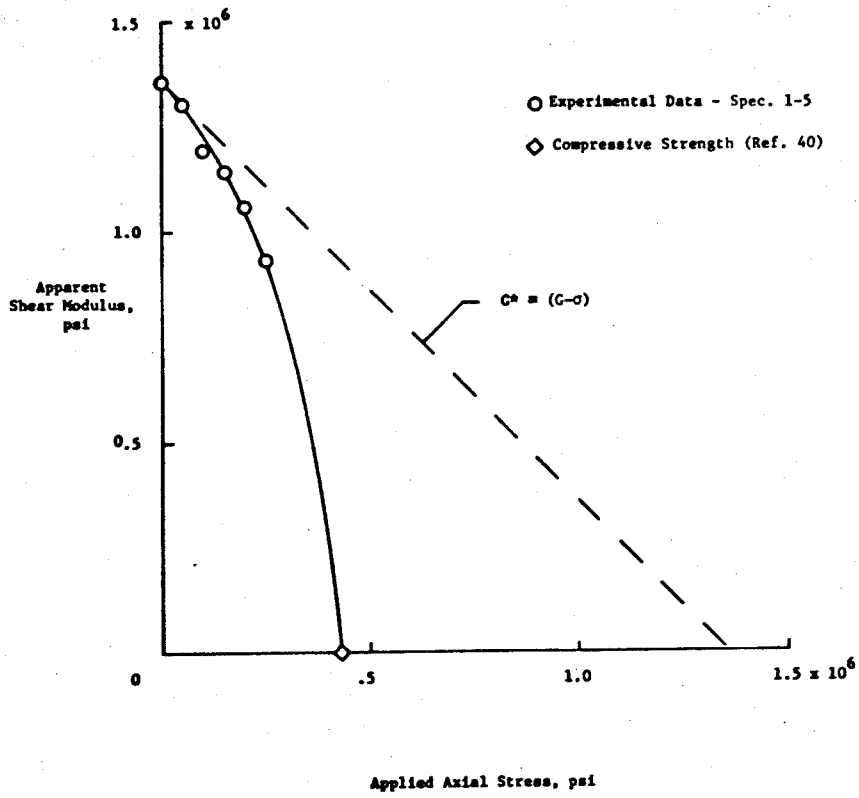


Figure 7.51 - Effect of axial compressive stress on the shear modulus of boron-epoxy.

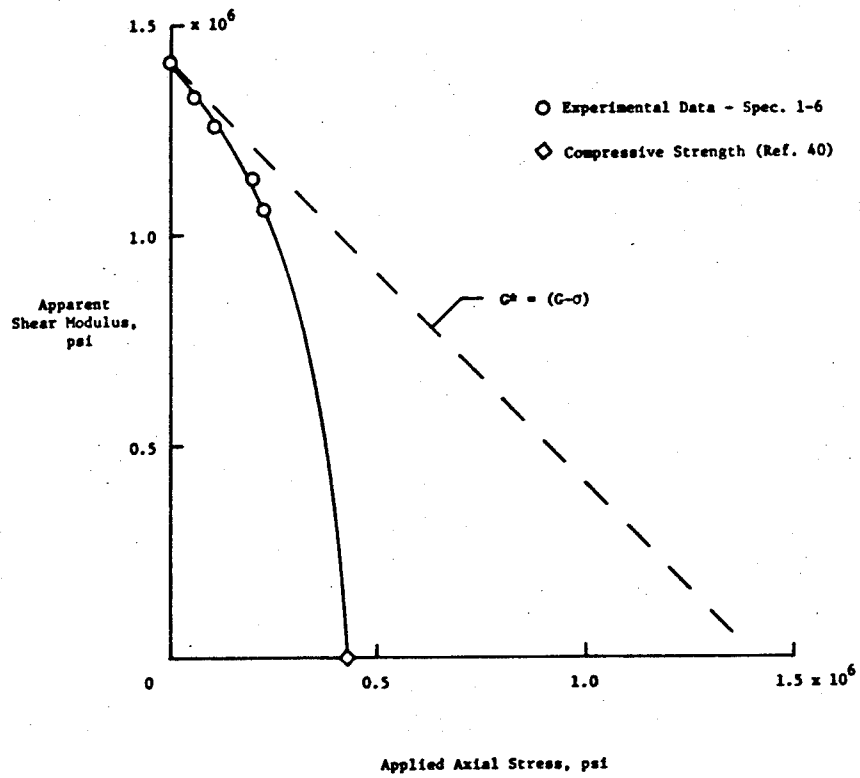


Figure 7.52 - Effect of axial compressive stress on the shear modulus of boron-epoxy.

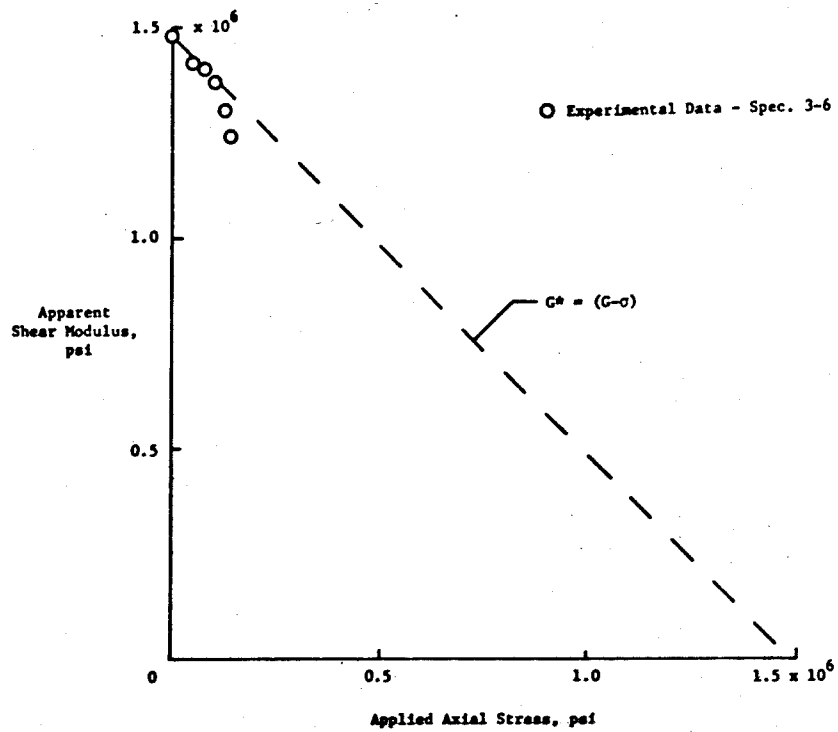


Figure 7.53 - Effect of axial compressive stress on the shear modulus of glass-epoxy.

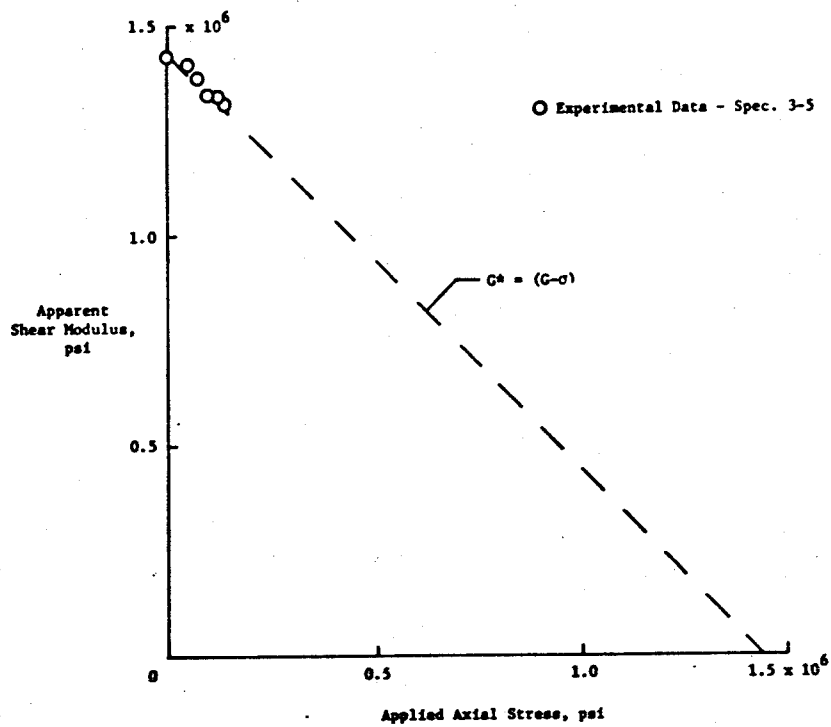


Figure 7.54 - Effect of axial compressive stress on the shear modulus of glass-epoxy.

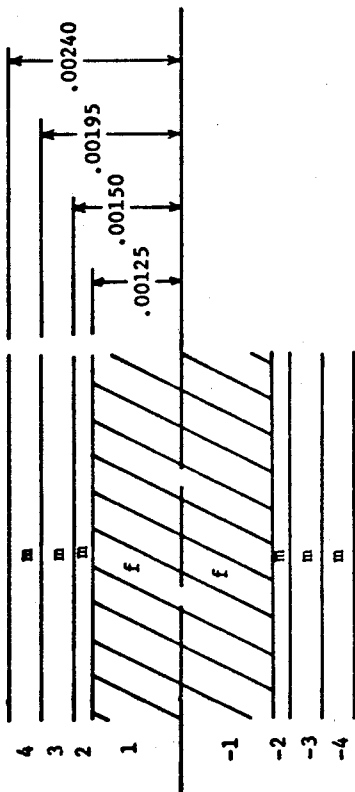


Figure 7.55 - Laminate cross-section used to represent boron-epoxy in the interlaminar shear stress analysis. Dimensions are given in inches.

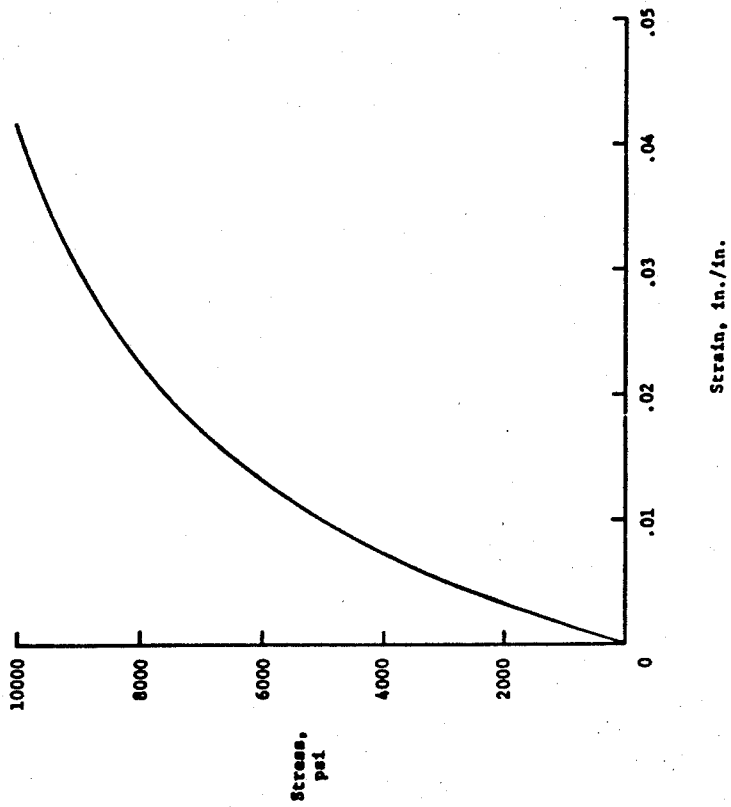


Figure 7.56 - Shear stress-strain curve used to represent behavior of epoxy in the interlaminar shear analysis.

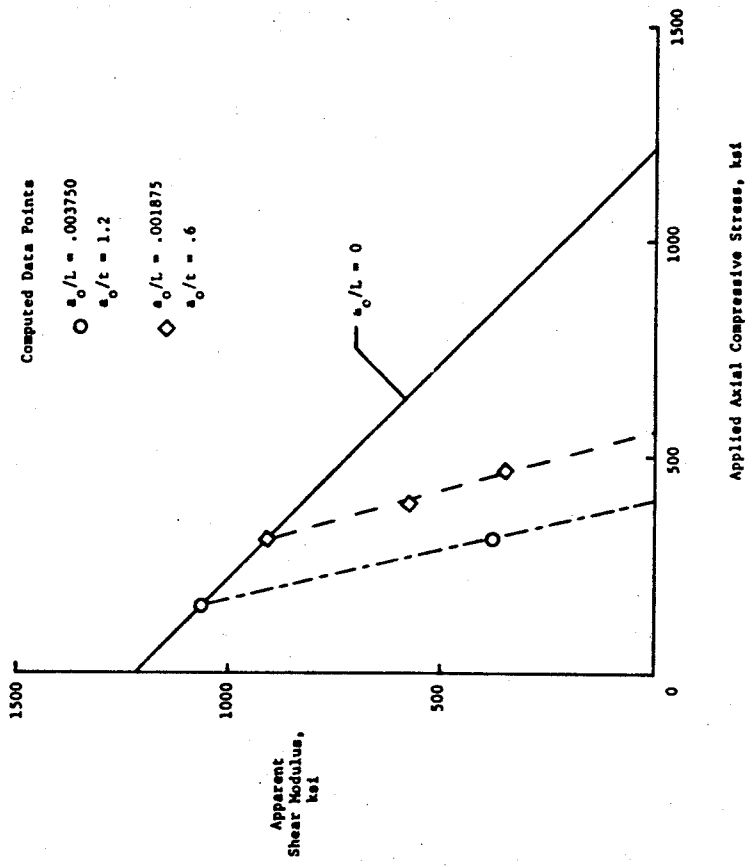


Figure 7.57 - Effect of axial compressive stress and fiber curvature on shear modulus for laminate model of boron-epoxy.

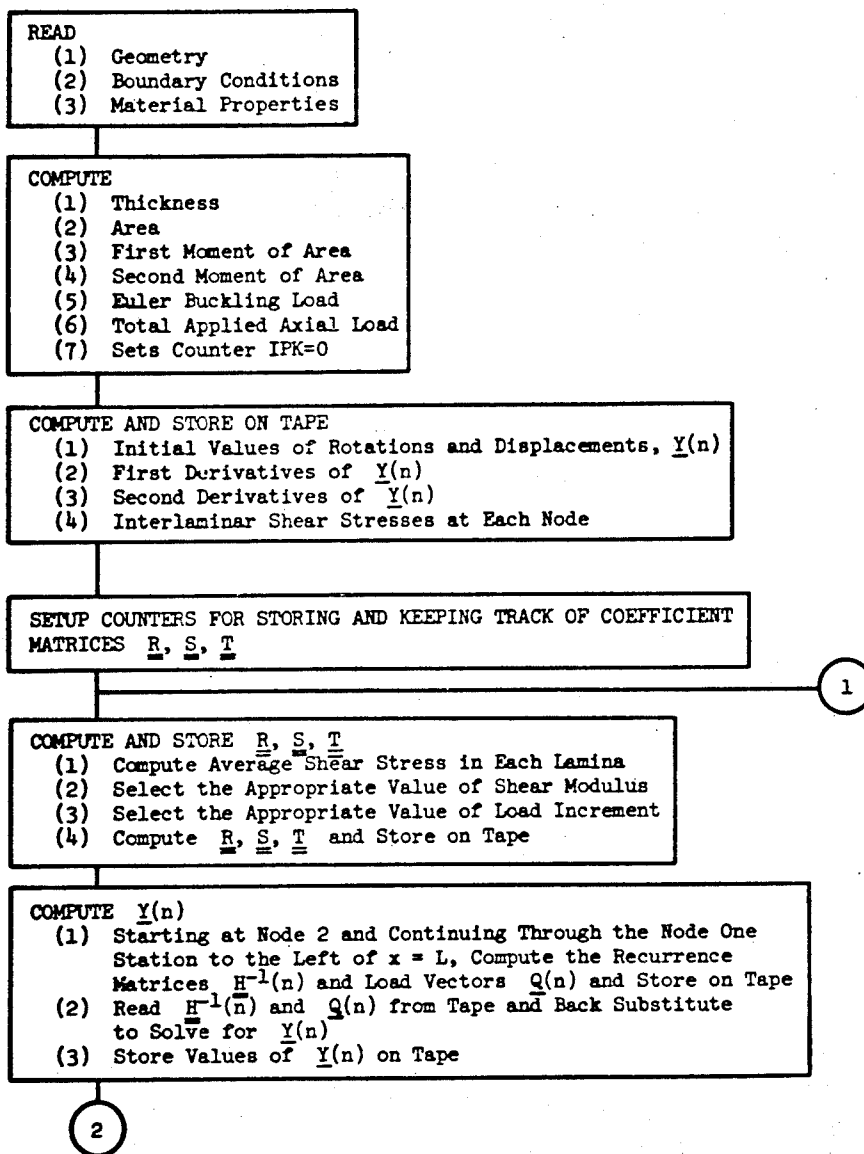


Figure A.1 - Flow diagram of interlaminar shear stress program.

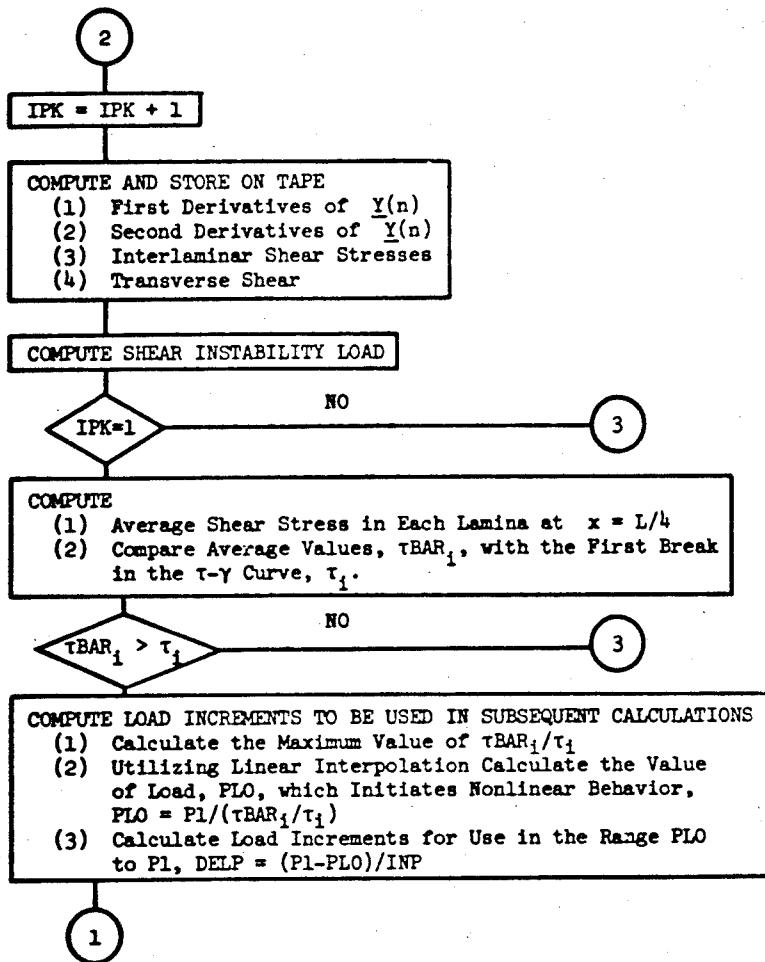


Figure A.1 - (Continued)

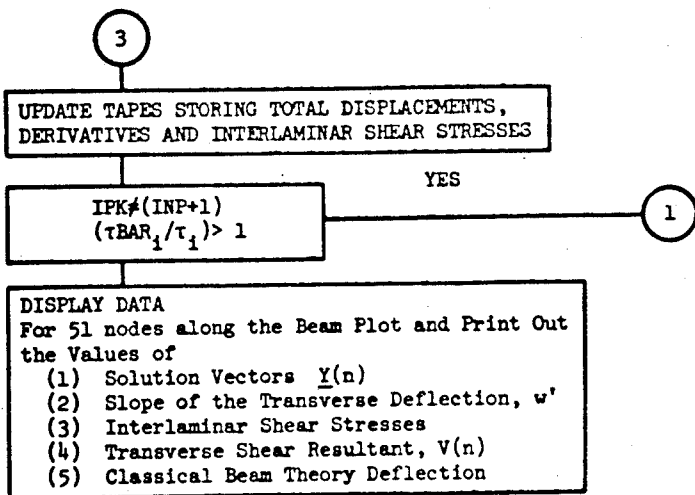


Figure A.1 - (Concluded)

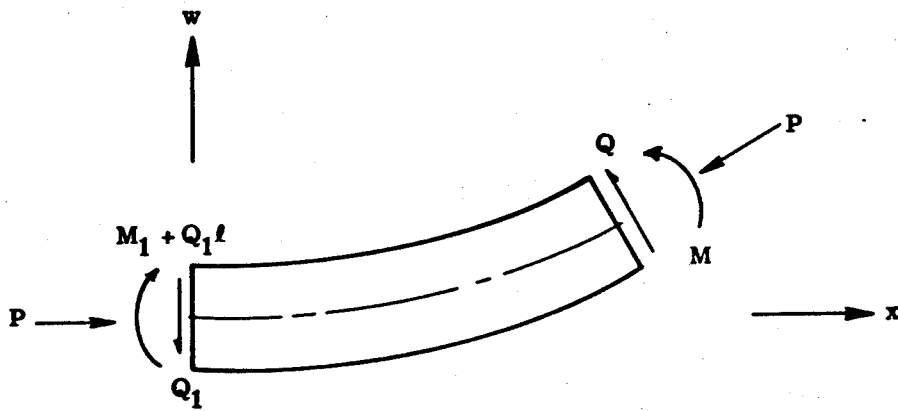


Figure B.1 - Free body diagram of beam, case A boundary conditions.

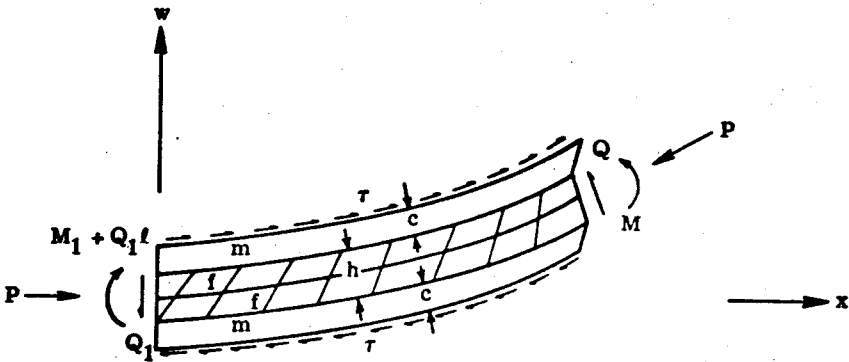


Figure B.2 - Free body diagram of beam, case B boundary conditions.

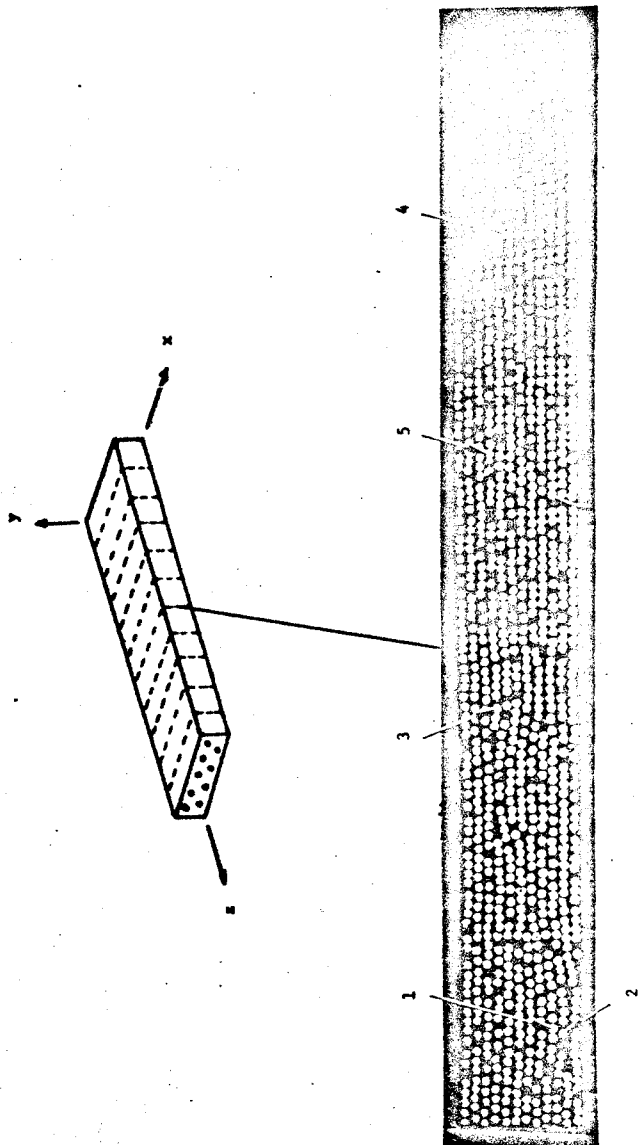


Figure C.1 - Method for determining fiber curvature.

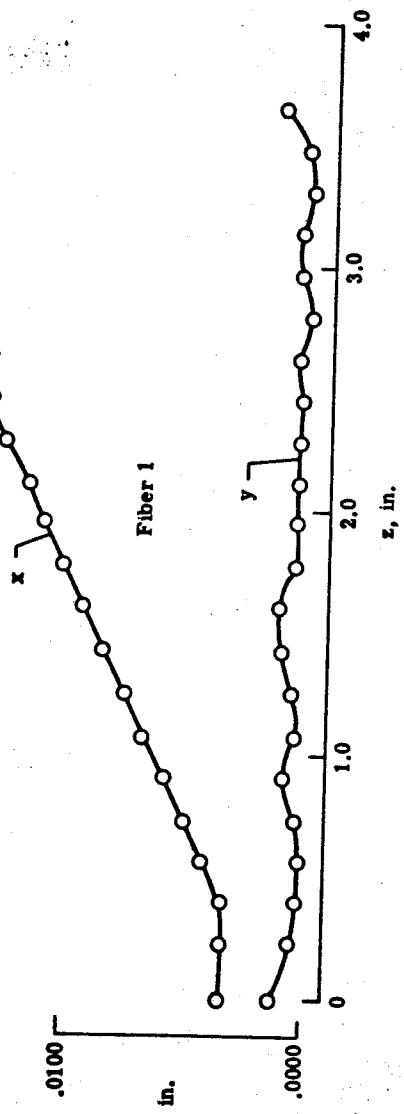


Figure C.2 - Fiber coordinates.

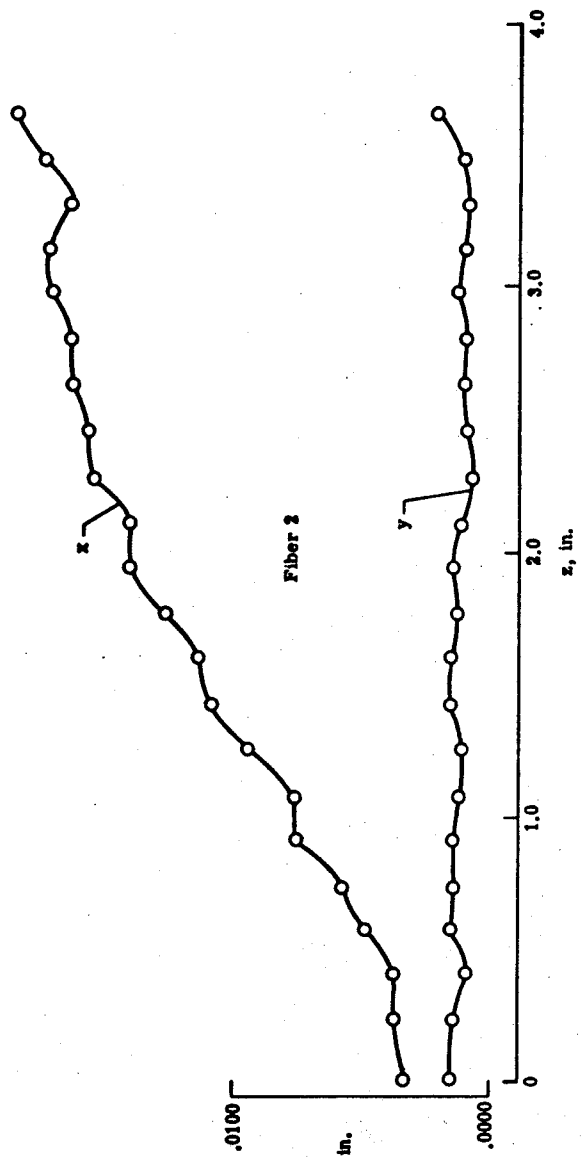


Figure C.2 - Continued.

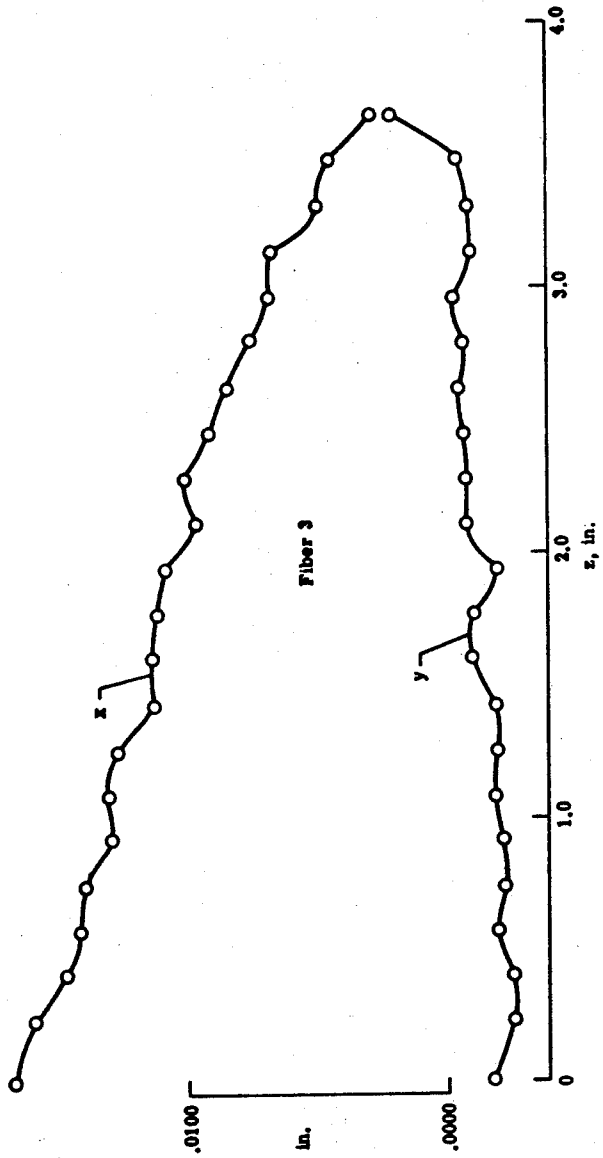


Figure C.2 - Continued.

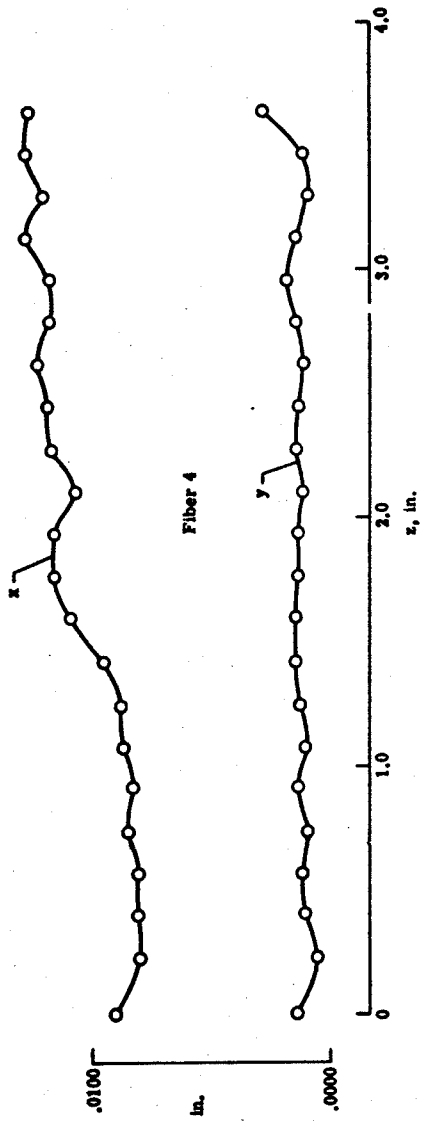


Figure C.2 - Continued.

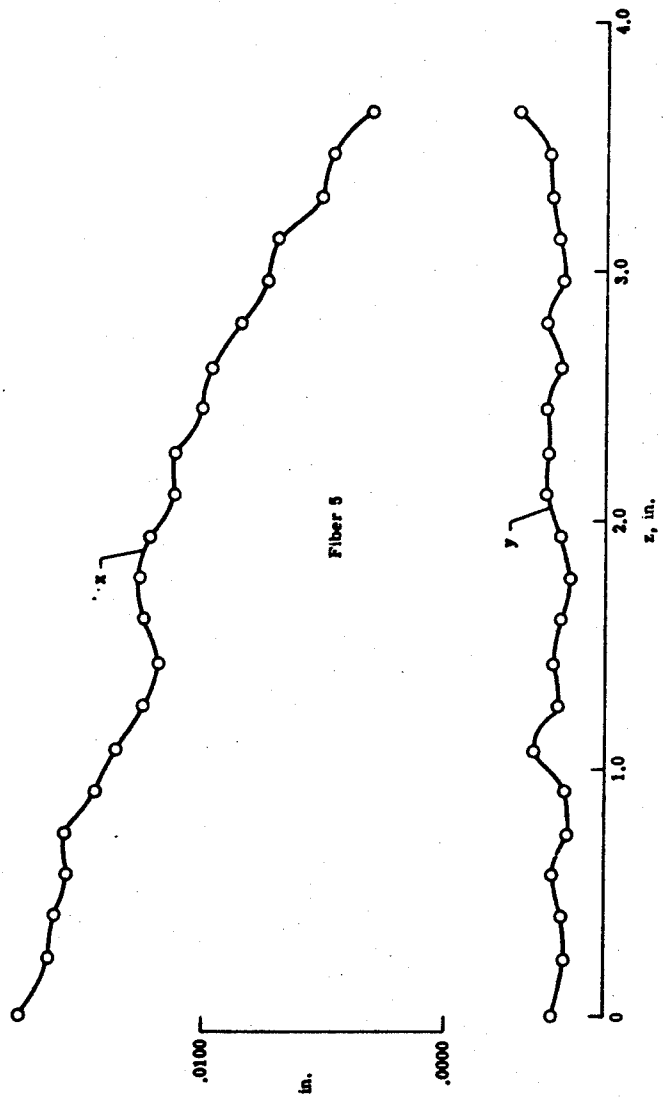


Figure C.2 - Concluded.

VITA

The author was born in Durham, North Carolina, on November 23, 1938. He attended public schools in Nash County and Rocky Mount, North Carolina and was graduated from Rocky Mount Senior High School in June of 1957. He entered North Carolina State University in September of 1958 and received the degree of Bachelor of Science in Mechanical Engineering in June 1962. From that time to the present, the author has been employed by the National Aeronautics and Space Administration at the Langley Research Center, Hampton, Virginia. In 1963, the author began taking graduate courses and received the degree of Master of Science from Virginia Polytechnic Institute in June of 1965. The author is married to the former Miss Lillian M. Ayers and they are the parents of two children, Debra Ann, age 12, and John G., III, age 9.

John G. Davis Jr.

COMPRESSIVE STRENGTH OF LAMINA REINFORCED
AND FIBER REINFORCED COMPOSITE MATERIALS

By

John G. Davis, Jr.

(ABSTRACT)

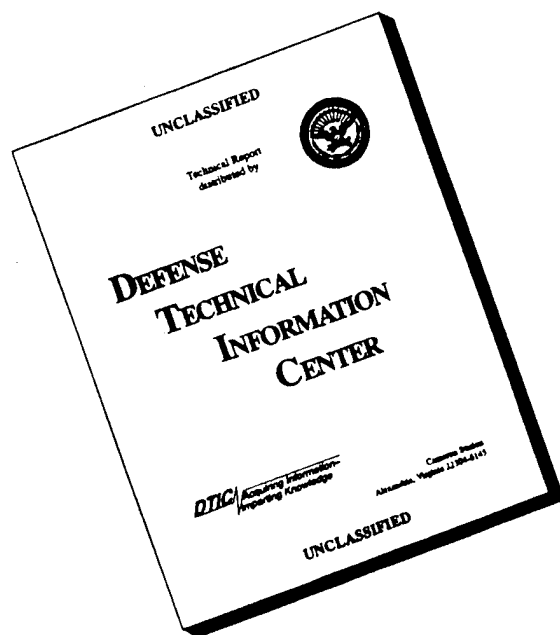
Results are presented from a theoretical and experimental investigation on the compressive strength of lamina reinforced and fiber reinforced composite materials when loaded parallel to the reinforcement. An analytical model which replaces the fiber reinforced composite with a laminate containing initially curved laminae has been proposed. By applying the Timoshenko beam equations to each layer of the laminate, an interlaminar shear stress analysis which can be used to predict the behavior of the laminate under compressive loading was developed. Two modes of failure are considered in the analysis, delamination and shear instability, and nonlinear shear stress-strain behavior of the laminae is included.

Axial compression tests were performed on aluminum-wax laminates, boron-epoxy tubes and S-glass-epoxy tubes. In addition, torsion tests and combined compression and torsion tests were conducted on the fiber reinforced tubes. Coordinates of fibers in a boron-epoxy laminate were measured. Experimental results indicate that the aluminum-wax laminates failed by delamination and that failure of the boron-epoxy composite in

compression is most likely due to shear instability. In addition it was shown that the shear modulus of boron-epoxy is a function of axial compressive stress and that the fibers in a boron-epoxy composite are not parallel but contain initial curvature.

Adequate correlation between theory and experiment was obtained for both lamina and fiber reinforced test results.

DISCLAIMER NOTICE



THIS DOCUMENT IS BEST QUALITY AVAILABLE. THE COPY FURNISHED TO DTIC CONTAINED A SIGNIFICANT NUMBER OF PAGES WHICH DO NOT REPRODUCE LEGIBLY.